

NUMERICAL STABILITY AND HEAT TRANSFER ANALYSES  
OF SUPERCRITICAL WATER FLOWING UPWARD  
IN VERTICAL HEATED PIPES

BY

ELAHEH EBRAHIMNIA

A Thesis Submitted to the Faculty of Graduate Studies of  
The University of Manitoba  
In Partial Fulfillment of the Requirements of the Degree of

MASTER OF SCIENCE

Department of Mechanical and Manufacturing Engineering  
University of Manitoba  
Winnipeg

Copyright © 2014 by Elaheh Ebrahimnia

## ABSTRACT

A numerical study is performed to model the 2-D axisymmetric turbulent flow of supercritical water flowing upward in vertical pipes with constant wall heat flux. This study was aimed to use CFD in analyzing supercritical flow instability and heat transfer characteristics in supercritical flow. The governing equations are solved using RANS models in the Computational Fluid Dynamics (CFD) code, ANSYS CFX v14.5.

First, three computational domains are simulated and results are compared with the existing experimental data of heat transfer and pressure drop. Based on the results of validations with experimental data, a constant value for turbulent Prandtl number ( $Pr_t$ ) is selected in studying the flow stability. Secondly, analyses of two types of flow instabilities (static and oscillatory) are performed in a vertical pipe with up-flow at 25MPa using a constant wall heat flux. Eight cases with different inlet temperatures and outlet K factors are studied and reported. Two turbulence models are used to find the instability thresholds: the standard  $k-\varepsilon$  model with a scalable wall-function and the  $k-\omega$  based SST model. The instability results of the CFD code are compared with 1-D non-linear code solutions. Also, conditions for approximating the thresholds of static and oscillatory instabilities based on steady-state results are assessed and discussed. In addition, the effects of changing  $Pr_t$ , inlet temperature, and outlet K factor on the instability threshold are discussed.

Converged steady-state results are obtained for a total of 350 cases by varying the mass flow rate and the  $Pr_t$  for the eight main cases. Transient analyses are also performed with the initial conditions of converged steady-state solution to determine the instability of the

flow. From the eight cases studied, it is determined that the results of instability thresholds obtained using the  $k-\varepsilon$  and the SST models are similar. Also the results of CFD and 1-D codes are different mainly as a consequence of the difference in the pressure drop predictions between the two codes. In addition, approximating the flow instability threshold by the conditions proposed for approximating the instability thresholds based on steady-state results generally holds true for a CFD solution for the cases studied in the present work. Results also indicate that  $Pr_t$  does not have a noticeable effect on the instability threshold for the cases examined in the present study. Furthermore, the present CFD work confirms the increase in the instability threshold mass flow rate by increasing the outlet K factor, both for static and oscillatory instabilities, for the up-flow geometry considered.

## **ACKNOWLEDGEMENTS**

I would like to express my appreciation and thanks to my advisors, Dr. V. Chatoorgoon and Dr. S.J. Ormiston, for their valuable guidance. I would also like to thank my committee members, Dr. B.-C. Wang and Dr. S. Filizadeh for their helpful comments and suggestions. I am also grateful to AECL for the financial support of this project. Last but not least, I would like to thank my husband, Javad and my family for their wonderful support, guidance, and patience.

## TABLE OF CONTENTS

ABSTRACT.....	I
ACKNOWLEDGEMENTS.....	III
TABLE OF CONTENTS.....	IV
LIST OF TABLES.....	VIII
LIST OF FIGURES.....	XII
NOMENCLATURE.....	XX
CHAPTER 1 INTRODUCTION.....	1
1.1 Supercritical Water Property Variation.....	3
1.2 Applications of Supercritical Flow.....	7
1.3 Supercritical Flow Instability.....	7
1.4 SCWR Channel Flow Modeling.....	9
CHAPTER 2 LITERATURE REVIEW.....	11
2.1 Scope of the Review.....	11
2.2 Flow Instability Experiments.....	11
2.3 One-Dimensional and Analytical Instability Analyses.....	12
2.4 CFD Instability Analyses.....	14
2.5 Turbulence and Heat Transfer Analyses of Supercritical Flow.....	16
2.6 Summary of the Literature Review.....	19
2.7 Objectives of the Present Work.....	19
CHAPTER 3 MODEL DESCRIPTION FOR STABILITY ANALYSIS.....	21
3.1 Geometry.....	21
3.2 Assumptions.....	22

3.3	Property Variation .....	22
3.4	Parameters defined .....	24
3.5	Governing Equations.....	25
3.5.1	Momentum Source terms .....	27
3.6	Turbulence Closure .....	29
3.6.1	The $k$ - $\varepsilon$ Turbulence Model .....	30
3.6.2	The Shear Stress Transport (SST) Turbulence Model .....	31
3.6.3	Wall Function.....	34
3.7	Boundary Conditions.....	36
3.7.1	Fluid Wall .....	36
3.7.2	Subdomain Fluid Wall .....	37
3.7.3	Inlet .....	37
3.7.4	Outlet.....	38
3.7.5	Symmetry .....	38
3.7.6	Domain Interface .....	38
CHAPTER 4 NUMERICAL SOLUTION METHOD FOR CFD ANALYSIS .....		39
4.1	Introduction .....	39
4.2	Grid Generation.....	39
4.3	Numerical Solution Method.....	40
CHAPTER 5 GRID INDEPENDENCE AND VALIDATION TESTS.....		44
5.1	Introduction .....	44
5.2	Heat Transfer Deterioration Phenomenon.....	45
5.3	Comparison with Experimental Heat Transfer Data .....	46

5.3.1	Identification of Experiments: Shitsman and Ornatsky .....	46
5.3.2	Grid-Independence Study: The Shitsman Test Case .....	46
5.3.3	Grid-Independence Study: The Ornatsky Test Case.....	56
5.3.4	Effect of Varying the Turbulent Prandtl Number .....	65
5.4	Pressure Drop of Supercritical flow .....	74
5.4.1	Pressure Terminology in CFX .....	74
5.4.2	Verification of Pressure Drop Using a Momentum Balance .....	76
5.5	Comparison with Experimental Results.....	80
5.5.1	Comparison of Frictional Pressure Drop from CFX with Experimental Results.....	80
5.6	Grid Independence Study: Ambrosini’s Geometry .....	81
CHAPTER 6 RESULTS AND DISCUSSION.....		94
6.1	Introduction .....	94
6.2	Determining the instability threshold.....	94
6.3	Static and Oscillatory Instability Cases.....	96
6.3.1	CFX Static Instability Results.....	97
6.3.2	Comparison of CFX Results with 1-D Non-Linear Results for Static Instability.....	103
6.3.3	Assessing Ledinegg’s and Chatoorgoon’s Conditions for Approximating the Static Instability Threshold.....	106
6.3.4	CFX Oscillatory Instability Results .....	114
6.3.5	Comparison of CFX Results with 1-D Non-Linear Results for Oscillatory Instability.....	120

6.3.6	Assessing Chatoorgoon’s Condition for Approximating the Oscillatory Instability Threshold.....	123
6.4	Summary of Static and Oscillatory Instabilities Results.....	129
6.5	Effect of Turbulent Prandtl Number .....	131
6.6	Effect of Outlet K Factor.....	139
6.7	Effect of Inlet Temperature .....	139
6.8	Variation of Properties in the Heat Transfer Deteriorated Region.....	139
CHAPTER 7 SUMMARY, CONCLUSIONS, AND RECOMMENDATIONS .....		144
7.1	Summary .....	144
7.2	Conclusions .....	145
7.3	Recommendations .....	148
REFERENCES .....		150
APPENDIX A GEOMETRY AND GRID .....		161
APPENDIX B MOMENTUM SOURCE TERM.....		167

## LIST OF TABLES

Table 5.1: Flow conditions for experiments of Shitsman and Ornatsky.....	46
Table 5.2: Grids used for mesh-independence check for case T1 .....	47
Table 5.3: RMS and maximum percentage deviation of axial variation of average angular wall temperature between grids for case T1 .....	47
Table 5.4: Grids used to study the effect of changing the number of radial and axial nodes simultaneously for case T1 .....	50
Table 5.5: RMS and maximum percentage deviation of axial variation of average angular wall temperature and static pressure drop between coarse, medium and fine grids for case T1 .....	51
Table 5.6: RMS and maximum percentage deviation of radial velocity between coarse, medium and fine grids for case T1 .....	52
Table 5.7: RMS and maximum percentage deviation of radial temperature between coarse, medium and fine grids for case T1 .....	54
Table 5.8: RMS and maximum percentage deviation of radial pressure between coarse, medium and fine grids for case T1 .....	56
Table 5.9: Grids used for mesh-independence check for case T2 .....	57
Table 5.10: RMS and maximum percentage deviation of axial variation of average angular wall temperature between grids for case T2 .....	57
Table 5.11: Grids used to study the effect of changing the number of radial and axial nodes simultaneously for case T2 .....	59
Table 5.12: RMS and maximum percentage deviation of axial variation of average angular wall temperature between coarse, medium and fine grids for case T2 .....	60

Table 5.13: RMS and maximum percentage deviation of radial velocity between coarse, medium and fine grids for case T2 .....	61
Table 5.14: RMS and maximum percentage deviation of radial temperature between coarse, medium and fine grids for case T2 .....	63
Table 5.15: RMS and maximum percentage deviation of radial pressure between coarse, medium and fine grids for case T2 .....	65
Table 5.16: RMS deviation of wall temperature from Shitsman’s experiment for different $Pr_t$ numbers for case T1 .....	71
Table 5.17: RMS deviation of wall temperature from Ornatsky’s experiment for different $Pr_t$ numbers for case T2 .....	73
Table 5.18: Flow conditions for the case used to verify pressure drop terms .....	78
Table 5.19: Flow conditions for the cases used to validate the CFX code .....	80
Table 5.20: Flow conditions for mesh-independence check using Ambrosini’s geometry .....	82
Table 5.21: Grids used for mesh-independence check for the Ambrosini test case .....	82
Table 5.22: RMS and maximum percentage deviation of axial variation of average angular wall temperature and static pressure drop between grids for the Ambrosini test case .....	83
Table 5.23: Grids used to study the effect of changing the number of radial and axial nodes simultaneously for the Ambrosini test case .....	86
Table 5.24: RMS and maximum percentage deviation of axial variation of average angular wall temperature and static pressure drop between coarse, medium and fine grids for the Ambrosini test case .....	87

Table 5.25: RMS and maximum percentage deviation of radial velocity between coarse, medium and fine grids for the Ambrosini test case .....	89
Table 5.26: RMS and maximum percentage deviation of radial temperature between coarse, medium and fine grids for the Ambrosini test case .....	91
Table 5.27: RMS and maximum percentage deviation of radial pressure between coarse, medium and fine grids for the Ambrosini test case .....	93
Table 5.28: The final grid used in the simulations for the Ambrosini test case .....	93
Table 6.1: Flow conditions for the cases used in the simulations, leading to static instability.....	96
Table 6.2: Flow conditions for the cases used in the simulations, leading to oscillatory instability.....	97
Table 6.3: Static instability threshold mass flow rates predicted by CFD.....	99
Table 6.4: Static instability threshold mass flow rates predicted by 1-D code and comparison with CFD.....	104
Table 6.5: CFD mass flow rate predictions corresponding to Chatoorgoon's and Ledinegg's criteria for static instability .....	111
Table 6.6: 1-D code mass flow rate predictions corresponding to Chatoorgoon's and Ledinegg's criteria for static instability .....	112
Table 6.7: Differences in CFD and 1-D mass flow rate predictions corresponding to Chatoorgoon's and Ledinegg's criteria for static instability and the instability thresholds .....	113
Table 6.8: Oscillatory instability threshold mass flow rates and period of oscillation predicted by CFD.....	117

Table 6.9: Oscillatory instability threshold predicted by 1-D code and comparison with the CFD results .....	122
Table 6.10: CFD and 1-D mass flow rates corresponding to Chatoorgoon's criteria for oscillatory instability and comparison with the instability threshold .....	128
Table 6.11: Comparison of CFD and 1-D results corresponding to Chatoorgoon's criterion for oscillatory instability with the instability thresholds .....	129
Table 6.12: Comparison of static instability threshold mass flow rates between two values of $Pr_t$ using the SST model.....	138
Table 6.13: Comparison of oscillatory instability threshold mass flow rates between two values of $Pr_t$ using the SST model.....	138

## LIST OF FIGURES

Figure 1.1: Schematic of a SCWR.....	2
Figure 1.2: Schematic of CANDU SCWR .....	3
Figure 1.3: Phase diagram of water .....	4
Figure 1.4: Variation of water density with temperature at constant pressures.....	5
Figure 1.5: Variation of $C_p$ for supercritical water with temperature at constant pressures .....	6
Figure 1.6: Variation of water thermo-physical properties at a supercritical pressure of 25 MPa.....	6
Figure 3.1: Geometry of the vertical pipe used for simulations .....	21
Figure 3.2: Cross section view of the geometry used for simulations .....	22
Figure 3.3: Regions and equations of IAPWS .....	24
Figure 4.1: A cross sectional view of the a) geometry blocking and b) mesh.....	40
Figure 4.2: Near-wall treatment for a typical coarse mesh cross section .....	40
Figure 5.1: Effect of near-wall spacing on average angular wall temperature along the pipe for case T1.....	48
Figure 5.2: Maximum difference in angular wall temperature at each axial location along the pipe for case T1.....	49
Figure 5.3: Comparison of average angular wall temperature between three grids shown in Table 5.5 for case T1 .....	51
Figure 5.4: Comparison of radial variation of velocity at $x/L = 1/2$ between three grids for case T1.....	53

Figure 5.5: Comparison of radial variation of outlet velocity between three grids for case T1 .....	53
Figure 5.6: Comparison of radial variation of temperature at $x/L = 1/2$ between three grids for case T1.....	55
Figure 5.7: Comparison of radial variation of outlet temperature between three grids for case T1 .....	55
Figure 5.8: Effect of near-wall spacing on average angular wall temperature along the pipe for case T2.....	58
Figure 5.9: Maximum difference in angular wall temperature at each axial location along the pipe for case T2.....	59
Figure 5.10: Comparison of average angular wall temperature between three grids shown in Table 5.12 for case T2 .....	61
Figure 5.11: Comparison of radial variation of velocity at $x/L = 1/2$ between three grids for case T2.....	62
Figure 5.12: Comparison of radial variation of outlet velocity between three grids for case T2 .....	62
Figure 5.13: Comparison of radial variation of temperature at $x/L = 1/2$ between three grids for case T2.....	64
Figure 5.14: Comparison of radial variation of outlet temperature between three grids for case T2 .....	64
Figure 5.15: Comparison of wall temperature with Shitsman's experiment and Jaromin and Anglart's numerical work- $Pr_t=0.9$ for case T1 .....	69

Figure 5.16: Comparison of wall temperature with Shitsman's experiment and Jaromin and Anglart's numerical work- $Pr_t = 1$ for case T1 .....	70
Figure 5.17: Comparison of wall temperature with Shitsman's experiment for different $Pr_t$ numbers for case T1 .....	70
Figure 5.18: Comparison of wall temperature with Ornatsky's experiment and Jaromin and Anglart's numerical work- $Pr_t = 0.9$ for case T2 .....	72
Figure 5.19: Comparison of wall temperature with Ornatsky's experiment and Jaromin and Anglart's numerical work- $Pr_t = 1$ for case T2 .....	72
Figure 5.20: Comparison of wall temperature with Ornatsky's experiment for different $Pr_t$ numbers for case T2 .....	73
Figure 5.21: Comparison of right and left hand sides of Equation (5.19) vs. the non-dimensional length of the pipe .....	78
Figure 5.22: Variation of different terms in Equation (5.19) vs. the non-dimensional length of the pipe .....	79
Figure 5.23: Comparison of frictional pressure drops between two methods .....	80
Figure 5.24: Comparison of frictional pressure drop using the SST and the $k-\epsilon$ models with experimental results .....	81
Figure 5.25: Effect of near-wall spacing on average angular wall temperature along the pipe for the Ambrosini test case.....	84
Figure 5.26: Effect of near-wall spacing on static pressure drop along the pipe for the Ambrosini test case .....	85
Figure 5.27: Maximum difference in angular wall temperature at each axial location along the pipe for the Ambrosini test case.....	86

Figure 5.28: Comparison of average angular wall temperature between three grids for the Ambrosini test case .....	88
Figure 5.29: Comparison of static pressure between three grids for the Ambrosini test case.....	88
Figure 5.30: Comparison of radial variation of velocity at $x/L = 1/2$ between three grids for the Ambrosini test case .....	90
Figure 5.31: Comparison of radial variation of outlet velocity between three grids for the Ambrosini test case.....	90
Figure 5.32: Comparison of radial variation of temperature at $x/L = 1/2$ between three grids for the Ambrosini test case .....	92
Figure 5.33: Comparison of radial variation of outlet temperature between three grids for the Ambrosini test case .....	92
Figure 6.1: CFD results for an unstable case using the SST model for Case S1 ( $\dot{m} = 0.0575$ kg/s).....	98
Figure 6.2: CFD results for a stable case using the SST model for Case S1 ( $\dot{m} = 0.058$ kg/s).....	98
Figure 6.3: Axial wall temperature of the $k-\varepsilon$ and the SST models for Case S4 ( $\dot{m} = 0.06$ kg/s).....	100
Figure 6.4: Axial static pressure drop of the $k-\varepsilon$ and the SST models for Case S4 ( $\dot{m} = 0.06$ kg/s).....	101
Figure 6.5: Variation of Term 1 and Term 4 in Equation (6.1) versus the non-dimensional length of the pipe using the $k-\varepsilon$ and the SST models for Case S4 ( $\dot{m} = 0.06$ kg/s).....	102

Figure 6.6: 1-D non-linear (SPORTS) results for a stable case for Case S1 ( $\dot{m} = 0.058$ kg/s).....	103
Figure 6.7: 1-D non-linear (SPORTS) results for an unstable case for Case S1 ( $\dot{m} = 0.056$ kg/s).....	104
Figure 6.8: Axial static pressure drop using 1-D code and the SST model for Case S1 ( $\dot{m} = 0.058$ kg/s).....	106
Figure 6.9: Instability boundary and $\Delta(p + \rho u^2)$ and $\Delta p$ of the channel versus mass flow rate using the $k-\varepsilon$ and the SST models and 1-D code for Case S1 .....	108
Figure 6.10: Instability boundary and $\Delta(p + \rho u^2)$ and $\Delta p$ of the channel versus mass flow rate using the $k-\varepsilon$ model for Case S1.....	109
Figure 6.11: Instability boundary and $\Delta(p + \rho u^2)$ and $\Delta p$ of the channel versus mass flow rate using the SST model for Case S1 .....	110
Figure 6.12: Instability boundary and $\Delta(p + \rho u^2)$ and $\Delta p$ of the channel versus mass flow rate using the 1-D code for Case S1 .....	110
Figure 6.13: CFD results for a stable case, using the $k-\varepsilon$ model for Case O3 ( $\dot{m} = 0.067$ kg/s).....	115
Figure 6.14: CFD results for an unstable case using the $k-\varepsilon$ model for Case O3 ( $\dot{m} = 0.0665$ kg/s).....	116
Figure 6.15: Variation of inlet and outlet mass flow rates with time for Case O3 ( $\dot{m} = 0.0665$ kg/s).....	116
Figure 6.16: Axial wall temperature of the $k-\varepsilon$ and the SST models for Case O4 ( $\dot{m} = 0.086$ kg/s).....	118

Figure 6.17: Axial pressure drop of the $k-\varepsilon$ and the SST models for Case O4 ( $\dot{m} = 0.086 \text{ kg/s}$ ).....	118
Figure 6.18: Variations of Term 1 and Term 4 in Equation (6.1) vs. the non-dimensional length of the pipe using the $k-\varepsilon$ and the SST models for Case O4 ( $\dot{m} = 0.086 \text{ kg/s}$ ) .....	119
Figure 6.19: 1-D non-linear (SPORTS) results for a stable case for Case O3 ( $\dot{m} = 0.058 \text{ kg/s}$ ).....	120
Figure 6.20: 1-D non-linear (SPORTS) results for an unstable case for Case O3 ( $\dot{m} = 0.057 \text{ kg/s}$ ).....	121
Figure 6.21: Axial static pressure for 1-D code and the SST model for Case O1 ( $\dot{m} = 0.052 \text{ kg/s}$ ).....	123
Figure 6.22: $\Delta(p + \rho u^2)$ of the channel versus mass flow rate using CFD and 1-D codes for Case O3 .....	124
Figure 6.23: Instability boundary, $\Delta(p + \rho u^2)$ of the channel, and $\partial \Delta(p + \rho u^2)/\partial \dot{m}$ , using CFD for Case O3.....	125
Figure 6.24: Instability boundary, $\Delta(p + \rho u^2)$ of the channel, and $\partial \Delta(p + \rho u^2)/\partial \dot{m}$ , using the $k-\varepsilon$ model for Case O3 .....	126
Figure 6.25: Instability boundary, $\Delta(p + \rho u^2)$ of the channel, and $\partial \Delta(p + \rho u^2)/\partial \dot{m}$ , using the SST model for Case O3.....	126
Figure 6.26: Instability boundary, $\Delta(p + \rho u^2)$ of the channel, and $\partial \Delta(p + \rho u^2)/\partial \dot{m}$ , using the 1-D code for Case O3 .....	127
Figure 6.27: Ratio of mass flow rate at the instability boundary to the mass flow rate at $\partial (\Delta p)/\partial \dot{m} = 0$ for static instability cases using CFD and 1-D codes .....	130

Figure 6.28: Ratio of mass flow rate at the instability boundary to the mass flow rate at $\partial \Delta(p + \rho u^2) / \partial \dot{m} = 0$ for static instability cases using CFD and 1-D codes.....	130
Figure 6.29: Ratio of mass flow rate at the instability boundary to the mass flow rate at $\partial^2 \Delta(p + \rho u^2) / \partial \dot{m}^2 = 0$ for oscillatory instability cases using CFD and 1-D codes ...	131
Figure 6.30: Comparison of wall temperature between two values of $Pr_t$ for Case S3 ( $\dot{m} = 0.061$ kg/s).....	132
Figure 6.31: Comparison of static pressure between two values of $Pr_t$ for Case S3 ( $\dot{m} = 0.061$ kg/s).....	133
Figure 6.32: Comparison of wall temperature between two values of $Pr_t$ for Case O4 ( $\dot{m} = 0.089$ kg/s).....	134
Figure 6.33: Comparison of static pressure between two values of $Pr_t$ for Case O4 ( $\dot{m} = 0.089$ kg/s).....	134
Figure 6.34: Comparison of wall temperature between two values of $Pr_t$ for Case O3 ( $\dot{m} = 0.067$ kg/s).....	135
Figure 6.35: Comparison of static pressure between two values of $Pr_t$ for Case O3 ( $\dot{m} = 0.067$ kg/s).....	136
Figure 6.36: Axial variation of different terms in Equation (6.1) using $Pr_t = 0.7$ and $0.95$ for Case O3 ( $\dot{m} = 0.067$ kg/s) .....	137
Figure 6.37: Axial variation of wall temperature for different mass flow rates leading to HTD using the SST model for Case S2 .....	140
Figure 6.38: Axial near-wall variation of thermal conductivity for the region before the K factor, using the SST model for Case S2 ( $\dot{m} = 0.052$ ) .....	142

Figure 6.39: Radial variation of velocity at different axial locations using the SST model for Case S2 ( $\dot{m} = 0.052 \text{ kg/s}$ ) .....	142
Figure 6.40: Axial near-wall variation of velocity gradient and turbulence kinetic energy for the region before the K factor, using the SST model for Case S2 ( $\dot{m} = 0.052 \text{ kg/s}$ ). 143	
Figure A.1: 3-D bounding box .....	162
Figure A.2: Perpendicular splits on $x$ - $y$ and $x$ - $z$ planes .....	162
Figure A.3: The block which was deleted .....	163
Figure A.4: Geometry and blocking after the lower left block was deleted .....	163
Figure A.5: Quarter O-Grid block .....	164
Figure A.6: Blocks that were deleted.....	164
Figure A.7: Geometry and blocking after the blocks were deleted .....	165
Figure A.8: Associated vertices of the blocking and points of the geometry .....	165
Figure A.9: The mesh applied on the geometry.....	166
Figure B.1: Radial variation of momentum source in the subdomain using the Loss Model for Case S4 ( $\dot{m} = 0.06 \text{ kg/s}$ ) .....	170
Figure B.2: Radial variation of velocity at different axial locations, slightly before and along the subdomain using the Loss Model for Case S4 ( $\dot{m} = 0.06 \text{ kg/s}$ ) .....	171
Figure B.3: Radial variation of momentum source in the subdomain using the Momentum Source Model for Case S4 ( $\dot{m} = 0.06 \text{ kg/s}$ ).....	172
Figure B.4: Radial variation of velocity at different axial locations, slightly before and along the subdomain using the Momentum Source Model for Case S4 ( $\dot{m} = 0.06 \text{ kg/s}$ ) 173	

## NOMENCLATURE

$A$	cross-section area [m <sup>2</sup> ]
$A'$	surface area [m <sup>2</sup> ]
$C$	a log-layer constant depending on wall roughness ( $C = 5.2$ for a smooth wall)
$C_p$	specific heat at constant pressure [J/(kg.K)]
$C_\mu, C_{\varepsilon 1}, C_{\varepsilon 2}$	turbulence model constants
$D$	diameter [m]
$F1, F2$	turbulence model blending functions
$g$	acceleration of gravity [m/s <sup>2</sup> ]
$h$	enthalpy [J/kg]
$h_{tot}$	total enthalpy [J/kg]
$I$	turbulence intensity
$k$	turbulence kinetic energy per unit mass [m <sup>2</sup> /s <sup>2</sup> ]
$\kappa$	von-Karman constant
$K_{loss}$	loss coefficient [1/m]
$K_{perm}$	permeability [m <sup>2</sup> ]
$L$	length [m]
$\dot{m}$	mass flow rate [kg/s]
$p$	static pressure [Pa]
$p'$	modified pressure [Pa]
$Pr$	laminar Prandtl number
$Pr_t$	turbulent Prandtl number
$P_k$	turbulence production term [kg/m.s <sup>3</sup> ]
$P_{kb}, P_{ke}$	representative of the influence of buoyancy [kg/m.s <sup>3</sup> ]

$q''$	heat flux [W/m <sup>2</sup> ]
$R$	radius [m]
$S_m$	momentum source term [kg/m <sup>2</sup> .s <sup>2</sup> ]
$T$	temperature [°C, K]
$t$	time [s]
$U$	velocity magnitude [m/s]
$u$	fluctuating velocity component in turbulent flow [m/s]
$y^+$	dimensionless distance of the first node from the wall
$u^+$	near-wall velocity
$u^*$	dimensionless velocity scale
$u_\tau$	friction velocity [m/s]
$U_t$	velocity tangent to the wall at the distance of $\Delta y$ from the wall [m/s]

Greek Symbols:

$\alpha, \beta, \sigma_\omega, \sigma_k$	model constants for $k$ and $\omega$ equations
$\varepsilon$	turbulence dissipation rate [m <sup>2</sup> /s <sup>3</sup> ]
$\rho$	density [kg/m <sup>3</sup> ]
$\sigma_p$	turbulent Schmidt number
$\sigma_\varepsilon, \sigma_k$	model constants for $\varepsilon$ and $k$ equations
$\lambda$	thermal conductivity [W/(m.K)]
$\mu$	dynamic viscosity [kg/(m.s)]
$\mu_t$	eddy viscosity [kg/(m.s)]
$\tau_\omega$	wall shear stress [N/m <sup>2</sup> ]
$\nu$	kinematic viscosity [m <sup>2</sup> /s]
$\omega$	frequency [1/s]

# **CHAPTER 1**

## **INTRODUCTION**

The Supercritical Water Reactor (SCWR) has been proposed by the U.S. DOE Nuclear Energy Research Advisory Committee and the Generation IV International Forum (2002) as one of the six designs for new Generation IV reactors. SCWRs are one of the three types of Light Water Reactors (LWRs). The other types are Boiling Water Reactors (BWRs) and Pressurized Water Reactors (PWRs). Using supercritical water in reactors as a primary coolant is believed to provide an improvement in overall plant efficiency compared to other types of LWRs (~45% versus ~33% of other LWRs). Considerable design simplification is another feature of a SCWR, which distinguishes it from a BWR and a PWR. A schematic of a SCWR is shown in Figure 1.1. The primary coolant (water) is pumped into the reactor core at a high pressure, where it is heated by the energy generated from the fission of atoms and is turned into supercritical water. Then, unlike the PWRs, where the heated water transfers its thermal energy to a secondary system, the supercritical water is passed through the turbine directly, like a BWR. The direct-cycle design of a SCWR makes it simpler than a PWR. Also, operating above the critical point eliminates the need for pressurizers and steam generators (needed in PWRs) and recirculation pumps, steam separators and dryers (needed in BWRs).

The goals of Generation IV reactor designs are defined in four broad areas of safety, sustainability, economics, and proliferation resistance and physical protection. Currently, the research on Generation IV reactors is ongoing and they are expected to become available for commercial use between 2015 and 2030 or beyond.

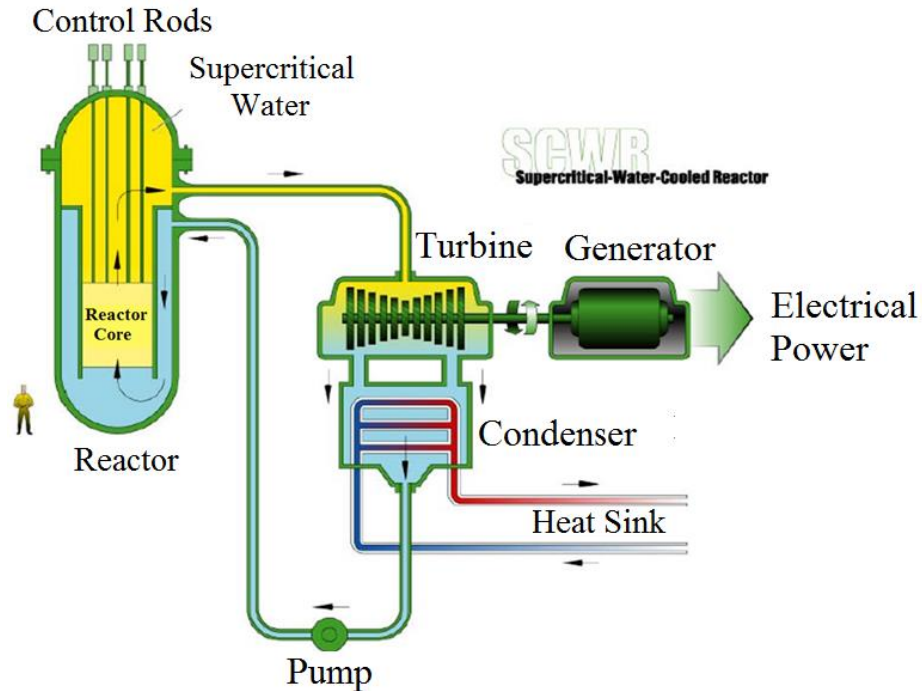


Figure 1.1: Schematic of a SCWR (The U.S. DOE Nuclear Energy Research Advisory Committee and the Generation IV International Forum, 2002)-used with permission

The Canadian contribution to various areas of generation IV international forum (GIF) SCWR projects consists of projects directly relevant to the Canada Deuterium Uranium (CANDU) SCWR fuel and core designs at Atomic Energy of Canada Limited (AECL) and fundamental research and development (R&D) projects related to SCW flow and heat transfer at various Canadian universities. A schematic of CANDU SCWR is shown in Figure 1.2. Pressure tubes are used in this design instead of a pressure vessel used in the design shown in Figure 1.1. A pressure-tube design, where the core is divided up into smaller tubes for each fuel channel, has potentially fewer issues with mechanical and thermal stresses.

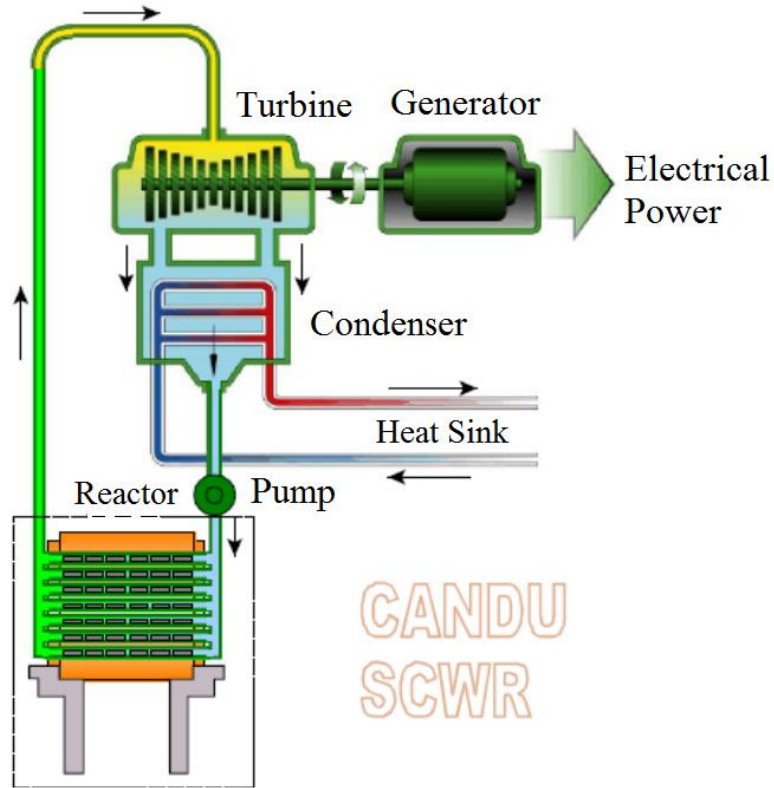


Figure 1.2: Schematic of CANDU SCWR (Brady et al., 2007) - used with permission

### 1.1 Supercritical Water Property Variation

Figure 1.2 shows the phase diagram of water ( $H_2O$ ) at different temperatures and pressures. The boiling line separates the gas and liquid regions and ends at the critical point, where the distinction between liquid and gas phases disappears. Above this point, water is single-phase and is called supercritical fluid. The critical temperature and pressure of  $H_2O$  are  $374.3\text{ }^\circ\text{C}$  and  $22.08\text{ MPa}$ , respectively.

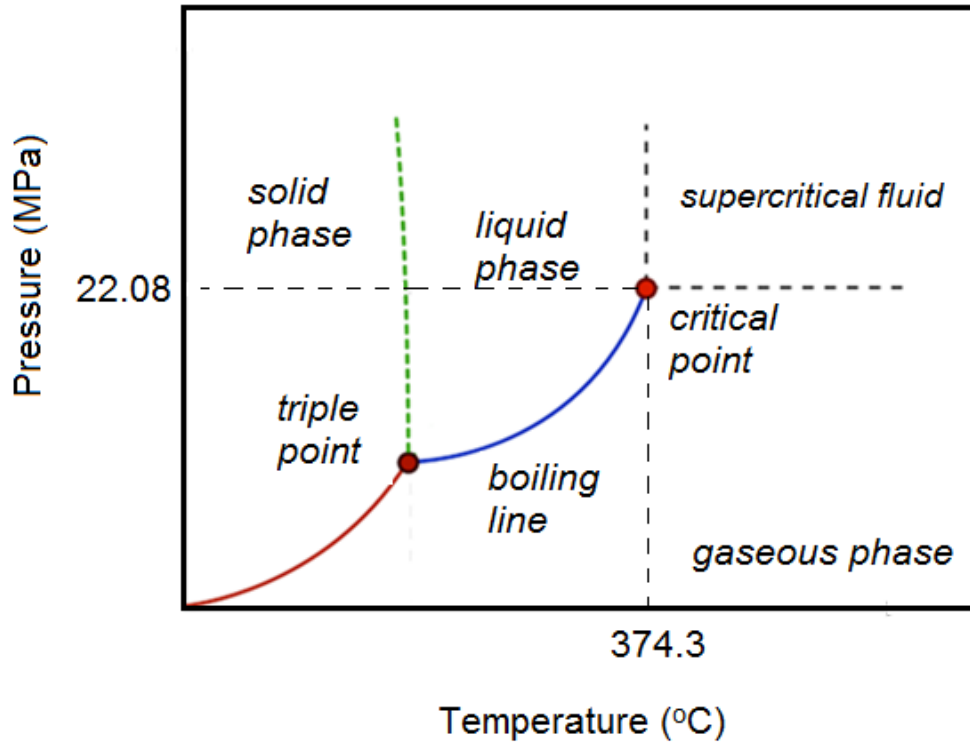


Figure 1.3: Phase diagram of water

In Figure 1.4, the variation of density with temperature at different pressures below and above the critical point is shown. At well below the critical pressure, the fluid goes through a two-phase region. As the temperature increases at a constant pressure, the liquid evaporates and results in the vertical line. In this region, both liquid and vapor phases are in equilibrium. However, as the pressure increases, the saturated vapor becomes denser, and the density of the saturated liquid decreases and results in a reduction in the length of the vertical line. As the pressure reaches its critical value, the vertical line disappears and the two phases become one single phase. At pressures slightly above the critical pressure, density has a strong variation with temperature and as the pressure increases, the variation of density becomes milder.

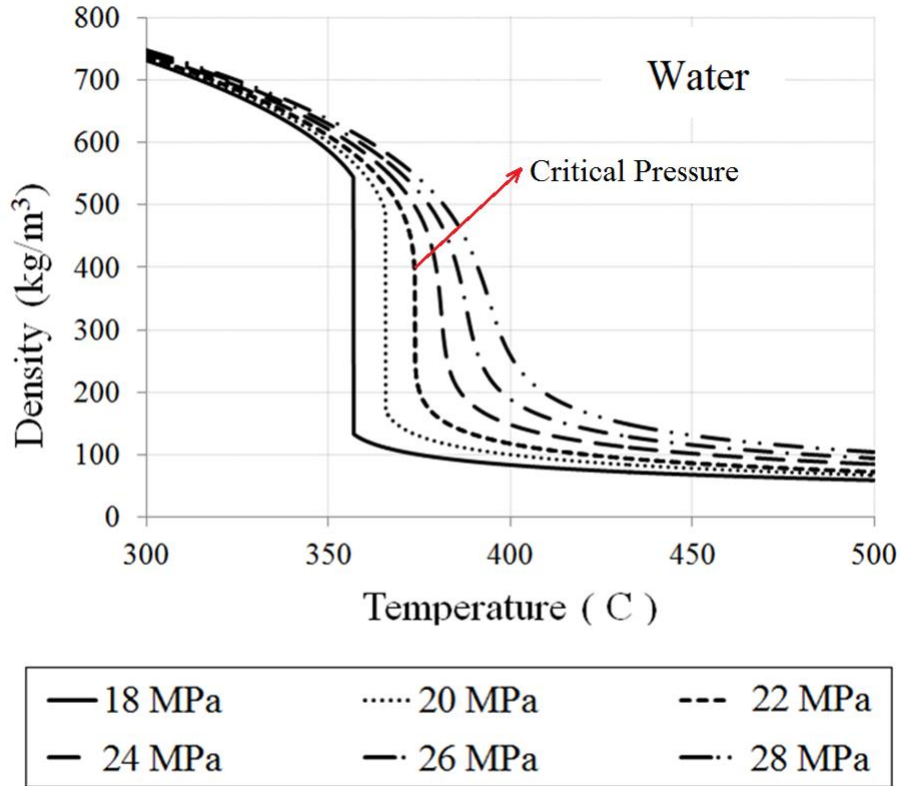


Figure 1.4: Variation of water density with temperature at constant pressures (Lemmon et al., 2013)

Figure 1.5 shows the variation of heat capacity ( $C_p$ ) with temperature at different pressures above the critical pressure. Slightly above the critical pressure,  $C_p$  has a strong variation with temperature. The temperature at which the heat capacity reaches its peak value is referred to as the pseudo-critical temperature. As shown in Figure 1.6, thermal conductivity and viscosity also vary significantly near the critical pressure and temperature. Following the strong variation of thermo-physical properties, both the turbulent and molecular diffusion of heat and momentum can be affected. Also, the strong variation of density can affect the turbulence production, either by flow acceleration or because of the buoyancy effect. Large variation of  $C_p$ , combined with large variations of thermal conductivity and turbulence production, may have important consequences in the heat transfer efficiency (He et al., 2008).

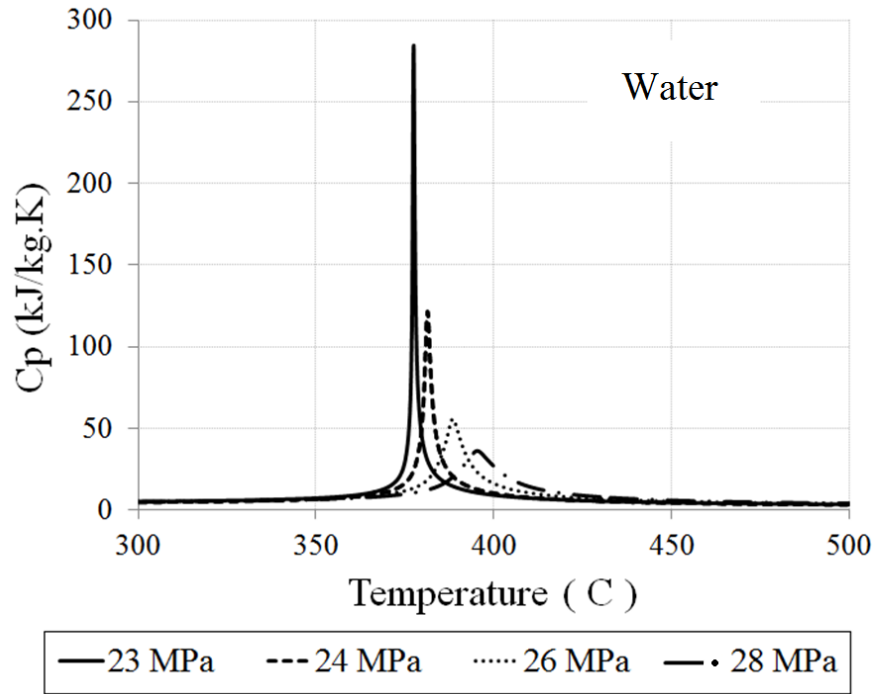


Figure 1.5: Variation of  $C_p$  for supercritical water with temperature at constant pressures (Lemmon et al., 2013)

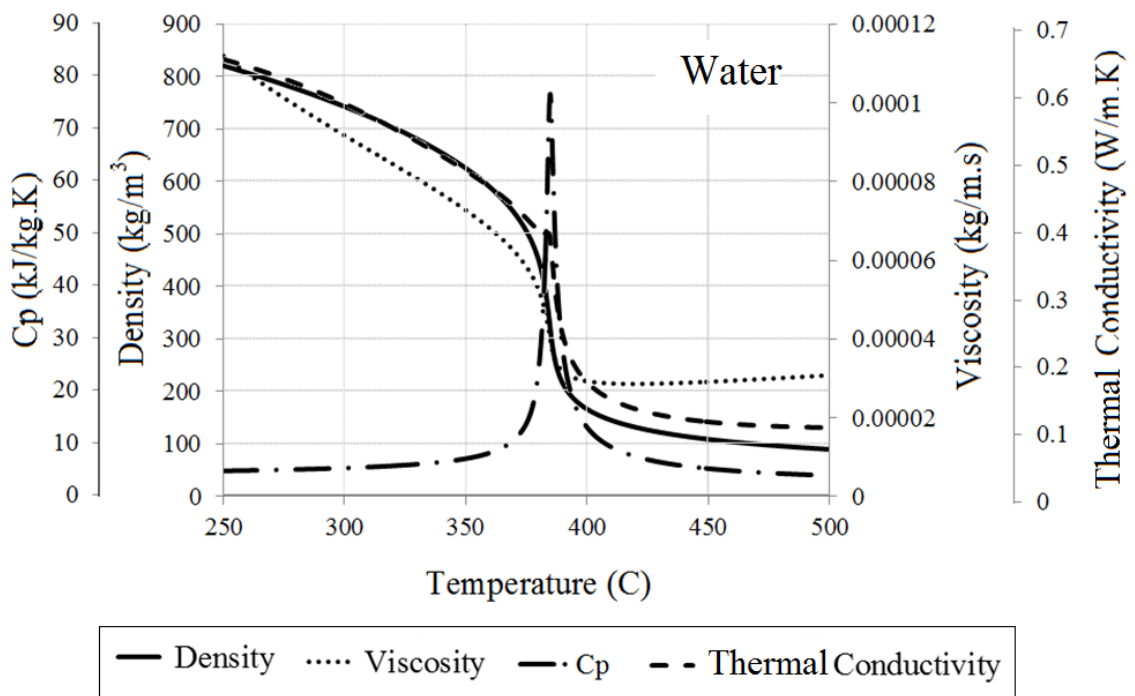


Figure 1.6: Variation of water thermo-physical properties at a supercritical pressure of 25 MPa (Lemmon et al., 2013)

## **1.2 Applications of Supercritical Flow**

Using supercritical fluids in different industrial applications is not new. Rocket engines were the first thermal engines that worked under supercritical conditions. However, the need for a higher efficiency and a lower emission level of CO<sub>2</sub> led to an increase in pressure and temperature in other engines, such as gas turbines, diesel piston engines, and aeronautical turbines. Extensive studies on supercritical pressure heat transfer were conducted in the 1960's and 1970's with the aim of developing supercritical water power stations. Recently there has been renewed interest in this subject and new studies are being conducted on the development of the supercritical water-cooled nuclear reactors and several other new applications involving fluids with supercritical pressures. The main advantages of using supercritical flow in nuclear reactors are increase in efficiency of nuclear power plants and decrease in the capital and operational costs. Decrease in reactor coolant pumping power and frictional losses are the other benefits that using a supercritical fluid provides (Duffey and Pioro, 2005)

Besides the advantages of using SCW in power plants, there is also an interest in using supercritical hydrogen in the active cooling of a re-usable earth-to-orbit hypersonic aircraft (Hendricks et al., 1970). Other applications of supercritical fluids are: as a coolant in super-conductors and electronic devices (Hendricks et al., 1970), as a refrigerant in air conditioning equipment (Lorentzen, 1994), and as a fuel for chemical and nuclear rockets (Hendricks et al., 1970).

## **1.3 Supercritical Flow Instability**

Despite the benefits of supercritical water in terms of overall efficiency, thermal hydraulic instabilities are likely to arise in supercritical water reactors due to the sharp

variations of some physical properties (mainly the density) along a heated pipe. A flow is stable if, when disturbed, its new operating conditions tend asymptotically towards the original initial condition; otherwise, the flow is said to be unstable. Two different kinds of instabilities have been encountered: static (also called excursive), and dynamic (also called oscillatory and density-wave oscillation). A flow is said to be subject to a static instability if, when disturbed, it moves away from its equilibrium position in an excursive manner without returning to the original state. On the other hand, a flow is said to be dynamically unstable when there is adequate interaction and delayed feedback between the inertia of the flow and the compressibility of the fluid (Kakac, 2007).

During an oscillatory instability, the mass flow rate starts oscillating and oscillation amplitudes grow over time. Periodic oscillations of mass flow rate may induce mechanical vibrations and cause failure of a heated channel. Under certain circumstances, large flow oscillations can lead to superheating and burnout of the heated channel because less heat is removed from the channel and the wall temperature increases significantly. In a nuclear reactor, periodic oscillations of mass flow rate result in periodic oscillations of wall temperature and cause thermal fatigue in the wall and cladding materials. Following the thermal fatigue in the wall, mechanical breakdown or even more serious accidents such as release of radioactive materials may occur.

Static instability is also dangerous as the flow rate might go to zero and lead to burnout of the channel. Both types of instabilities are undesirable and flow conditions should be designed with a sufficient margin against them to ensure the safety of SCWRs.

#### **1.4 SCWR Channel Flow Modeling**

A reactor core consists of fuel bundles with two headers at the inlet and at the outlet, to impose a constant pressure drop to the system. The coolant surrounding the fuel bundles removes the heat from the core and carries it to electrical generators to produce electrical power. To simulate the heat transfer to the coolant, a simplified model with a pipe of the same hydraulic diameter is used.

To study the instability of the flow in a pipe, certain parameters must be defined which typically include: operational pressure, mass flow rate, and the inlet temperature of the coolant, the heat flux applied to the coolant, and inlet and outlet pressure drop coefficients. These parameters are then used as boundary conditions to predict the field of velocity, pressure, and temperature, which lead to prediction of the instability boundary.

Flow instability can be assessed using experiments, Computational Fluid Dynamics (CFD), and analytical methods. Experimental works on supercritical flow instability are limited. Analytical modeling, on the other hand, has been widely used in modeling the flow instability. Performing analytical study is relatively inexpensive, but might give an inaccurate prediction of the flow behaviour due to assumptions and simplifications in the modeling process.

CFD is based on fundamental conservation equations and depends on turbulence models selected to solve the flow field. It can be performed for 2-D, 2-D axisymmetric, and 3-D flow. CFD has been widely used to study the heat transfer characteristics of SCW and to improve the understanding of heat transfer mechanism in the supercritical region. CFD modeling of supercritical flow is believed to provide a more realistic prediction of flow

behaviour than 1-D codes in exchange for greater computational costs. Therefore, in analyzing the stability of the flow, CFD is mainly used to assess the performance of 1-D codes, since 1-D codes are simpler and quicker, and are more often used in industry. A formal definition of the problem and statement of motivations will be given in Chapter 2.

## **CHAPTER 2**

### **LITERATURE REVIEW**

#### **2.1 Scope of the Review**

In this chapter, previous relevant experimental, numerical, and analytical studies of supercritical flow instability and heat transfer are reviewed. These studies are divided into four categories: flow instability experiments, one-dimensional and analytical instability analyses, CFD instability analyses, and turbulence and heat transfer analyses of supercritical flow.

#### **2.2 Flow Instability Experiments**

Daney et al. (1979) performed an experiment to obtain the thermally-induced flow oscillations in supercritical helium. In their experiment, supercritical helium was flowing in a long, heated channel. They observed density-wave oscillations, during which the outlet temperature and the inlet mass flow rate of the channel oscillated in phase.

Fukuda et al. (1991) conducted an experimental study on the instability of supercritical helium flowing in a spiral tube. The pressure and the mass flux were kept constant, while the heat flux was changed. They observed three types of oscillations. Type A was accompanied by the oscillations of inlet and outlet pressure and not the temperature. Type B was accompanied by both temperature and pressure oscillations. Type C was accompanied by both temperature and pressure oscillations but with lower periods than type B. They concluded that Type A is a Helmholtz instability caused by the compressibility in the tubing, while types B and C are density-wave oscillations caused by large changes in physical properties.

Xiong et al. (2012) performed an experimental study on the instability of supercritical water in parallel channels. In their experiment, the heat flux was increased gradually and other parameters were kept constant to obtain possible instability boundaries. According to their observations, the flow rates of the two channels started oscillating out of phase as the heat flux reached the instability threshold. Their experimental work confirmed that the increase in the system pressure stabilizes the system. However, they suggested that further development on experimental techniques was needed to observe the non-monotonic effect of inlet temperature on the instability threshold.

Overall, experimental studies on stability of supercritical flow in heated channels are limited. The studies of Daney et al. (1979) and Fukuda et al. (1991) were conducted using supercritical helium. However, the focus of this study was the instability of supercritical water. Also, the study of Xiong et al. (2012) was performed using two parallel channels and was published after the objectives of the present study were defined. Therefore, the instability results of the present study are not compared with the experimental instability studies stated.

### **2.3 One-Dimensional and Analytical Instability Analyses**

The first comprehensive analytical study of various supercritical flow instability modes was reported by Zuber et al. (1966). They discussed the mechanisms that could induce thermo-hydraulic oscillations at supercritical pressures and suggested improvements to eliminate the onset of oscillations. Bouré et al. (1973) presented a classification of the different types of instabilities. They suggested that static instability (Ledinegg instability) can be described using only the steady-state equations. In this case, a small change in the flow conditions results in a new steady-state not equal to the original one. For dynamic

instabilities, such as density-wave oscillations, the steady-state equations are not sufficient to predict the system behavior or the threshold of instability. Yi et al. (2004) carried out a linear stability analysis to study the thermal-hydraulic stability of supercritical water in SCLWRs. They also performed a parametric study to determine the parameters affecting the flow stability. They concluded that, although a SCLWR has low coolant flow rates and large density changes in the core, the thermal-hydraulic stability can be achieved by applying an orifice pressure drop coefficient at the inlet of the fuel assemblies. Gomez et al. (2006) carried out a thermal-hydraulic stability analysis of supercritical water flowing in a uniformly heated channel, by extending the modeling approach used for the stability analysis of two-phase flow. They concluded that while density-wave oscillation can occur at supercritical pressures, Ledinegg instability and pressure drop oscillations (PDO) are not likely to occur in supercritical water systems. Ambrosini et al. (2006) reported the possibility of Ledinegg instability within a channel. They proposed dimensionless parameters for analyzing the stability of supercritical fluids based on classical phase-change and sub-cooling numbers adopted for boiling channels.

Chatoorgoon (2006) performed an analytical study of supercritical water stability in two horizontal parallel channels and concluded that instability in supercritical flow is different form instability in two-phase flow. He concluded that the threshold of oscillatory instability in parallel channels occurs close to the mass flow rate corresponding to  $\partial^2\Delta(p + \rho u^2)/\partial \dot{m}^2 = 0$ . Chatoorgoon (2013) performed a study to develop non-dimensional parameters for predicting the static instability boundary, using an in-house linear instability program. His non-dimensional parameters were examined for H<sub>2</sub>O and CO<sub>2</sub> with different inlet temperatures, inlet and outlet K factors, and system

pressures, flowing in a vertical pipe. He concluded that static instability is most likely to happen in vertical down-flow and least likely to occur in vertical up-flow, while the oscillatory instability can occur at higher temperatures in down-flow. Also, increasing the inlet temperature can either destabilize or stabilize the system depending on the K factors. When the inlet and outlet K-factors were low, increasing the inlet temperature destabilized the system, while in cases of high K-factors, increasing the inlet temperature stabilized the system. In addition, he concluded that above a certain temperature, static instability is not likely to occur.

Xiong et al. (2013) developed an in-house code by applying a time-domain approach and modeled the experimental study of Xiong et al. (2012). They compared the numerical and experimental results and concluded that the numerical code is capable of predicting the stability boundaries. Their results also showed that the inlet temperature has a non-monotonic effect on the power threshold.

#### **2.4 CFD Instability Analyses**

In recent years, there has been an increase in use of CFD (Computational Fluid Dynamics) simulations in stability analysis of supercritical flow. Sharabi et al. (2008) used FLUENT and applied the  $k-\varepsilon$  turbulence model with standard wall functions and with a low-Reynolds number model on a circular pipe. They compared the instability results with the ones predicted by linear and non-linear 1-D models and concluded that for flows at supercritical pressure, CFD confirms the occurrence of density wave oscillations at relatively large power-to-flow ratios. The results obtained using both turbulence models were in agreement with one-dimensional codes proposed by Ambrosini et al. (1999) and Idaho National Laboratory (INL) (1999). In another study,

Sharabi, et al. (2009) studied density-wave oscillations in triangular and square pitch rod bundles using the FLUENT code. They compared the results of instability thresholds and found good agreement between CFD and 1-D codes (Ambrosini et al., 1999 and INL, 1999). They also concluded that density-wave oscillations in triangular and square pitch rod bundles have similar characteristics to density-wave oscillations in circular channels.

In another study, Ampomah-Amoako and Ambrosini (2013) studied the performance of CFD in analyzing the supercritical flow stability. They used the STAR-CCM+ code and compared the CFD instability threshold results with the results of their in-house 1-D code (Ambrosini et al., 1999) for a circular pipe, as well as a triangular and a square pitch rod bundle slices. Their work confirmed the occurrence of both static and dynamic instabilities depending on the inlet fluid sub-cooling. To find the instability boundary, Ampomah-Amoako and Ambrosini first chose an inlet mass flow boundary condition to obtain the steady-state condition. Then the boundary was changed to a stagnation inlet with an assigned value of pressure upstream of the inlet section, while preserving the value of flow rate obtained in the steady-state solution. The power was then increased in steps while searching for instability at each step. The problem with this method is that a constant pressure drop is imposed at the inlet of the channel for different powers, without considering the fact that changing the power changes the pressure drop as well.

In a very recent study, Xi et al. (2014) carried out a 3-D numerical simulation of two heated parallel channels with supercritical water using CFX4, to find the instability boundaries. They used the geometry of Xiong et al. (2012) and performed a parametric study on the effect of inlet temperature, gravity, and system pressure on the instability threshold. Two turbulence models (the standard  $k-\varepsilon$  and SST models) were used in their

study. They concluded that the instability boundary results of the SST model are more conservative than the standard  $k-\varepsilon$  model. However, to save computational time, they continued the simulations using the  $k-\varepsilon$  model. They also compared their results of instability thresholds with the experimental results of Xiong et al. (2012). They concluded that their 3-D model is capable of predicting the onset of instability in better agreement with the experiment than the 1-D code developed by Xiong et al. (2013). However, in their simulations, the numbers of nodes were 360000 and 580000 when using the  $k-\varepsilon$  and the SST models, respectively, which are very small considering their geometry (two channels each with a length of 3 m and a diameter of 6 mm). Also, they used special coupling methods for pressure and velocity, which are required when the code has an uncoupled solver, which was employed in their older version of CFX. The newer version of CFX (i.e. CFX5) does not require a coupling method, since CFX5 is a fully coupled solver and therefore, the pressure-velocity coupling is inherent in the solution of the mass and momentum equation set. In addition, to find the instability boundary, they kept the total inlet mass flow rate constant and monitored the outlet mass flow rate during time with the increase of heat flux. Therefore, a constant pressure drop was imposed at the channel for different heat fluxes, as in the study of Ampomah-Amoako and Ambrosini (2013), without taking into account the variation of pressure drop with the power change.

## **2.5 Turbulence and Heat Transfer Analyses of Supercritical Flow**

The heat transfer deterioration phenomenon has been studied through both experimental and numerical methods. Shitsman (1963), Ornatskii et al. (1971), and Yamagata et al. (1972) have done experimental studies to analyze the heat transfer deterioration (HTD)

phenomenon at supercritical pressures. Bourke et al. (1971), Rodney et al. (1964) and Kurganov et al (1986) used pitot tubes and hot wire anemometers to measure turbulence properties in circular tubes with CO<sub>2</sub> flowing upward. Their result showed an M-shaped axial velocity profile, which is consistent with the fact that the supercritical fluid density decreases close to the wall and causes acceleration in the flow near the wall. Other experimental studies have been comprehensively reviewed by Duffey and Piro (2005). Bae et al. (2005) conducted direct numerical simulations (DNS) on supercritical CO<sub>2</sub> flowing upward and downward in vertical tubes, subjected to heating from the wall. Their study produced detailed information on turbulence and thermal characteristics of the flow. Palko and Anglart (2008) performed a numerical investigation of the HTD phenomena. They suggested that buoyancy is the phenomenon that governs the HTD, especially for relatively low coolant flow rates and high heat fluxes. They also claimed that the RANS low-Re turbulence modeling approach is fully capable of simulating the heat transfer characteristics of supercritical flow. Kao et al. (2010) used CFD and applied Reynolds Stress Model (RSM) with enhanced wall treatments. Their simulations confirmed the occurrence of the HTD phenomenon and predicted the peak of wall temperature and the minimum of heat transfer coefficient, consistent with Shitsman's experiment (1963). They suggested that the increase in both inlet temperature and operational pressure is effective in relaxing the heat transfer deterioration.

Mohseni and Bazargan (2010) developed a 2-D CFD code to examine a number of low Reynolds number  $k$ - $\epsilon$  turbulence models in the conditions of heat transfer enhancement and deterioration. They concluded that the results are quite sensitive to the choice of the turbulence model, especially in the deteriorated regime of heat transfer. However, their

work showed that the peak of wall temperature, which occurred in the deteriorated regime of heat transfer, was over-predicted regardless of the turbulence model used. They also mentioned the choice of the turbulent Prandtl number ( $Pr_t$ ) as one of the sources of uncertainty in modeling the HTD. In another work, Bazargan and Mohseni (2011) investigated the effect of  $Pr_t$  on convection heat transfer of supercritical flow. They examined both constant and variable values of  $Pr_t$  and concluded that the buoyancy effect in upward supercritical flow causes the  $Pr_t$  to decrease.

Jaromin and Anglart (2013) used ANSYS CFX and performed a numerical study of heat transfer to supercritical water. They compared the results of wall temperature with experimental data of Shitsman (1963) and Ornatsky (1971) and concluded that the SST turbulence model is capable of predicting the onset of heat transfer deterioration. Their study also showed that  $Pr_t$  has a significant influence on the results of wall temperature.

The studies on heat transfer characteristics and turbulence of supercritical flow have been comprehensively reviewed by Yoo (2013). Yoo concluded that despite a number of experimental studies on heat transfer to SC flow and various correlations proposed, there has been no single correlation capable of describing deteriorated or enhanced heat transfer to SC fluid flowing in vertical circular tubes. The numbers of studies on the fluid mechanics of SC flow are limited due to technical difficulties and high expenses required for measuring velocity and temperature fields. He also mentioned that in CFD modeling of SC flow, the turbulence models are capable of reproducing turbulence recovery in cases of high buoyancy, but not the improvement in heat transfer, due to using constant values of  $Pr_t$ . Since carrying out Direct Numerical Simulation (DNS) for complex geometries and high Reynolds numbers is expensive and time-consuming, he suggested

using LES or developing more accurate turbulence models capable of producing a more accurate prediction of variable thermo-physical properties.

## **2.6 Summary of the Literature Review**

From this literature review it can be seen that the majority of the numerical works done on supercritical flow were focused on its heat transfer characteristics. The instability analyses were also mainly done using 1-D codes. The authors who used CFD to analyze the instability of supercritical flow are Sharabi et al. (2008, 2009), Ampomah-Amoako and Ambrosini (2013), and Xi et al. (2014). In the first two studies, only the  $k-\varepsilon$  turbulence model and a low-Reynolds number model were used. While in the third study by Xi et al. (2014), there are some uncertainties regarding the number of nodes and the coupling method used. In addition, in these studies, a constant pressure drop was imposed at the channel for different heat fluxes, without considering the variation of pressure drop with the power change. Also, the effect of  $Pr_t$  on the flow instability was not discussed in these studies.

## **2.7 Objectives of the Present Work**

The objectives of this study are to:

1. Investigate the supercritical flow instability (both static and oscillatory instabilities) in a vertical heated channel with up-flow and without inlet and outlet plena, using proper boundary conditions, with the ANSYS CFX v.14.5 code
2. Compare the results of instability threshold between the two turbulence models used (the  $k-\varepsilon$  and the SST models)
3. Compare the CFD predictions of flow instability threshold with the 1-D solutions

4. Assess Chatoorgoon's condition (2013), proposed for channels with plena, and Ledinegg's condition (1938) for static instability
5. Assess Chatoorgoon's condition (2006) for oscillatory instability, proposed for channels with plena
6. Assess the effect of turbulent Prandtl number on the instability threshold
7. Perform heat transfer and pressure drop studies for validation of the CFD code
8. Discuss the findings and make recommendations

## CHAPTER 3

### MODEL DESCRIPTION FOR STABILITY ANALYSIS

#### 3.1 Geometry

The geometry shown in Figure 3.1 consists of a single circular vertical pipe with a length of 4.2672 m (as in proposed reactor designs) and a diameter of 8.36 mm, with a uniform heat flux applied at the wall. It is the same geometry used in previous CFD instability studies (Sharabi et al., 2008 and Ampomah-Amoako and Ambrosini, 2013). In some of the cases, an extra length of 0.0328 m is added at the outlet of the pipe for introducing a local pressure drop coefficient. In this study, only up-flow is considered and there is no inlet or outlet plenum, while the actual reactor design includes inlet-outlet plena. Cross section view of the geometry is also shown in Figure 3.2.

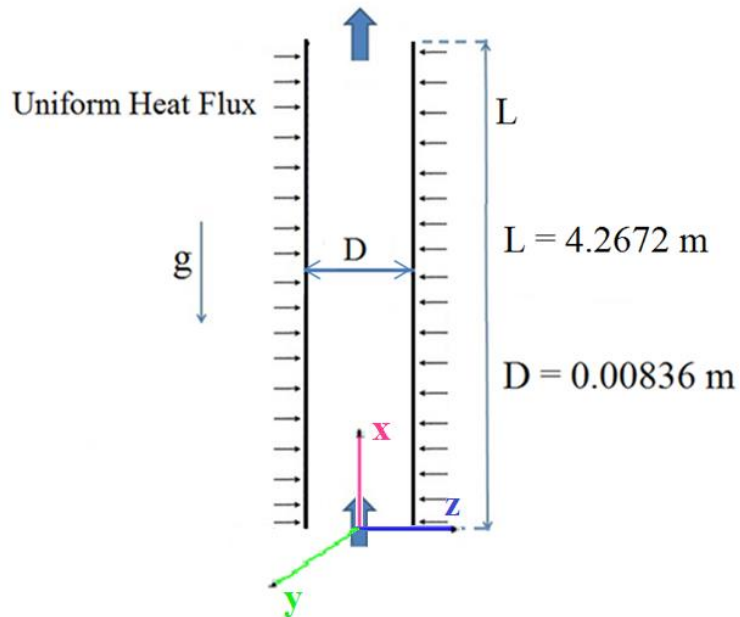


Figure 3.1: Geometry of the vertical pipe used for simulations

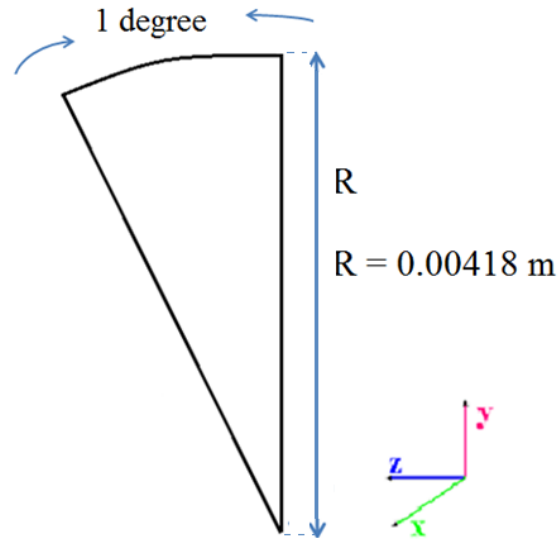


Figure 3.2: Cross section view of the geometry used for simulations

### 3.2 Assumptions

The following assumptions are made in the formulation of the governing equations of mass, momentum, and energy conservation.

- The flow is steady, two-dimensional and axisymmetric.
- The fluid is Newtonian.
- The flow is turbulent.
- Thermal radiation and combustion heat transfer are negligible and heat transfer is due to convection and conduction only.
- A constant, uniform heat flux is applied on the surface of the channel.
- Walls have no roughness.
- The eddy-viscosity approximation is used to model the Reynolds stresses.

### 3.3 Property Variation

In CFX, properties of water are calculated based on thermodynamic properties of water and steam from IAPWS-IF97, formulated by Wagner et al. (2000). The IAPWS-IF97

database provides an accurate equation of state for water and steam properties as well as an increase in computational speed.

Figure 3.3 shows five distinct thermodynamic regions for water and steam in IAPWS data base. They are as follows:

Region 1 (Sub-cooled Water): Water at a temperature lower than the saturation temperature at a given pressure;

Region 2 (Supercritical water/steam): Water at a temperature and pressure above its critical point;

Region 3 (Superheated steam): Steam at a temperature that is higher than its vaporization (boiling) point at a given pressure;

Region 4: Saturation data;

Region 5 (High temperature steam): Steam with a temperature up to 2000 °C and a pressure below 10 MPa.

It is noteworthy that Region 5 is not implemented in ANSYS CFX.

The entire sets of equations of IAPWS-IF97 have a limited range of validity. The range of validity for this property package as implemented in CFX is as follows:

$$0^{\circ}\text{C} < T \leq 800^{\circ}\text{C} \quad \text{for} \quad 10\text{MPa} \leq P \leq 100\text{MPa}$$

and

$$800^{\circ}\text{C} < T < 2000^{\circ}\text{C} \quad \text{for} \quad P < 10\text{MPa}$$

Temperature and pressure should be kept in the range of validity of IAPWS.

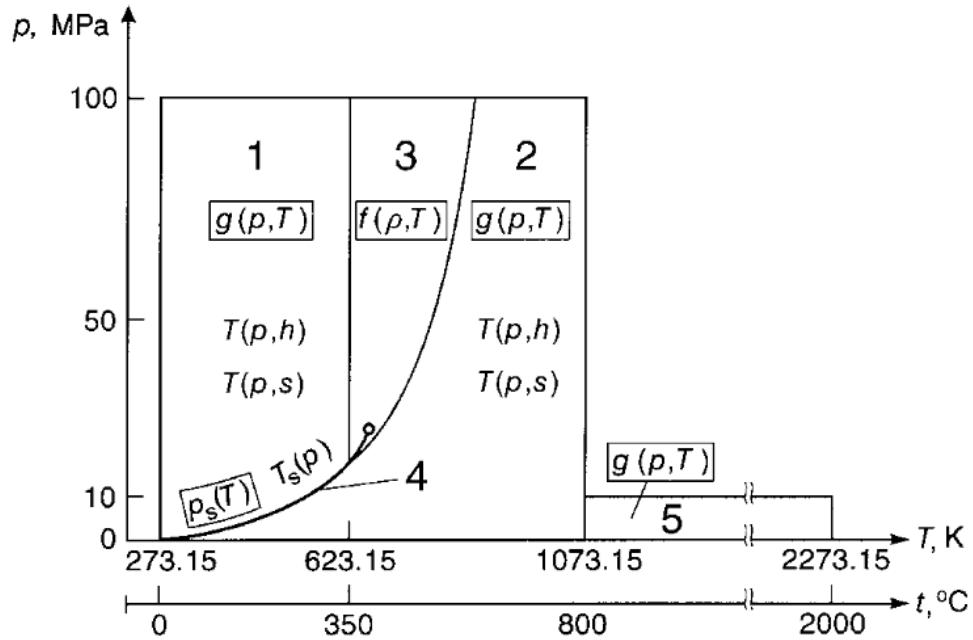


Figure 3.3: Regions and equations of IAPWS (ANSYS CFX-Solver Theory Guide, 2013)

### 3.4 Parameters defined

The parameters that are used to define the model are:

- Length: The length of the heated pipe is 4.2672 m for all of the cases. In case of having an outlet K factor, an extra unheated length of 0.0328 m is added at the outlet of the pipe, to introduce a pressure drop coefficient.
- Diameter: Diameter is equal to 8.36 mm for all of the cases.
- Properties: The working fluid used in the study is water at supercritical pressure based on IAPWS-IF97 (Wagner et al., 2000).
- Gravity:  $g_x = -9.81 \frac{m}{s^2}$ ,  $g_y = g_z = 0$
- Reference pressure: A reference pressure of 25 MPa is specified for all of the cases, since SCWR is designed to operate at 25 MPa (U.S. DOE Nuclear Energy Research Advisory Committee and the Generation IV International Forum, 2002).

- Buoyancy reference density: A buoyancy reference density of  $500 \text{ kg/m}^3$  is specified for all of the cases. Changing the value of buoyancy reference density changes the value of the modified pressure and the hydrostatic pressure, such that the summation of these two pressure terms which is the static pressure remains unchanged.
- Inlet turbulence intensity: In all the steady-state cases modeled, the value of turbulence intensity is set to 5%.
- K factor: In the cases with outlet K factors, loss coefficients are introduced in the subdomain.
- $Pr_t$ : In the present study, for all of the cases, a constant  $Pr_t$  equal to 0.95 is selected for the simulations. Another value of  $Pr_t$  equal to 0.7 is also used in some of the cases to examine the effect of  $Pr_t$  on the instability threshold.

The other independent parameters are inlet temperature, inlet mass flow rate, and wall heat flux. These parameters will be discussed in section 3.7.

### 3.5 Governing Equations

The equations for conservation of mass, momentum, and energy are written in Cartesian coordinates as follows:

Continuity Equation:

$$\frac{\partial(\rho)}{\partial t} + \frac{\partial(\rho U_j)}{\partial x_j} = 0 \quad (3.1)$$

Momentum Conservation Equation:

$$\begin{aligned} & \left( \frac{\partial(\rho U_i)}{\partial t} \right) + \left( \frac{\partial(\rho U_j U_i)}{\partial x_j} \right) \\ & = -\frac{\partial P'}{\partial x_i} + \frac{\partial}{\partial x_j} \left( (\mu + \mu_t) \left[ \frac{\partial U_i}{\partial x_j} + \frac{\partial U_j}{\partial x_i} \right] \right) + S_{M,buoy} + S_{M,loss} \end{aligned} \quad (3.2)$$

where  $S_{M,buoy}$  and  $S_{M,loss}$  are momentum source terms and will be discussed in Section 3.5.1.  $P'$  is the modified pressure and is equal to the following:

$$P' = p + \frac{2}{3}\rho k \quad (3.3)$$

A total energy equation is preferred over the thermal energy equation since the flow is compressible and the total energy formulation gives a more accurate solution by including the mechanical energy.

$$\begin{aligned} & \left( \frac{\partial(\rho h_{tot})}{\partial t} \right) + \left( \frac{\partial(\rho U_j h_{tot})}{\partial x_j} \right) \\ & = \frac{\partial}{\partial x_j} \left( (\lambda + \frac{\mu_t}{Pr_t}) \frac{\partial h}{\partial x_j} + \frac{\partial}{\partial x_j} (U_j [\tau_{ij} - \rho \overline{u_i u_j}]) \right) + U_j \cdot S_M \end{aligned} \quad (3.4)$$

where  $h_{tot}$  is the total enthalpy and is related to the static enthalpy, mechanical energy, and turbulence kinetic energy (for turbulence models in which turbulence kinetic energy is available, e.g.  $k-\varepsilon$ ,  $k-\omega$ , SST, and so on) using the following:

$$h_{tot} = h + \frac{1}{2} U_i U_i + k \quad (3.5)$$

where  $h$  is the static enthalpy. The turbulence kinetic energy is modeled using:

$$k = \frac{1}{2} \overline{u_i u_i} \quad (3.6)$$

where  $u$  is the fluctuating velocity component in turbulent flow.

In Equation (3.4),  $\frac{\partial}{\partial x_j} (U_j [\tau_{ij} - \rho \overline{u_i u_j}])$  is the viscous work term, which is due to viscous shear in the fluid. It is included in the total energy equation due to compressibility of the flow, although its effect is negligible. Also  $U_j S_M$  represents the work due to the external momentum source.

Value of the turbulent Prandtl number used in this study will be discussed in Chapter 5. In this study, both steady-state and transient (time-varying) solutions of the governing equations were performed.

### 3.5.1 Momentum Source terms

#### **Buoyancy**

A source term is added to the momentum equation for buoyancy calculations.

$$S_{M,buoy} = (\rho - \rho_{ref}) g_i \quad (3.7)$$

where  $g_i = -9.8 \text{ m/s}^2$  for  $i = 1$ , and  $g_i = 0$  for  $i = 2$  and  $3$ , where indices 1, 2, and 3 correspond to the  $x$ ,  $y$ , and  $z$  directions. The axial direction is  $x$ .

In CFX, when buoyancy is activated, the pressure in the momentum equation excludes the hydrostatic gradient due to  $\rho_{ref}$ . Then, the pressure term in the momentum equation is called the modified pressure. This term will be explained further in Chapter 5. Depending on the physics of the flow, either the Full Buoyancy model or the Boussinesq model is used to represent  $(\rho - \rho_{ref})$ . The Full Buoyancy model is used when density varies and Boussinesq model relates density change to temperature change. Because the density of water at supercritical pressure varies with temperature and pressure, the full buoyancy model was applied in the simulations in this work.

### Isotropic loss

An additional source term was added to the momentum equation, which is responsible for the isotropic loss. The isotropic loss is modeled as follows:

$$S_{M,loss,1} = -\frac{\mu}{K_{perm}}U_1 - K_{loss}\frac{\rho}{2}|U|U_1 \quad (3.8)$$

where  $K_{perm}$  is the permeability and  $K_{loss}$  is the loss coefficient.

Permeability is defined as the ability of a domain to allow the fluid to flow through. This term in the isotropic loss is responsible for viscous loss.  $K_{perm}$  was set to infinity ( $10^{30}$ ) to omit the role of the viscous loss in the momentum equation source term, so that:

$$\frac{\mu}{K_{perm}}U_1 \approx 0 \quad (3.9)$$

By omitting the viscous loss, Equation (3.8) becomes:

$$S_{M,loss,1} = -K_{loss}\frac{\rho}{2}|U|U_1 \quad (3.10)$$

$K_{loss}$  in Equation (3.10) is responsible for inertia losses. To specify a value for isotropic loss, a fluid subdomain with adiabatic wall was added to the main domain. The fluid subdomain had a very short length (0.0328 m) and therefore the variation of velocity in the  $x$  direction was negligible. The effect of gravity and shear stress is also negligible in this region.

By neglecting the effect of velocity variation, shear stress and gravity in the subdomain, the momentum equation for steady-state condition becomes:

$$-\frac{\partial P}{\partial x_i} + S_{M,loss,x} = 0 \quad (3.11)$$

Writing Equation (3.11) in the  $x$  direction, it becomes:

$$\frac{\partial P}{\partial x_1} = -K_{loss} \frac{\rho}{2} |U|U_1 \quad (3.12)$$

Using a linear approximation, Equation (3.12) becomes:

$$-\Delta P = 0.0328 K_{loss} \frac{\rho}{2} |U|U_1 \quad (3.13)$$

where 0.0328 is the length of the subdomain.

Equation (3.13) allows introducing the desired pressure drop into the momentum equation by specifying the  $K_{loss}$ . The value of  $0.0328 K_{loss}$  in this study is equivalent to the local pressure drop coefficient (K factor) in 1-D codes. In the following chapters, the K factor will be presented in flow condition specifications, to be consistent with 1-D codes.

### 3.6 Turbulence Closure

Turbulence models allow the calculation of the mean flow without first calculating the full time-dependent flow field. On the other hand, Direct Numerical Simulation (DNS) resolves all scales of turbulence by solving the Navier-Stokes equations numerically without any turbulence modeling. Due to approximations in turbulence modeling, the accuracy of the solution decreases in return for reduction in the computational costs, compared to Direct Numerical Simulation (DNS). There are ten unknown quantities in isothermal turbulent flow problems: the velocity variations in  $x$ ,  $y$  and  $z$  directions, the pressure variation, and the six Reynolds stresses. On the other hand, there are only four equations for the flow field: the momentum equations in three directions and the continuity equation. Therefore, turbulence modeling is required to close the system of equations. Turbulence models provide approximations for the six unknown Reynolds stresses. In the following, the formulation and application of two turbulence models used

in the present study are described: the standard  $k-\varepsilon$  model by Launder and Sharma (1974) with a scalable wall-function and the  $k-\omega$  based SST model by Menter (1993). The eddy viscosity modeling approach has been used.

### 3.6.1 The $k-\varepsilon$ Turbulence Model

The  $k-\varepsilon$  model is one of the most commonly used models and includes two extra transport equations to represent the turbulent properties of the flow. These equations are the turbulence kinetic energy,  $k$  and the turbulent dissipation rate,  $\varepsilon$ . The standard  $k-\varepsilon$  model with a scalable wall-function was used to solve  $\mu_t$  with the following relation:

$$\mu_t = C_\mu \rho \frac{k^2}{\varepsilon} \quad (3.14)$$

where  $C_\mu$  is a constant and the values of turbulence kinetic energy,  $k$ , and the dissipation,  $\varepsilon$ , come from the solution to the following transport equations:

$$\frac{\partial(\rho k)}{\partial t} + \frac{\partial(\rho U_j k)}{\partial x_j} = \frac{\partial}{\partial x_j} \left( \left( \mu + \frac{\mu_t}{\sigma_k} \right) \frac{\partial k}{\partial x_j} \right) + P_k - \rho \varepsilon + P_{kb} \quad (3.15)$$

$$\frac{\partial(\rho \varepsilon)}{\partial t} + \frac{\partial(\rho U_j \varepsilon)}{\partial x_j} = \frac{\partial}{\partial x_j} \left( \left( \mu + \frac{\mu_t}{\sigma_\varepsilon} \right) \frac{\partial \varepsilon}{\partial x_j} \right) + \frac{\varepsilon}{k} (C_{\varepsilon 1} P_k - C_{\varepsilon 2} \rho \varepsilon + C_{\varepsilon 1} P_{\varepsilon b}) \quad (3.16)$$

The turbulence production term,  $P_k$ , is modeled using:

$$P_k = \mu_t \left( \frac{\partial U_i}{\partial x_j} + \frac{\partial U_j}{\partial x_i} \right) \frac{\partial U_i}{\partial x_j} - \frac{2}{3} \frac{\partial U_k}{\partial x_k} \left( 3\mu_t \frac{\partial U_k}{\partial x_k} + \rho k \right) \quad (3.17)$$

When flow is compressible,  $\frac{\partial U_k}{\partial x_k}$  is large only in regions with high velocity divergence, such as shocks. Therefore, in the current flow condition, the second term on the right hand side of Equation (3.17) does not contribute significantly to the production.

The values for the standard  $k$ - $\varepsilon$  equation constants used in this work are:

$$C_\mu = 0.09, C_{\varepsilon 1} = 1.44, C_{\varepsilon 2} = 1.92, \sigma_k = 1.0, \text{ and } \sigma_\varepsilon = 1.3.$$

$P_{kb}$  and  $P_{\varepsilon b}$  in Equations (3.15) and (3.16) represent the influence of buoyancy forces. They are included in the  $k$  equation when the buoyancy turbulence is set to ‘Production and Dissipation’ in CFX (ANSYS CFX-Solver Theory Guide, 2013).

For the Full buoyancy model, the buoyancy production term,  $P_{kb}$ , is modeled using:

$$P_{kb} = -\frac{\mu_t}{\rho\sigma_\rho} g_i \frac{\partial\rho}{\partial x_i} \quad (3.18)$$

where  $\sigma_\rho$  is the turbulent Schmidt number and is equal to 1 for the Full buoyancy model.

The buoyancy dissipation term,  $P_{\varepsilon b}$ , is assumed to be proportional to  $P_{kb}$  as follows:

$$P_{\varepsilon b} = C_3 \cdot \max(0, P_{kb}) \quad (3.19)$$

where  $C_3$ , the dissipation coefficient, is equal to 1.

### 3.6.2 The Shear Stress Transport (SST) Turbulence Model

The  $k$ - $\omega$  based SST turbulence model is a two-equation eddy-viscosity model. The SST model benefits from the performance of both the  $k$ - $\varepsilon$  and the  $k$ - $\omega$  models in different regions of the flow. The  $k$ - $\varepsilon$  model performs well in the free-stream region, while the  $k$ - $\omega$  model developed by Wilcox (1988), performs well in the near-wall region and has a strong sensitivity to free-stream conditions (Menter, 1994). Therefore, the SST model uses the  $k$ - $\omega$  formulation in the inner parts of the boundary layer and switches to the  $k$ - $\varepsilon$  formulation in the free-stream. For this purpose, two blending functions,  $F_1$  and  $F_2$  are introduced in the turbulent frequency equation and turbulent viscosity term, respectively.  $F_1$  and  $F_2$  functions are equal to one near the surface and decreases to zero outside the boundary layer to incorporate the switch between the two models.

The modeled equations for the turbulence kinetic energy,  $k$  and turbulent frequency,  $\omega$ , are as follows:

$$\frac{\partial(\rho k)}{\partial t} + \frac{\partial(\rho U_j k)}{\partial x_j} = P_k - \beta' \rho k \omega + \frac{\partial}{\partial x_j} \left( \left( \mu + \frac{\mu_t}{\sigma_{k3}} \right) \frac{\partial k}{\partial x_j} \right) + P_{kb} \quad (3.20)$$

$$\begin{aligned} \frac{\partial(\rho \omega)}{\partial t} + \frac{\partial(\rho U_j \omega)}{\partial x_j} \\ = \alpha_3 \frac{\omega}{k} P_k - \beta_3 \rho \omega^2 + \frac{\partial}{\partial x_j} \left( \left( \mu + \frac{\mu_t}{\sigma_{\omega 3}} \right) \frac{\partial \omega}{\partial x_j} \right) + 2\rho(1 - F_1) \frac{1}{\sigma_{\omega 2} \omega} \frac{\partial k}{\partial x_j} \frac{\partial \omega}{\partial x_j} + P_{\omega b} \end{aligned} \quad (3.21)$$

The turbulent viscosity is modeled using:

$$\mu_t = \rho \frac{\alpha_1 k}{\max(\alpha_1 \omega, S F_2)} \quad (3.22)$$

where  $S$  is modeled using:

$$S = (2 S_{ij} S_{ij})^{\frac{1}{2}} \quad (3.23)$$

where

$$S_{ij} = \frac{1}{2} \left( \frac{\partial U_i}{\partial x_j} + \frac{\partial U_j}{\partial x_i} \right) \quad (3.24)$$

The turbulence production term,  $P_k$ , is defined in Equation (3.17).

The blending functions are as follows:

$$F_1 = \tanh(\text{arg}_1^4) \quad (3.25)$$

$$\text{arg}_1 = \min \left( \max \left( \frac{\sqrt{k}}{\beta' \omega y}, \frac{500 \nu}{y^2 \omega} \right), \frac{4\rho k}{C D_{k\omega} \sigma_{\omega 2} y^2} \right) \quad (3.26)$$

$$CD_{k\omega} = \max\left(2\rho \frac{1}{\sigma_{\omega 2}\omega} \frac{\partial k}{\partial x_j} \frac{\partial \omega}{\partial x_j}, 1.0 \times 10^{-10}\right) \quad (3.27)$$

$$F_2 = \tanh(\text{arg}_2^2) \quad (3.28)$$

$$\text{arg}_2 = \max\left(\frac{2\sqrt{k}}{\beta'\omega y}, \frac{500\nu}{y^2\omega}\right) \quad (3.29)$$

where  $y$  is the distance from the nearest surface and  $\nu$  is the kinematic viscosity.

The buoyancy production term is included in the  $k$ -equation with the same formulation as the  $k$ - $\varepsilon$  model.

$$P_{kb} = -\frac{\mu_t}{\rho\sigma_\rho} g_i \frac{\partial \rho}{\partial x_i} \quad (3.30)$$

The buoyancy turbulence for the  $\omega$ -equation is as follows:

$$P_{\omega b} = \frac{\omega}{k} ((\alpha + 1)C_3 \max(P_{kb}, 0) - P_{kb}) \quad (3.31)$$

The coefficients of  $\alpha, \beta, \sigma_k$  and  $\sigma_\omega$  are a linear combination of coefficients in the underlying models, using the following:

$$\emptyset_3 = F_1 \emptyset_1 + (1 - F_1)\emptyset_2 \quad (3.32)$$

where

$$\emptyset = \alpha, \beta, \sigma_\omega, \sigma_k \quad (3.33)$$

The values for the SST equation constants used in this work are:

$$\beta' = 0.09, \alpha_1 = 5/9, \beta_1 = 0.075, \sigma_{k1} = 2, \sigma_{\omega 1} = 2, \alpha_2 = 0.44, \beta_2 = 0.0828, \alpha_{k2} = 1,$$

$$\alpha_{\omega 2} = \frac{1}{0.856}, C_3 = 1 \text{ and } \sigma_\rho = 1.$$

### 3.6.3 Wall Function

The near-wall region can be subdivided into viscous sub-layer where viscosity plays an important role in momentum and heat transfer and the logarithmic layer where turbulence is dominant. In log-layer, the shear stress could be numerically computed as a function of the velocity at a given distance from the wall which is known as the wall function.

The  $y^+$  value is a non-dimensional distance from the wall to the first mesh node. To use a proper wall function for a particular turbulence model,  $y^+$  values should be within a certain range. The upper range of applicability will vary depending on the flow physics and the extent of the boundary layer profile. The standard wall function in ANSYS CFX is an extension of the method of Launder and Spalding (1974).

The logarithmic relation for the near-wall velocity is given by:

$$u^+ = \frac{U_t}{u_\tau} = \frac{1}{\kappa} \ln(y^+) + C \quad (3.34)$$

where  $u^+$  is the near-wall velocity,  $u_\tau$  is the friction velocity,  $U_t$  is the velocity tangent to the wall at the distance of  $\Delta y$  from the wall,  $\kappa$  is the von-Karman constant, and  $C$  is a log-layer constant depending on the wall roughness ( $C = 5.2$  for a smooth wall).  $y^+$  and  $u_\tau$  are modeled using:

$$y^+ = \frac{\rho \Delta y u_\tau}{\mu} \quad (3.35)$$

$$u_\tau = \left( \frac{\tau_\omega}{\rho} \right)^{\frac{1}{2}} \quad (3.36)$$

where  $\tau_\omega$  is the wall shear stress.

### 3.6.3.1 Scalable Wall Function

The major discrepancy of the standard wall function approach is its dependence on the  $y^+$ , since refining the near-wall mesh (i.e.  $y^+ < 11$ ) does not give a unique solution of increasing accuracy (Grotjans and Menter, 1998). The use of scalable wall functions in ANSYS CFX for  $\varepsilon$ -equation based turbulence models takes care of this problem and produces consistent results for grids of varying  $y^+$ . The scalable wall function automatically activates the local usage of the log law in regions where the  $y^+$  is sufficiently small to resolve the boundary layer, and the standard wall function in the regions where the  $y^+$  is coarser. Therefore, the scalable wall function can be applied on fine grids as well.

When the near-wall velocity,  $U_t$ , approaches zero in logarithmic region, an alternative velocity scale,  $u^*$ , can be used instead of  $u_\tau$ , which is as follows:

$$u^* = C_\mu^{1/4} k^{1/2} \quad (3.37)$$

$u_\tau$  can be obtained using:

$$u_\tau = \frac{U_t}{\frac{1}{k} \ln(y^*) + C} \quad (3.38)$$

The value of  $\tau_\omega$  is obtained from:

$$\tau_\omega = \rho u^* u_\tau \quad (3.39)$$

where

$$y^* = (\rho u^* \Delta y) / \mu \quad (3.40)$$

The basic idea behind the scalable wall function approach is to limit the value of  $y^+$  used in the logarithmic formulation by a lower value of  $y^* = \max(y^*, 11.06)$ , where 11.06 is the value of  $y^*$  at the intersection between the logarithmic and the linear wall profile.

When using the  $k$ - $\epsilon$  turbulence model with a scalable wall function,  $y^+$  should be less than 300.

### 3.6.3.2 Automatic wall function

There are cases that require high near-wall resolution and the  $k$ - $\epsilon$  model is unable to handle low turbulent Reynolds number computations. Therefore, to solve the viscous sub-layer more precisely, the  $\omega$ -based models including the SST model with automatic near-wall treatment are preferable. Automatic near-wall treatment automatically switches from wall-functions to a low-Re near-wall formulation as the mesh is refined. The requirement of using this model is to have at least 10 nodes in boundary layer; in other words,  $y^+ < 2$  is required to have an accurate approximation of the boundary layer. In this study, when using the SST model, the value of  $y^+$  was around 0.1, to capture the near-wall behaviour of the flow thoroughly.

## 3.7 Boundary Conditions

### 3.7.1 Fluid Wall

No-slip condition was specified on the pipe wall. A uniform heat flux of  $893 \text{ kW/m}^2$  (equal to a power of 100 kW) was applied at the wall for all of the cases. The value of 100 kW is the typical value of power used in previous simulations. The attempt of this study was to find the instability boundary flow rate at a specific power. In addition, heat flux and mass flow rate at the instability boundary are connected together and changing the heat flux changes the instability boundary mass flow rate as well. Therefore, heat flux was held constant for all of the simulations.

### 3.7.2 Subdomain Fluid Wall

No-slip adiabatic condition was employed on the subdomain wall.

### 3.7.3 Inlet

The inlet turbulence kinetic energy was calculated using:

$$k_{inlet} = \frac{3}{2} (UI)^2 \quad (3.41)$$

where  $I$ , the turbulence intensity, was modeled using:

$$I = \frac{u}{U} \quad (3.42)$$

where  $u$  is the fluctuating velocity. The inlet dissipation was calculated using:

$$\varepsilon_{inlet} = \rho C_{\mu} \frac{k^2}{\mu_t} \quad (3.43)$$

The inlet frequency was calculated using:

$$\omega_{inlet} = \frac{\rho k}{\mu_t} \quad (3.44)$$

**Steady-State Solution:** For steady-state conditions, an inlet mass flow rate was specified. For all of the cases studied, a different range of flow rate was examined to find the mass flow rate in which instability occurred. Flow direction was set normal to the boundary and the corresponding inlet velocity was uniform across the inlet. Also, a medium turbulence intensity of 5% was specified at the inlet. For medium intensity of 5%, CFX defines a viscosity ratio ( $\mu_t / \mu$ ) equal to 10.

**Transient Solution:** For a time-varying analysis, the initial conditions were a converged steady-state solution. Also, a medium turbulence intensity of 5% was specified as an initial condition across all domains for the transient solution. In addition, the inlet boundary condition was changed to an inlet with an average pressure equal to the

pressure obtained from the steady-state solution. The corresponding flow and the turbulence condition were considered fully developed at the inlet.

In all cases, a uniform temperature was specified at the pipe inlet.

#### 3.7.4 Outlet

In all cases, at the pipe exit, an outlet condition with a static pressure equal to a reference pressure of zero was specified.

#### 3.7.5 Symmetry

The flow was assumed to be axisymmetric. Therefore, the solution domain was  $\frac{1}{360}$  of the pipe volume. Symmetry boundary conditions were placed on the faces at zero and 1 degrees.

#### 3.7.6 Domain Interface

A domain interface was defined between the main domain and the subdomain. This interface satisfied the conservation of mass, momentum, turbulence, and heat transfer between the two domains. There was a one-to-one model of the mesh at the domain interface.

## CHAPTER 4

### NUMERICAL SOLUTION METHOD FOR CFD ANALYSIS

#### 4.1 Introduction

In this chapter, the general solution procedure used by CFX to obtain numerical solutions to the governing differential equations is discussed. In addition, the results of mesh independence and validation tests are presented.

#### 4.2 Grid Generation

The solution domain is divided into many discrete volumes. This set of volumes is the computational mesh. The mesh was generated using ANSYS ICEM CFD v14.5 software. The diagram of the wedge-shaped solution domain with an angle of  $15^\circ$  is shown in Figure 4.1 (a). Figure 4.1 (b) shows a coarse grid with an angle of  $15^\circ$  to illustrate the concept of the grid used in the simulations. The steps that were taken to create the geometry and the mesh are explained in Appendix A.

Through different tests performed for the number of nodes in the angular direction, it was concluded that results are very sensitive to the number of angular nodes and to obtain a uniform solution of properties, a very fine resolution of mesh has to be applied in the angular direction. To reduce the computational costs, only  $\frac{1}{360}$  of the pipe volume was created since the flow was axisymmetric. Therefore, the main domain created is a wedge-shaped domain with an angle of  $1^\circ$ . A cross-sectional view of a typical coarse grid near the wall is shown in Figure 4.2. A non-uniform distribution of nodes was used to obtain refinement near the pipe wall.

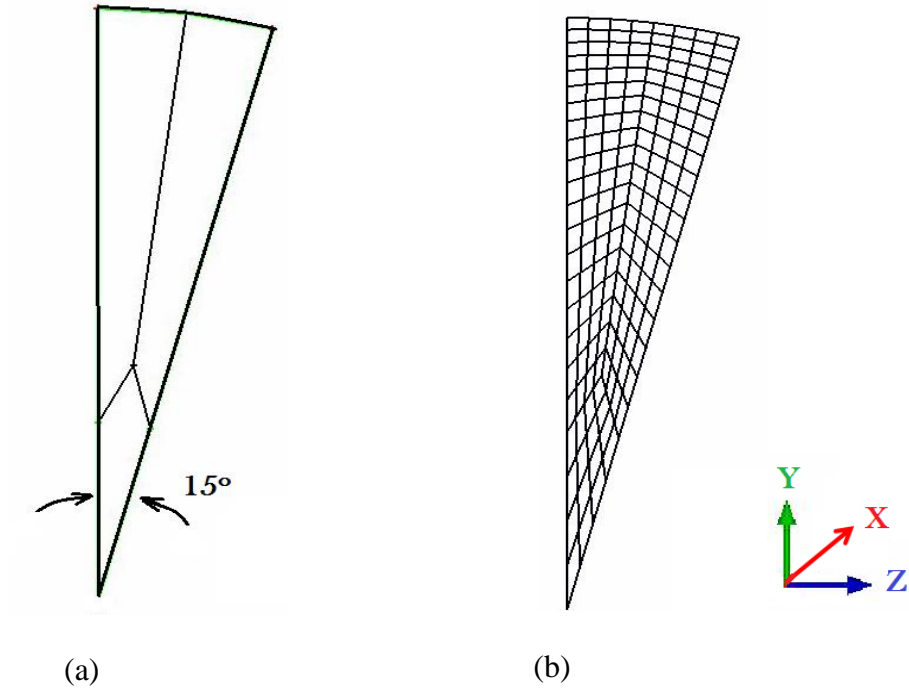


Figure 4.1: A cross sectional view of the a) geometry blocking and b) mesh

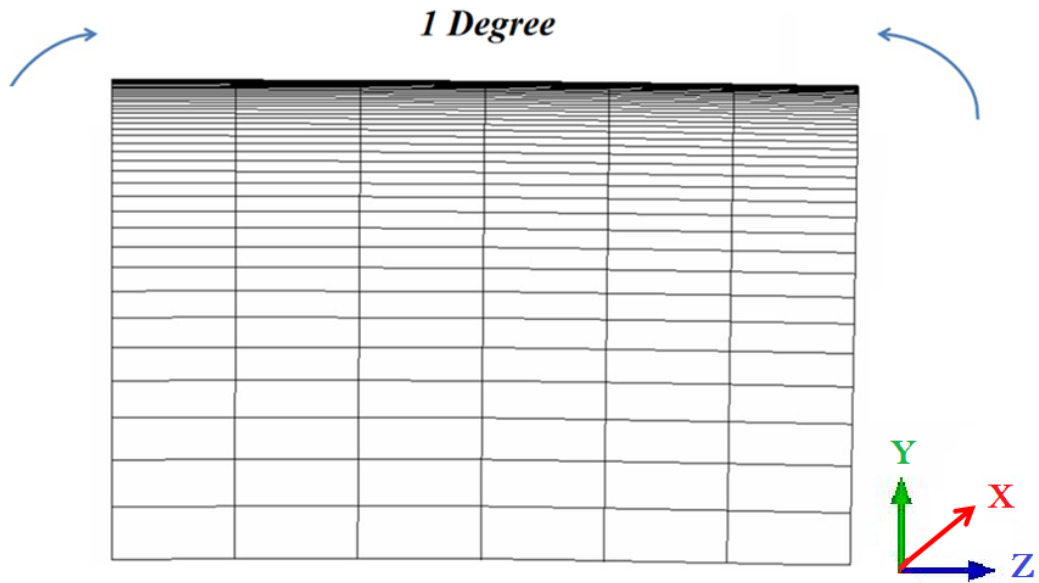


Figure 4.2: Near-wall treatment for a typical coarse mesh cross section

### 4.3 Numerical Solution Method

The governing equations were solved using ANSYS CFX v.14.5. CFX discretizes the spatial domain into finite control volumes and the governing equations are integrated

over each control volume, such that each quantity (mass, momentum, energy, etc.) is conserved for each control volume. All the governing equations possess the following general advection-diffusion form:

$$\underbrace{\frac{\partial}{\partial x_j} (\rho U_j \varphi)}_{\text{Advection term}} - \underbrace{\frac{\partial}{\partial x_j} \left[ \Gamma_\varphi \frac{\partial \varphi}{\partial x_j} \right]}_{\text{Diffusion term}} = \underbrace{S_\varphi}_{\text{Source term}} \quad (4.1)$$

where  $\varphi$  is the variable of interest,  $\Gamma_\varphi$  is the relevant diffusivity for  $\varphi$ , and  $S_\varphi$  is the source term. Advection is a transport mechanism of a substance by a fluid due to the fluid's bulk motion and requires the estimation of the field variable at an integral point (ip) on a control volume face. Determination of these face values requires the integration point values of  $\varphi$  to be approximated in terms of nodal values of  $\varphi$ . In ANSYS CFX, the advection scheme has the form:

$$\varphi_{ip} = \varphi_{up} + \beta \nabla \varphi \cdot \Delta \vec{r} \quad (4.2)$$

where  $\varphi_{up}$  is the value at the upwind node and  $\vec{r}$  is the vector from the upwind node to the ip. The high-resolution advection scheme based on the work of Barth and Jespersen (1989) was used to determine  $\beta$  at each node. The advective flux was evaluated using the values of  $\beta$  and  $\nabla \varphi$  from the upwind node.

Diffusion mechanism results in mixing or mass transport, without requiring bulk motion. To evaluate the diffusion terms (term 4 of Equation (3.2) and term 3 of Equation (3.4)), shape functions are used as following:

$$\frac{\partial \varphi}{\partial x} \Big|_{ip} = \sum_n \frac{\partial N_n}{\partial x} \Big|_{ip} \varphi_n \quad (4.3)$$

where  $\varphi_n$  is the value of  $\varphi$  at node  $n$ . The summation is over all nodes of the mesh element. The Cartesian derivatives of shape functions are expressed using Jacobian transformation matrix as follows:

$$\begin{bmatrix} \frac{\partial N}{\partial x} \\ \frac{\partial N}{\partial y} \\ \frac{\partial N}{\partial z} \end{bmatrix} = \begin{bmatrix} \frac{\partial x}{\partial s} & \frac{\partial y}{\partial s} & \frac{\partial z}{\partial s} \\ \frac{\partial x}{\partial t} & \frac{\partial y}{\partial t} & \frac{\partial z}{\partial t} \\ \frac{\partial x}{\partial u} & \frac{\partial y}{\partial u} & \frac{\partial z}{\partial u} \end{bmatrix}^{-1} \begin{bmatrix} \frac{\partial N}{\partial s} \\ \frac{\partial N}{\partial t} \\ \frac{\partial N}{\partial u} \end{bmatrix} \quad (4.4)$$

In early CFD codes, the scalar quantities were calculated at the cell centers and vector quantities were calculated at the cell faces. This method is known as staggered grid approach. In more recent codes, like ANSYS CFX, all variables are calculated at the cell centers. This method that is known as co-located grid approach has the advantage of needing only one mesh and the terms involved are simpler. However, co-located method leads to decoupled pressure field. To avoid that, CFX-5 uses a coupled solver based on the work of Rhie and Chow (1983), which solves the equations for velocity and pressure as a single system. This solution approach uses a fully implicit discretization of the equations at any given time step. For steady-state problems, the time-step behaves like a relaxation parameter and guides the approximate solutions to a steady-state solution. This reduces the number of iterations required to achieve a converged steady-state condition, or to calculate the solution for each time step in a time-dependent analysis, compared to a segregated solver. For transient analysis, multiple calculations of the linearized equations are performed at each time step.

In the present study, computations were done with double precision. Steady-state solutions were considered converged when the maximum normalized residual of each of

the discretized equations was less than  $1 \times 10^{-5}$  and the domain imbalance of equations solved was less than 0.01 %. The range of  $y^+$  for each turbulence model was discussed in Chapter 3. Since a lower value of  $y^+$  was used for the SST turbulence model, the convergence of the SST model was more difficult than the  $k-\varepsilon$  model and needed a smaller time step. For transient analyses, time step sizes of 0.1 s and 0.01 s were used for the  $k-\varepsilon$  and the SST models, respectively, and 10 full calculations were performed during each time step.

## CHAPTER 5

### GRID INDEPENDENCE AND VALIDATION TESTS

#### 5.1 Introduction

To validate the CFD simulation, experimental data related to instability of supercritical flow are needed. However, sets of experimental data on supercritical flow instability are only available for parallel channels and spiral tubes. Experimental studies have been performed on heat transfer, turbulence and pressure drop of supercritical flow. Therefore, for the purpose of this study, two experiments on the heat transfer of supercritical flow (Shitsman, 1963 and Ornatsky et al., 1971) and one experiment on the pressure drop of supercritical flow (Ishigai et al., 1981) were selected to validate the numerical model.

Shitsman's experiment was carried out using supercritical water flowing upward in a vertical circular pipe at low mass fluxes and relatively high heat fluxes, and the influence of buoyancy was significant. Shitsman was the first to observe a phenomenon called the heat transfer deterioration (HTD) at supercritical pressures. The experiment by Ornatsky et al. was also performed using supercritical water flowing upward in a vertical circular pipe. This experiment was also carried out in the deteriorated region of heat transfer, but with a very high coolant flow rate where the effect of buoyancy was not as significant.

There are not many experimental studies of total pressure drop of supercritical flow in a tube and there is a need for more experimental data in this area. One of the few experiments in this area is a work done by Ishigai et al., where they obtained experimental data of frictional pressure drop for supercritical pressure water flowing upward in uniformly heated tubes.

## 5.2 Heat Transfer Deterioration Phenomenon

In general, due to the significant variation of thermo-physical properties near the critical and the pseudo-critical points, supercritical fluid may experience three modes of heat transfer: normal heat transfer, deteriorated heat transfer, and improved heat transfer, depending on the operating conditions (Piro and Mokri, 2011).

Improved heat transfer is characterized by higher values of the heat transfer coefficient (HTC) and hence lower values of wall temperature in some parts of the heated channel or within the entire channel, compared to the normal heat transfer mode.

Heat transfer deterioration, on the other hand, is characterized by lower values of HTC and therefore higher values of temperature near the wall, compared to the normal heat transfer mode. This mode of heat transfer may happen in some parts of the heated channel, or within the entire channel and may be due to several reasons. The HTD may happen at either low mass flow rates due to the effect of buoyancy, or at high mass flow rates due to flow acceleration. In the case of a low mass flow-rate, the strong change of temperature near the wall leads to a large variation of density. Therefore, a large buoyancy force induced acts to accelerate the near-wall fluid. The increase in velocity near the wall flattens the velocity profile. Since the production term in the turbulence kinetic energy equation is a function of velocity gradient, the decrease in the velocity gradient reduces the production term and therefore, reduces the turbulence kinetic energy and the heat transfer coefficient. In the case of a high mass flow-rate, the buoyancy effect is small and can be ignored. However, when the wall temperature is larger than the pseudo-critical temperature, a large temperature gradient is established near the wall. The large density difference between the near-wall and the bulk flow accelerates the near-wall

fluid. Like the HTD in low mass flow rates, the flattened velocity profile acts to cause the HTD in high mass flow rates. Heat transfer deterioration is an undesirable phenomenon that designs of a SCWR will aim to avoid.

### 5.3 Comparison with Experimental Heat Transfer Data

#### 5.3.1 Identification of Experiments: Shitsman and Ornatsky

Table 5.1 summarizes flow conditions and geometry specifications for the Shitsman and Ornatsky test cases.

Table 5.1: Flow conditions for experiments of Shitsman and Ornatsky

Test Case	Author	System Pressure (MPa)	Inlet Temperature (K)	Mass Flux (kg/m <sup>2</sup> s)	Heat Flux (kW/m <sup>2</sup> )	Diameter (mm)	Length (m)
T1	Shitsman	23.3	598.05	430	319.87	8	1.50
T2	Ornatsky	25.5	368.91	1500	1810	3	1.05

#### 5.3.2 Grid-Independence Study: The Shitsman Test Case

Ten grids with different numbers of nodes in different sections were created to examine the number of axial nodes, radial nodes, angular nodes, and  $y^+$  and to determine a grid with acceptable numerical accuracy. The grids used to study the mesh independency of Shitsman's geometry are given in Table. 5.2.

Table 5.2: Grids used for mesh-independence check for case T1

Grid	Number of Nodes			First Near-Wall Spacing (mm)	Maximum $y^+$
	Axial	Radial	Angular		
1-S	250	100	7	$1 \times 10^{-3}$	0.36
2-S	430	100	7	$1 \times 10^{-3}$	0.36
3-S	600	100	7	$1 \times 10^{-3}$	0.36
4-S	430	50	7	$1 \times 10^{-3}$	0.36
5-S	430	150	7	$1 \times 10^{-3}$	0.36
6-S	430	100	3	$1 \times 10^{-3}$	0.36
7-S	430	100	11	$1 \times 10^{-3}$	0.36
8-S	430	100	15	$1 \times 10^{-3}$	0.36
9-S	430	100	7	$3 \times 10^{-4}$	0.108
10-S	430	100	7	$1 \times 10^{-4}$	0.036

The axial distribution of average angular wall temperature was used to assess grid independence. The value of wall temperature at each axial location was determined using a length average long a line in the angular direction along the wall. Table 5.3 shows the maximum percentage difference and the RMS difference of axial variation of average angular wall temperature between different grids.

Table 5.3: RMS and maximum percentage deviation of axial variation of average angular wall temperature between grids for case T1

Parameter Studied	Grids Compared	RMS Difference (K)	Max. Diff (%)
Number of axial nodes	1-S and 2-S	5.72	3.34
	2-S and 3-S	0.57	0.34
Number of radial nodes	4-S and 2-S	15.58	10.18
	2-S and 5-S	1.63	0.92
Maximum $y^+$	2-S and 9-S	12.96	6.97
	9-S and 10-S	9.4	5.3

From the results shown in Table 5.3, 430 nodes in the axial direction and 100 nodes in the radial direction were considered adequate. As Table 5.3 suggests, the results of wall temperature are very sensitive to the  $y^+$  of the grid. This is due to the strong variation of near-wall thermo-physical properties at supercritical pressures. The maximum percentage difference between grids 9-S and 10-S is about 5.3%. However, when  $y^+$  is quite low, convergence problems are encountered, so the variation of wall temperature are examined in detail and  $y^+$  was changed. Figure 5.1 shows the variation of average angular wall temperature along the tube using different maximum  $y^+$  values. As the value of  $y^+$  decreases and the mesh becomes more refined near the wall, the peaks in the wall temperature shift toward the outlet in the  $x$  direction and the value of wall temperature at the second peak reduces. However, between grids 9-S and 10-S the wall temperature does not change considerably and the results of the medium grid are considered acceptable.

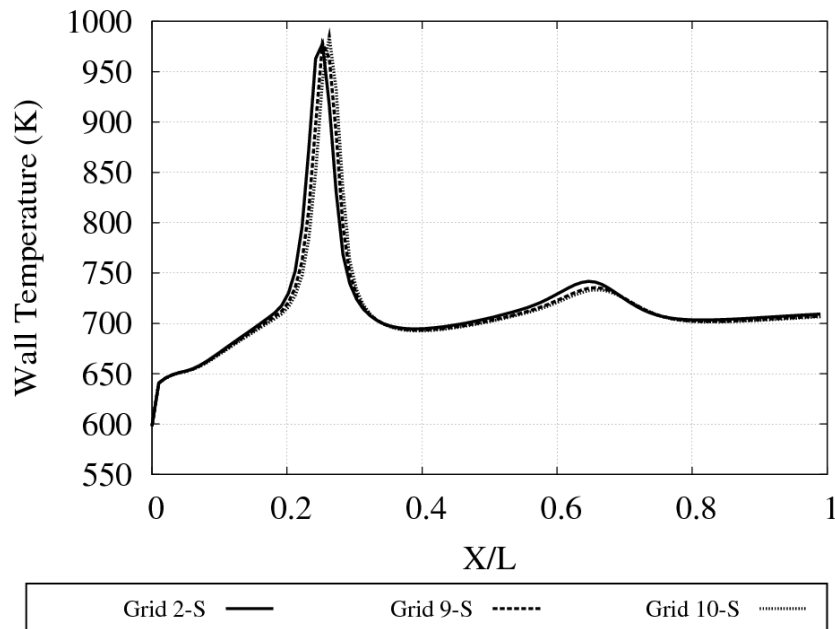


Figure 5.1: Effect of near-wall spacing on average angular wall temperature along the pipe for case T1

To study the effect of number of angular nodes, the maximum difference of wall temperature in the angular direction at each axial location along the pipe is compared between grids and is shown in Figure 5.2. This figure suggests that Grid 2-S with 7 nodes in the angular direction produces a more uniform angular temperature distribution compared to 3, 11, and 15 numbers of nodes. However, grids 2-S, 7-S, and 8-S all have acceptably small variation in wall temperature in the angular direction.

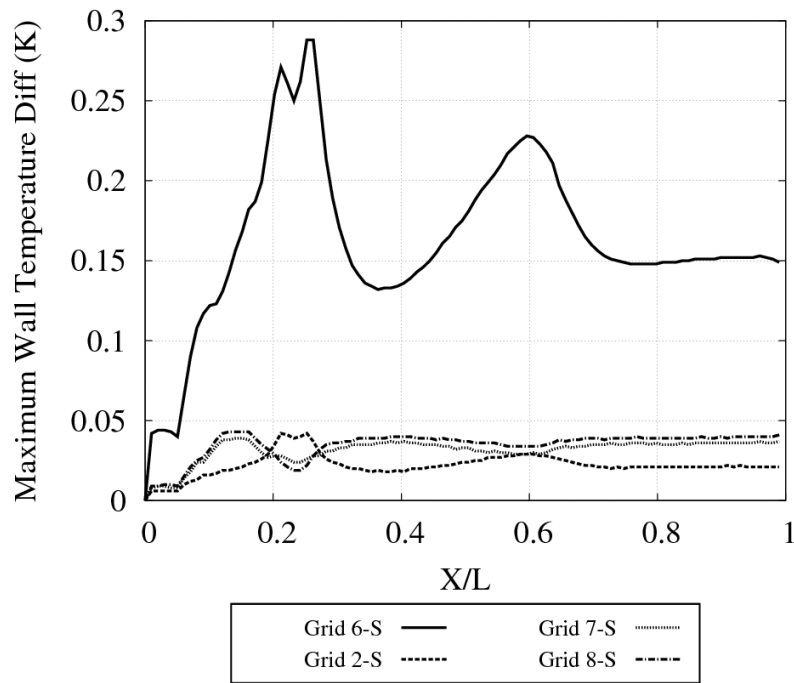


Figure 5.2: Maximum difference in angular wall temperature at each axial location along the pipe for case T1

The mesh-independence tests were also conducted using coarse, medium, and fine meshes of 89,750, 304,870, and 635,400 nodes, respectively. It is noteworthy that the number of nodes includes those in the diamond-shape region of the grid as well (Figure 4.1). Table 5.4 shows the number of nodes in different sections of the grids.

Table 5.4: Grids used to study the effect of changing the number of radial and axial nodes simultaneously for case T1

Grid	Number of Nodes			First Near-Wall Spacing (mm)
	Axial	Radial	Angular	
<b>Coarse-S</b>	250	50	7	$3 \times 10^{-4}$
<b>Medium-S</b>	430	100	7	$3 \times 10^{-4}$
<b>Fine-S</b>	600	150	7	$3 \times 10^{-4}$

The mesh independence of the results for the three grids in Table 5.4 was assessed in two ways. First, the axial variation of average angular wall temperature was determined and compared between grids. In addition, the static pressure drop along the tube length was compared. Table 5.5 shows the maximum percentage difference and the RMS difference of average angular wall temperature and static pressure drop between coarse, medium and fine grids. The percentage and RMS error of average angular wall temperature between the medium and fine grids are small. However, the maximum percentage difference of static pressure drop between the medium grid and the fine grid is relatively large. This difference is near the outlet of the channel where the static pressure reaches zero and therefore, the maximum percentage difference is not a good criterion to compare the grids. The RMS difference between both coarse and medium, and medium and fine grids is low (the maximum static pressure of domain is about 2000 Pa). Therefore, for static pressure, even the coarse grid is accurate enough. However, based on the percentage and RMS error of average angular wall temperature differences between grids, the medium grid was selected.

Table 5.5: RMS and maximum percentage deviation of axial variation of average angular wall temperature and static pressure drop between coarse, medium and fine grids for case T1

Grids Compared	Wall Temperature		Static Pressure Drop	
	RMS Difference (K)	Max. Difference (%)	RMS Difference (Pa)	Max. Difference (%)
Coarse-S and Medium-S	34.11	25.2	1.45	17.03
Medium-S and Fine-S	0.52	0.52	2.26	14.46

Figure 5.3 shows the variation of average angular wall temperature along the pipe for coarse, medium and fine grids. This figure clearly shows that the coarse mesh underestimates the value of wall temperature. In this figure, the curves of wall temperature variation for Medium-S and Fine-S grids are coincident.

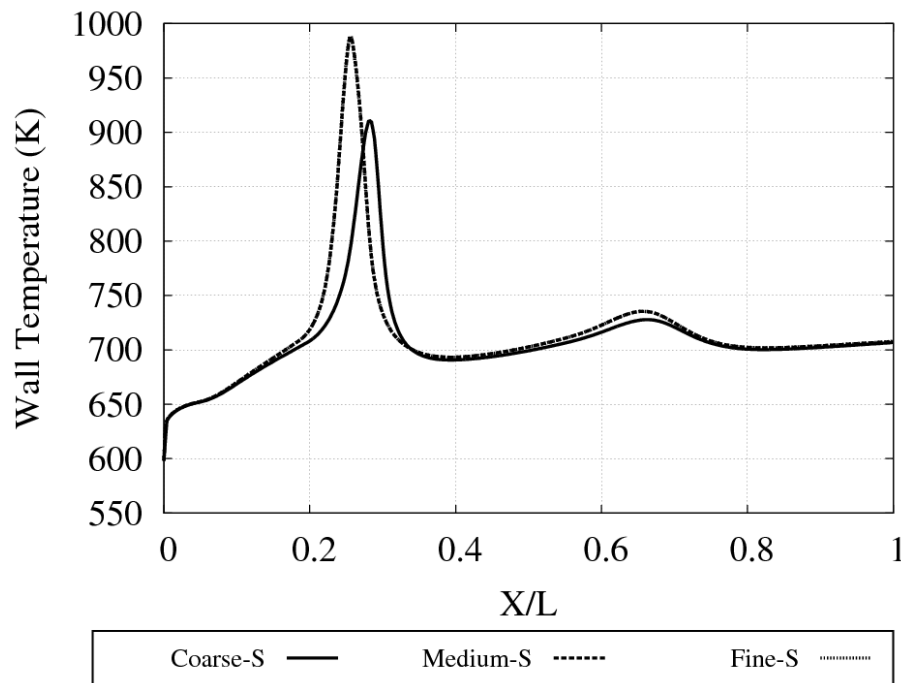


Figure 5.3: Comparison of average angular wall temperature between three grids shown in Table 5.5 for case T1

Two radial lines at the middle and at the outlet of pipe were defined to assess the dependence of the solution on grid refinements in the radial direction. Table 5.6 shows the maximum percentage difference and the RMS difference of velocity between coarse, medium and fine grids. The percentage and RMS error between the medium and fine grids are very small and the medium grid predicts the radial velocity accurately.

Table 5.6: RMS and maximum percentage deviation of radial velocity between coarse, medium and fine grids for case T1

<b>Grids compared</b>	<b>Outlet Radial Velocity</b>		<b>Radial Velocity at <math>\frac{x}{L} = \frac{1}{2}</math></b>	
	<b>RMS Difference (K)</b>	<b>Max. Difference (%)</b>	<b>RMS Difference (Pa)</b>	<b>Max. Difference (%)</b>
<b>Coarse-S and Medium-S</b>	0.0062	0.88	0.0018	1.99
<b>Medium-S and Fine-S</b>	0.00088	0.11	0.00037	0.098

Figures 5.4 and 5.5 show the variation of radial velocity at the middle and at the outlet of the pipe, respectively, for coarse, medium and fine grids. In these figures, the curves of velocity variation for Medium-S and Fine-S grids are coincident.

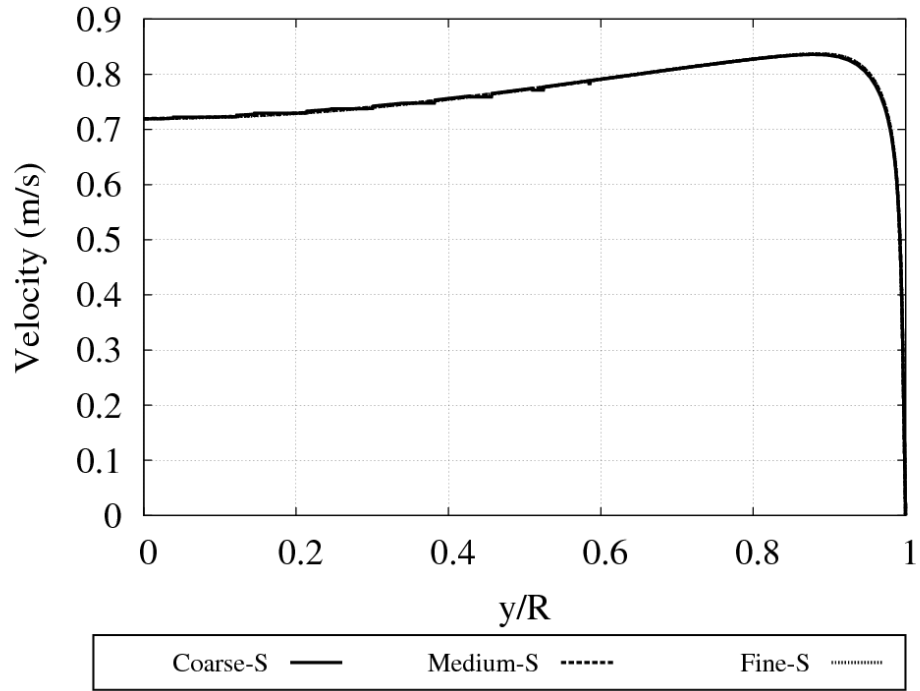


Figure 5.4: Comparison of radial variation of velocity at  $\frac{x}{L} = \frac{1}{2}$  between three grids for case T1

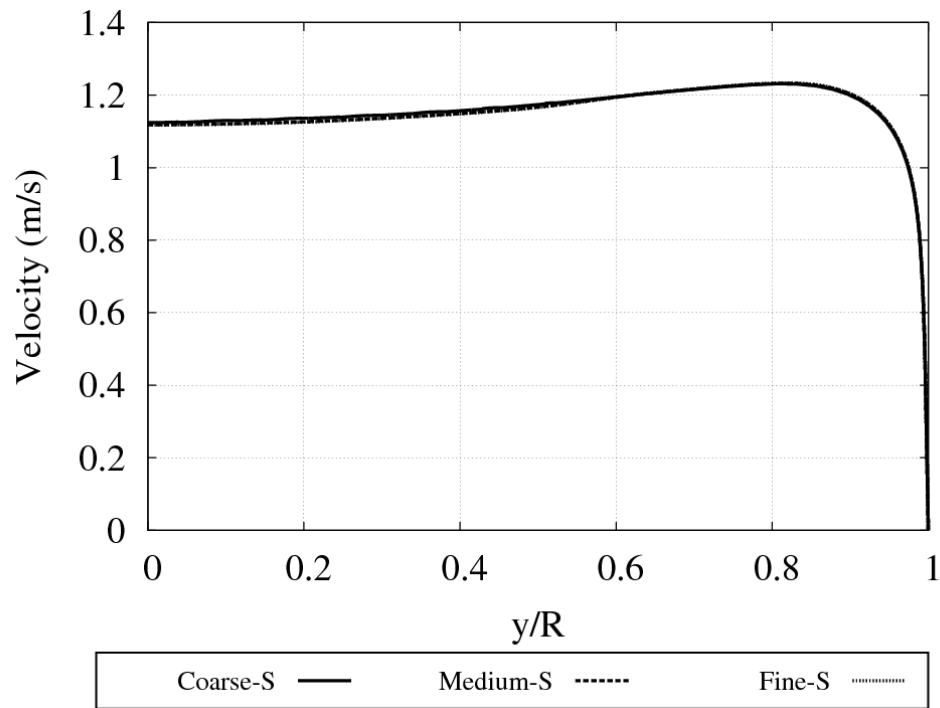


Figure 5.5: Comparison of radial variation of outlet velocity between three grids for case T1

Table 5.7 presents the maximum percentage difference and the RMS difference of temperature between coarse, medium and fine grids along the radial lines at the middle and at the outlet of the pipe. The percentage and RMS error between the medium and fine grids are small enough to consider the medium grid acceptable.

Table 5.7: RMS and maximum percentage deviation of radial temperature between coarse, medium and fine grids for case T1

Grids compared	Outlet Radial Temperature		Radial Temperature at $\frac{x}{L} = \frac{1}{2}$	
	RMS Difference (K)	Max. Difference (%)	RMS Difference (Pa)	Max. Difference (%)
Coarse-S and Medium-S	0.24	0.5	0.068	0.13
Medium-S and Fine-S	0.017	0.0059	0.01	0.015

Figures 5.6 and 5.7 show the variation of radial temperature at the middle and at the outlet of the pipe for coarse, medium and fine grids. In this figure, the curves of temperature variation for Coarse-S, Medium-S and Fine-S grids are coincident.

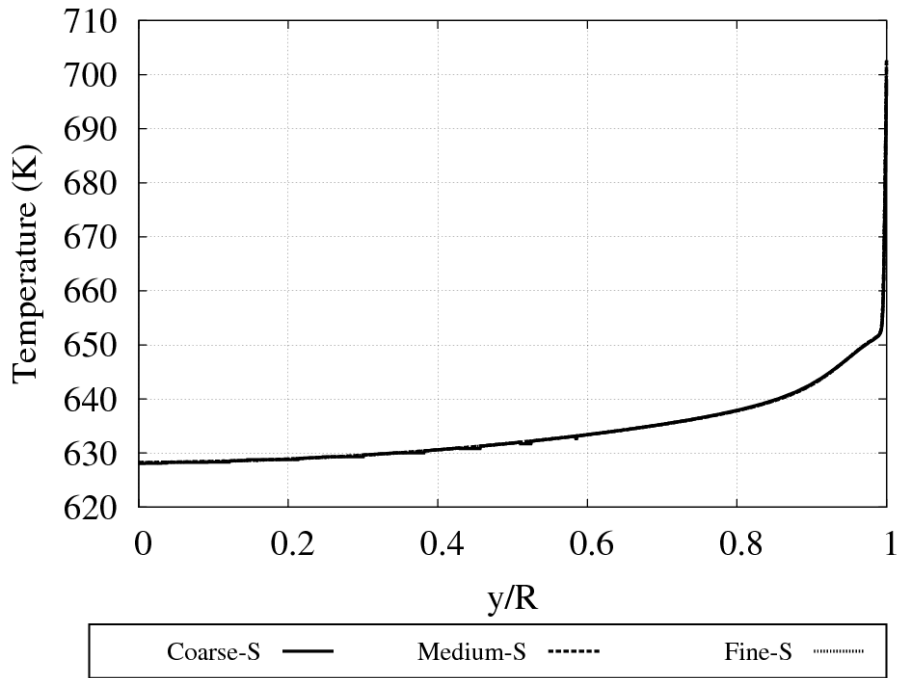


Figure 5.6: Comparison of radial variation of temperature at  $\frac{x}{L} = \frac{1}{2}$  between three grids for case T1

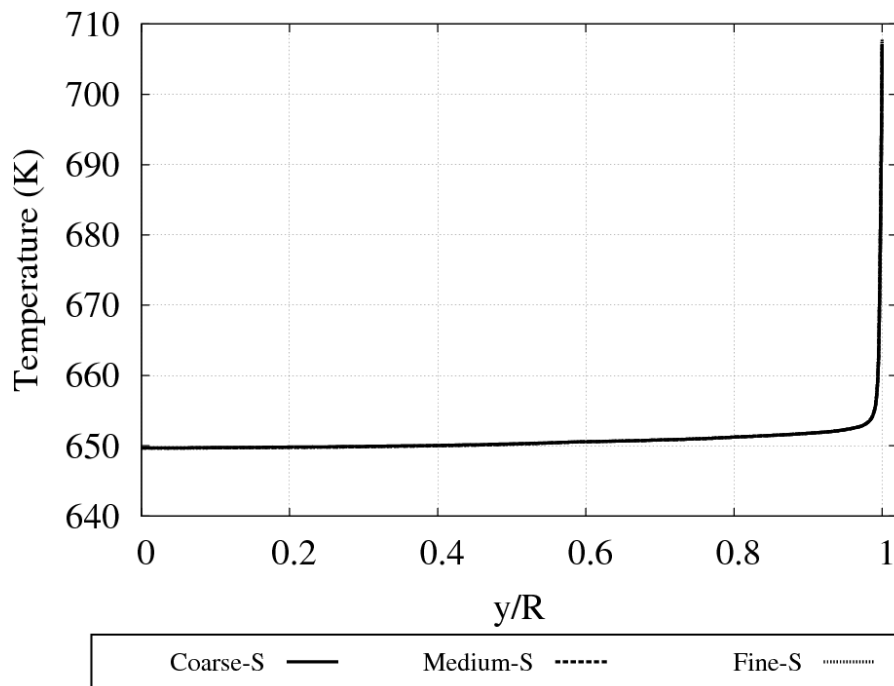


Figure 5.7: Comparison of radial variation of outlet temperature between three grids for case T1

Table 5.8 presents the maximum percentage difference and the RMS difference of static pressure between coarse, medium and fine grids along a radial line at the middle of the pipe. This table suggests that the value of static pressure is not very sensitive to the grid refinement and even the coarse grid is accurate enough.

Table 5.8: RMS and maximum percentage deviation of radial pressure between coarse, medium and fine grids for case T1

<b>Grids Compared</b>	<b>Radial Static Pressure Difference at <math>\frac{x}{L} = \frac{1}{2}</math></b>	
	<b>RMS Difference (Pa)</b>	<b>Max. Difference (%)</b>
<b>Coarse-S and Medium-S</b>	2.89	0.17
<b>Medium-S and Fine-S</b>	3.65	0.28

### 5.3.3 Grid-Independence Study: The Ornatsky Test Case

Ten grids with different numbers of nodes in different sections were created to examine the effect of changing the number of axial nodes, radial nodes, angular nodes, and near-wall spacing on the solution produced by the code. The grids used to study the mesh independency of Ornatsky's geometry are listed in Table. 5.9.

Table 5.9: Grids used for mesh-independence check for case T2

Grid	Number of Nodes			First Near-Wall Spacing (mm)	Maximum $y^+$
	Axial	Radial	Angular		
<b>1-O</b>	200	100	7	$5 \times 10^{-4}$	0.56
<b>2-O</b>	400	100	7	$5 \times 10^{-4}$	0.56
<b>3-O</b>	600	100	7	$5 \times 10^{-4}$	0.56
<b>4-O</b>	400	50	7	$5 \times 10^{-4}$	0.56
<b>5-O</b>	400	150	7	$5 \times 10^{-4}$	0.56
<b>6-O</b>	400	100	3	$5 \times 10^{-4}$	0.56
<b>7-O</b>	400	100	11	$5 \times 10^{-4}$	0.56
<b>8-O</b>	400	100	15	$5 \times 10^{-4}$	0.56
<b>9-O</b>	400	100	7	$1 \times 10^{-4}$	0.11
<b>10-O</b>	400	100	7	$5 \times 10^{-5}$	0.056

The axial distribution of average angular wall temperature was used to assess grid independence. Table 5.10 shows the maximum percentage difference and the RMS difference of axial variation of average angular wall temperature between different grids.

Table 5.10: RMS and maximum percentage deviation of axial variation of average angular wall temperature between grids for case T2

Parameter studied	Grids compared	RMS difference (K)	Max. Difference (%)
<b>Number of axial nodes</b>	1-O and 2-O	0.38	0.36
	2-O and 3-O	0.16	0.13
<b>Number of radial nodes</b>	4-O and 2-O	5.24	1.144
	2-O and 5-O	0.18	0.13
<b>Maximum <math>y^+</math></b>	2-O and 9-O	4.95	1.177
	9-O and 10-O	0.55	0.13

From the results shown in Table 5.10, 400 nodes in axial direction and 100 nodes in radial direction were considered adequate. Also a  $y^+$  of 0.11 has a maximum percentage difference of 0.13% from a  $y^+$  of 0.056. Therefore,  $y^+$  of 0.11 was considered adequate.

Figure 5.8 shows the variation of average angular wall temperature along the pipe using different near-wall spacings. In this figure, the curves of wall temperature variation for 9-O and 10-O grids are coincident.

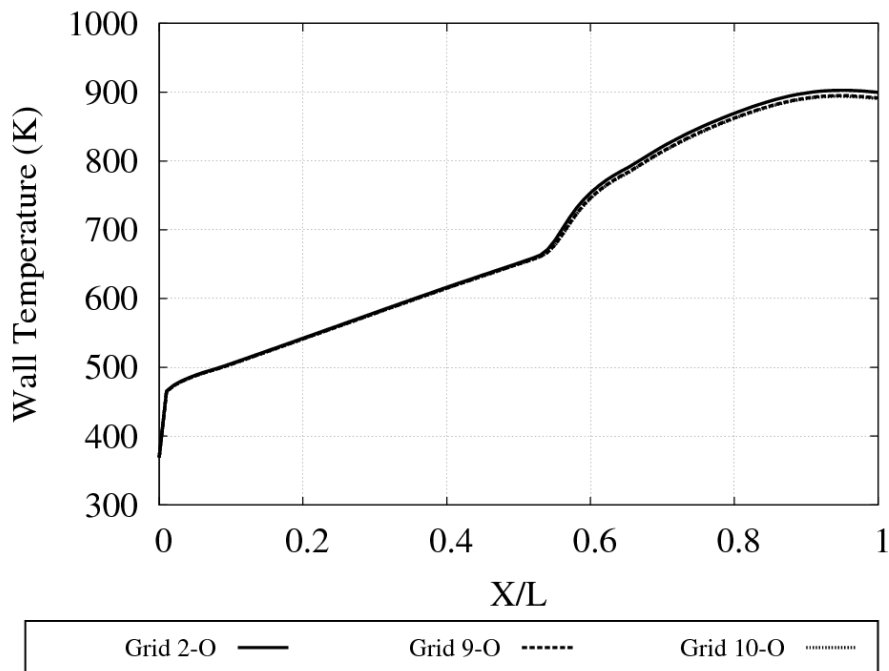


Figure 5.8: Effect of near-wall spacing on average angular wall temperature along the pipe for case T2

To study the effect of number of angular nodes, the maximum difference in wall temperature in the angular direction at each axial location along the pipe is compared between grids. Figure 5.9 shows the effect of number of angular nodes on the maximum difference in angular wall temperature at each axial location along the pipe. Figure 5.9

suggests that Grid 2-O with 7 nodes in the angular direction produces a more uniform angular temperature distribution compared to 3, 11, and 15 numbers of nodes.

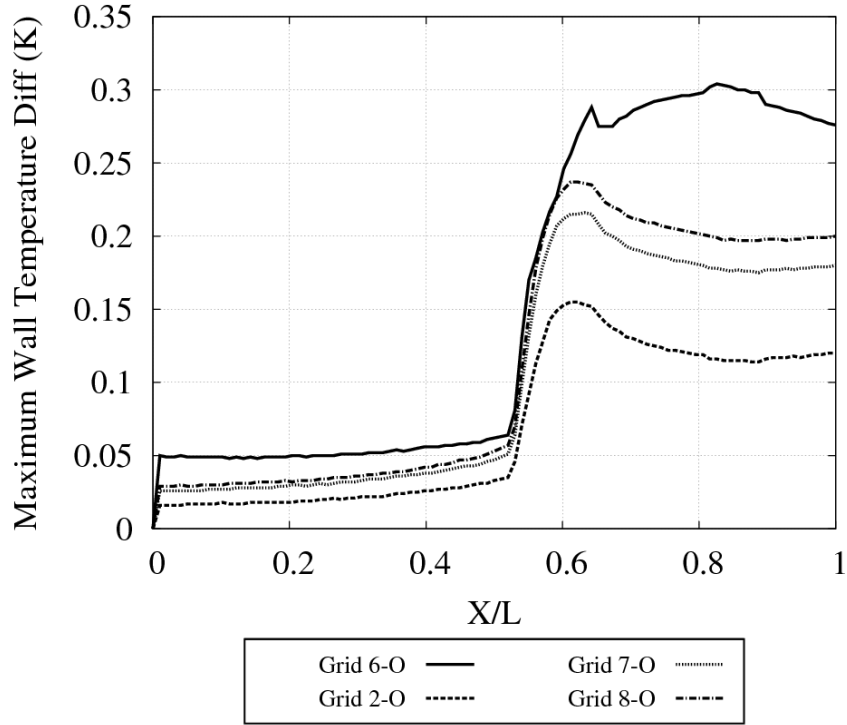


Figure 5.9: Maximum difference in angular wall temperature at each axial location along the pipe for case T2

The mesh-independence tests were also conducted using coarse, medium, and fine meshes of 71800, 283,600, and 635,400 nodes, respectively. Table 5.11 shows the number of nodes in different sections of the grids.

Table 5.11: Grids used to study the effect of changing the number of radial and axial nodes simultaneously for case T2

Grid	Number of Nodes			First Near-Wall Spacing (mm)
	Axial	Radial	Angular	
<b>Coarse-O</b>	200	50	7	$1 \times 10^{-4}$
<b>Medium-O</b>	400	100	7	$1 \times 10^{-4}$
<b>Fine-O</b>	600	150	7	$1 \times 10^{-4}$

The axial variation of average angular wall temperature was determined and compared between grids. In addition, the static pressure drop along the tube length was compared. Table 5.12 shows the maximum percentage difference and the RMS difference of average angular wall temperature and static pressure drop between coarse, medium and fine grids. Since the percentage and RMS error between the medium and fine grids were small, the medium grid was considered suitable.

Table 5.12: RMS and maximum percentage deviation of axial variation of average angular wall temperature between coarse, medium and fine grids for case T2

<b>Grids Compared</b>	<b>Wall Temperature</b>		<b>Static Pressure Drop</b>	
	<b>RMS Difference (K)</b>	<b>Max. Difference (%)</b>	<b>RMS Difference (Pa)</b>	<b>Max. Difference (%)</b>
<b>Coarse-O and Medium-O</b>	6.19	1.39	45.19	0.78
<b>Medium-O and Fine-O</b>	0.28	0.18	2.91	0.55

Figure 5.10 shows the variation of average angular wall temperature along the pipe for coarse, medium and fine grids. As in case T1, the coarse mesh underestimates the value of average angular wall temperature for this case. In this case, however, the underestimation is relatively small. In this figure, the curves of wall temperature variation for Medium-O and Fine-O grids are coincident.

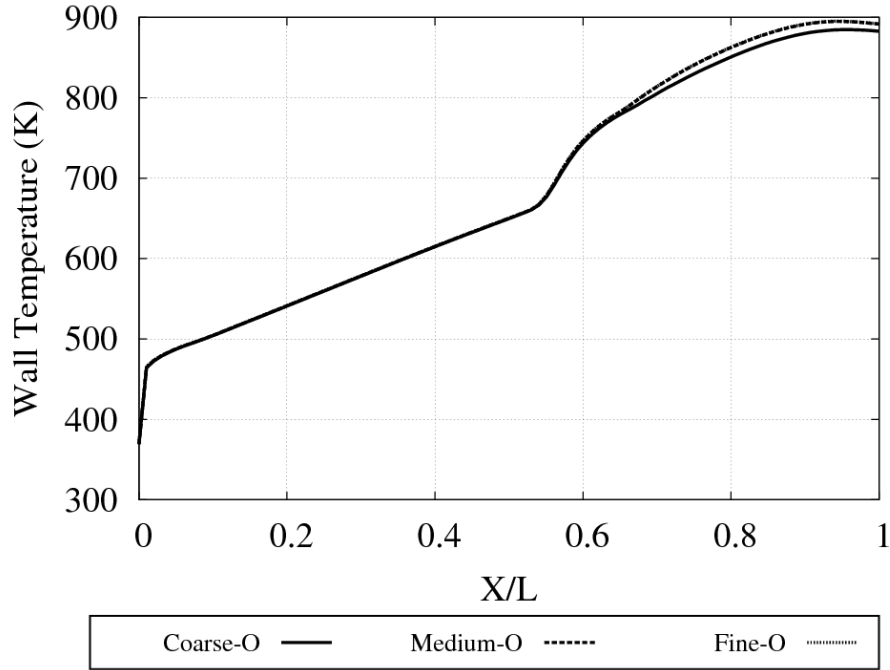


Figure 5.10: Comparison of average angular wall temperature between three grids shown in Table 5.12 for case T2

Two radial lines at the middle and at the outlet of the pipe were defined to study the mesh independency in the radial direction. Table 5.13 shows the maximum percentage difference and the RMS difference of velocity between coarse, medium and fine grids. This table suggests that the medium grid produces acceptable results.

Table 5.13: RMS and maximum percentage deviation of radial velocity between coarse, medium and fine grids for case T2

Grids Compared	Outlet Radial Velocity		Radial Velocity at $\frac{x}{L} = \frac{1}{2}$	
	RMS Difference (K)	Max. Difference (%)	RMS Difference (Pa)	Max. Difference (%)
Coarse-O and Medium-O	0.0086	2.54	0.0035	0.75
Medium-O and Fine-O	0.0029	0.08	0.0056	0.067

Figures 5.11 and 5.12 show the variation of radial velocity at the middle and at the outlet of the pipe, respectively, for coarse, medium and fine grids.

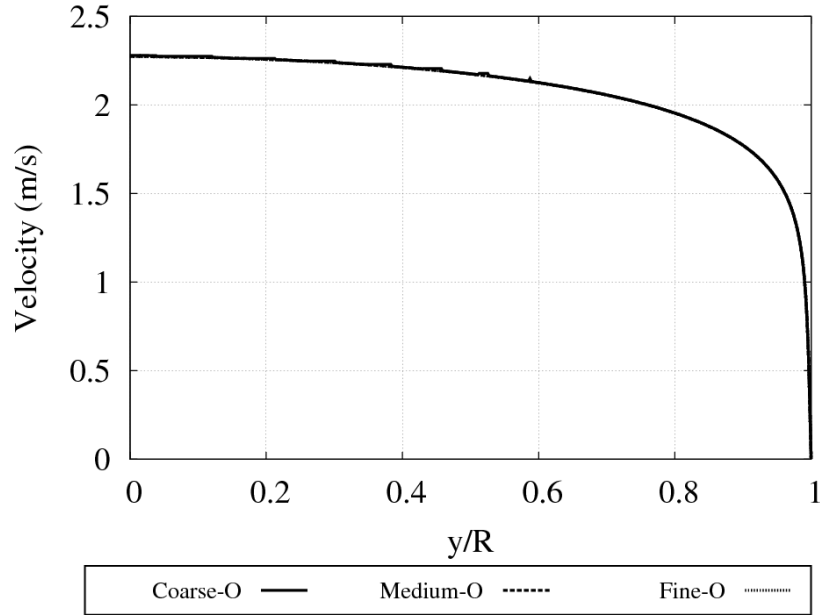


Figure 5.11: Comparison of radial variation of velocity at  $\frac{x}{L} = \frac{1}{2}$  between three grids for case T2

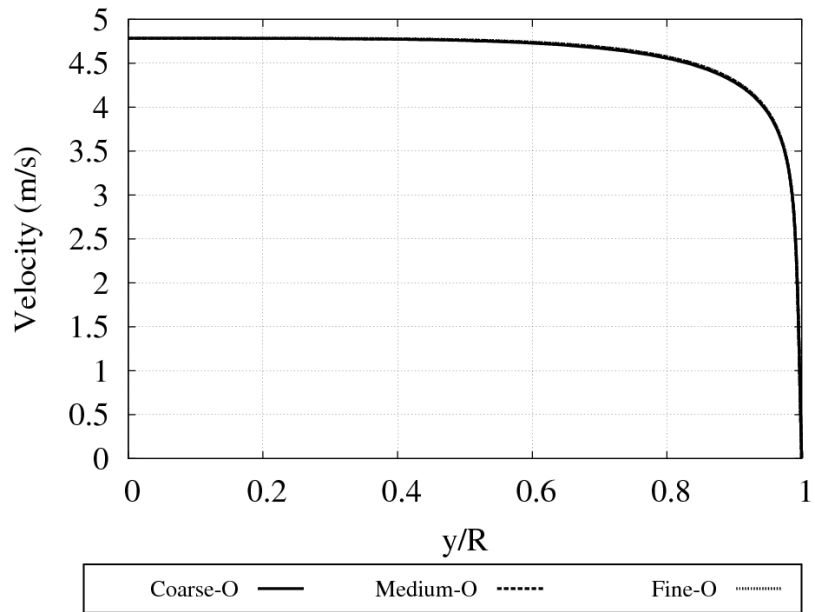


Figure 5.12: Comparison of radial variation of outlet velocity between three grids for case T2

Table 5.14 shows the maximum percentage difference and the RMS difference of temperature between coarse, medium and fine grids along the radial lines at the middle and at the pipe outlet. Based on these results, the medium grid gives a suitable prediction of radial temperature.

Table 5.14: RMS and maximum percentage deviation of radial temperature between coarse, medium and fine grids for case T2

<b>Grids Compared</b>	<b>Outlet Radial Temperature</b>		<b>Radial Temperature at <math>\frac{x}{L} = \frac{1}{2}</math></b>	
	<b>RMS Difference (K)</b>	<b>Max. Difference (%)</b>	<b>RMS Difference (Pa)</b>	<b>Max. Difference (%)</b>
<b>Coarse-O and Medium-O</b>	0.84	1.14	0.19	0.17
<b>Medium-O and Fine-O</b>	0.034	0.03	0.06	0.02

Figures 5.13 and 5.14 show the variation of radial temperature at the middle and at the pipe outlet, respectively, for coarse, medium and fine grids.

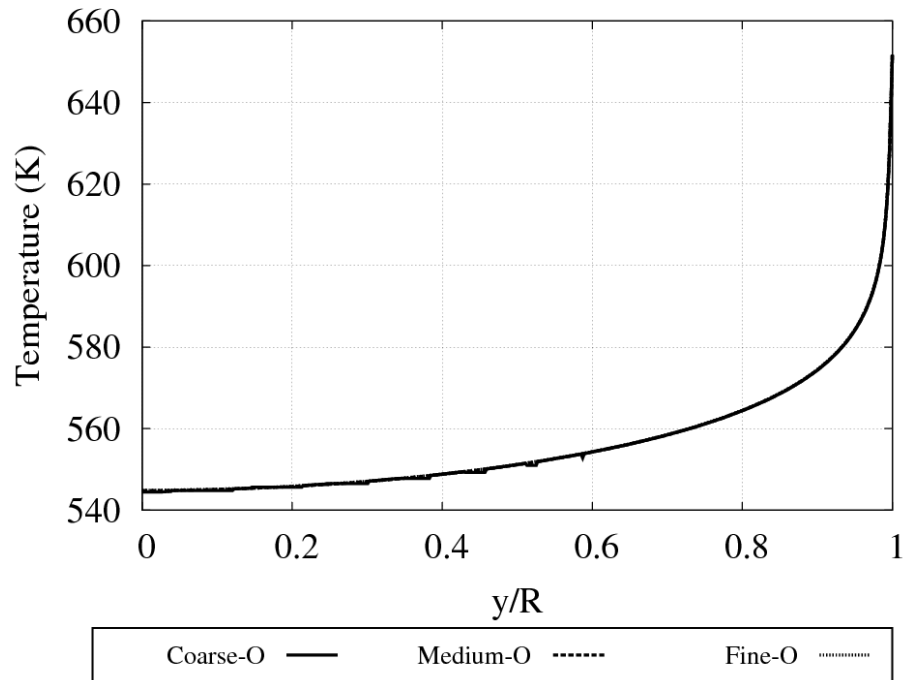


Figure 5.13: Comparison of radial variation of temperature at  $\frac{x}{L} = \frac{1}{2}$  between three grids for case T2

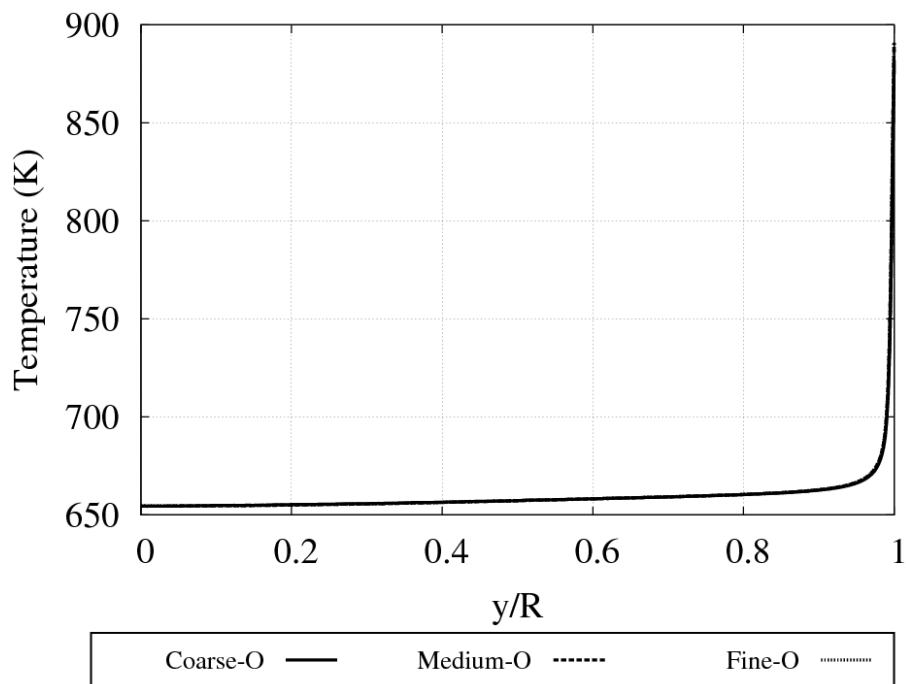


Figure 5.14: Comparison of radial variation of outlet temperature between three grids for case T2

Table 5.15 shows the maximum percentage difference and the RMS difference of static pressure between coarse, medium and fine grids along a radial line at the middle of the pipe. The radial static pressure for the medium grid has a small error compared to the fine grid. Therefore, the medium grid was considered suitable.

Table 5.15: RMS and maximum percentage deviation of radial pressure between coarse, medium and fine grids for case T2

Grids Compared	Radial Static Pressure Difference at $\frac{x}{L} = \frac{1}{2}$	
	RMS Difference (Pa)	Max. Difference (%)
Coarse-O and Medium-O	46.18	0.52
Medium-O and Fine-O	1.19	0.06

### 5.3.4 Effect of Varying the Turbulent Prandtl Number

#### Background

Turbulent Prandtl number ( $Pr_t$ ) is defined as the ratio between the momentum eddy diffusivity and the thermal eddy diffusivity and is a property of turbulent flow. According to Weigand et al. (1996):

$$Pr_t \leq 1 \quad \text{for} \quad Pr \geq 1 \quad (\text{gases and liquids})$$

$$Pr_t > 1 \quad \text{for} \quad Pr < 1 \quad (\text{liquid metals})$$

$Pr_t$  has a great effect on the heat transfer characteristics of the flow (Howell and Lee, 1999). However, the effect of  $Pr_t$  for deteriorated heat transfer condition and for a fluid with variable properties has not been studied extensively. Bazargan and Mohseni (2007)

used supercritical carbon dioxide and developed a two-dimensional model using the SIMPLE algorithm. They implemented six models for  $Pr_t$  and investigated the effect of constant and variable values of  $Pr_t$  on heat transfer for both normal and deteriorated modes of heat transfer. They compared the results with the experimental data of Song et al. (2008) which was obtained for supercritical flow in a vertical pipe. The models Bazargan and Mohseni (2007) used are as follows:

Equation (5.1) developed by Myoung et al. (1989):

$$Pr_t = 0.75 + \frac{1.63}{\ln\left(1 + \frac{Pr}{0.0015}\right)} \quad (5.1)$$

Equation (5.2) developed by Hollingsworth et al. (1989) for water at normal pressure:

$$Pr_t = 1.855 - \tanh[0.2(y^+ - 7.5)] \quad (5.2)$$

Where

$$y^+ = \frac{\rho \sqrt{\frac{\tau_w}{\rho y}}}{\mu} = \frac{\rho u_\tau}{\sqrt{y} \mu} \quad (5.3)$$

Equation (5.4) developed by Kays (1994):

$$Pr_t = \frac{2.0}{Pe_t} + 0.85 \quad (5.4)$$

Where

$$Pe_t = \frac{\mu_t}{\mu} Pr \quad (5.5)$$

Equation (5.6) developed by Kays and Crawford (2005), useful for all values of  $Pr$ :

$$Pr_t = \left\{ \frac{1}{7} + 0.3 \frac{Pe_t}{\sqrt{0.85}} - (0.3 Pe_t)^2 \left[ 1 - \exp\left(-\frac{1}{\sqrt{0.85}(0.3Pe_t)}\right) \right] \right\}^{-1} \quad (5.6)$$

Constant turbulent Prandtl numbers of 0.85, 0.9 and 1 were also used by Bazargan and Mohseni (2007) to study the effect of constant values of  $Pr_t$  on heat transfer.

They concluded that the model of Kays (1994), Kays and Crawford (2005), and Myoung et al (1989), along with the constant  $Pr_t$  of 0.9 are more capable of predicting heat transfer characteristics in normal mode of heat transfer. Also, the  $Pr_t$  of Kays (1994) results in considerable deviation in deteriorated mode of heat transfer.

In addition,  $Pr_t$  may be different near the wall and away from the wall. According to Weigand et al. (1996), the value of  $Pr_t$  is influenced by the wall distance which tends to increase the  $Pr_t$  close to the wall. Outside the thermal boundary layer the value of  $Pr_t$  seems to be constant for  $Pr > 1$ .

Due to lack of experimental and DNS data especially for the deteriorated mode of heat transfer in supercritical flow, constant  $Pr_t$  numbers similar to the constant property fluid have been used in this study. For cases T1 and T2, different values of constant  $Pr_t$  were employed in the simulations and the results are compared to experimental data to find the best value of  $Pr_t$ .

- Case T1

Figures 5.15 and 5.16 show the variation of wall temperature along the pipe for  $Pr_t$  numbers of 0.9 and 1 compared to experimental data of Shitsman and the numerical results of Jaromin and Anglart (2013). The results of Jaromin and Anglart were obtained

using ANSYS CFX. As shown in Figures 5.15 and 5.16, there is a noticeable difference between the results of the present study and the results of Jaromin and Anglart. The main reason for this disagreement is the difference in the  $y^+$  between the two studies. As discussed earlier,  $y^+$  has a considerable effect on the wall temperature and as the value of  $y^+$  decreases, the peaks in the wall temperature shift toward the outlet in the  $x$  direction and the value of wall temperature at the second peak reduces. In the study of Jaromin and Anglart, the value of  $y^+$  was between 0.3 and 0.5, while in this study, the value of  $y^+$  was 0.1. Another source of disagreement might be the maximum number of points in the water property tables. When defining the density or specific heat capacity using IAPWS, the CFX-Solver generates tables of properties. These tables include the range of temperature and pressure and the maximum points. The parameter of maximum points specifies the maximum number of points (values) for each table dimension. The default value of 100 is not always adequate. In this study, the value was increased to 1000 points to increase the accuracy. For more than 1000 points, the results did not change significantly. In the study of Jaromin and Anglart the maximum number of points was not mentioned. For  $Pr_t$  equal to 0.9, the results of Jaromin and Anglart shows better agreement with experimental results, while for  $Pr_t$  equal to 1, the results of current study show better agreement with experimental data, compared to the results of Jaromin and Anglart.

Figure 5.17 shows the variation of wall temperature along the pipe for different  $Pr_t$  numbers compared to the experimental data. As  $Pr_t$  increases, the wall temperature peaks shift toward the channel inlet and the wall temperature value associated with the second peak increases. All models are able to predict the trend of axial temperature. However,

for some  $Pr_t$  numbers, the magnitude of temperature at the second peak is not predicted accurately enough and for others, the location of the second peak is not predicted correctly. Also, the magnitudes of the temperature at the first peak and after the peak are over-predicted for all of the values of  $Pr_t$  used. The numerical code also fails to predict the reduction in the wall temperature near the flow outlet. Table 5.16 shows the RMS deviation of wall temperature from Shitsman's experiment for different  $Pr_t$  numbers.  $Pr_t$  number equal to 1.05 has the smallest RMS difference with the experimental data because this  $Pr_t$  best predicts the location of the first peak in the wall temperature, although it under-predicts the location of the second peak. However,  $Pr_t$  equal to 1 seems to give a better overall agreement of wall temperature along the pipe. Therefore,  $Pr_t$  of 1 was considered best for Shitsman's case.

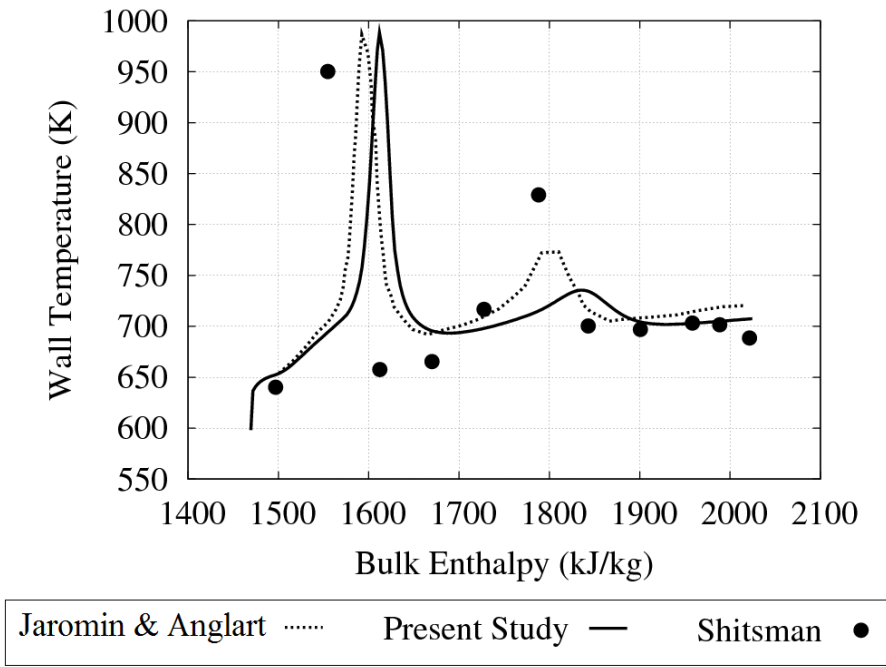
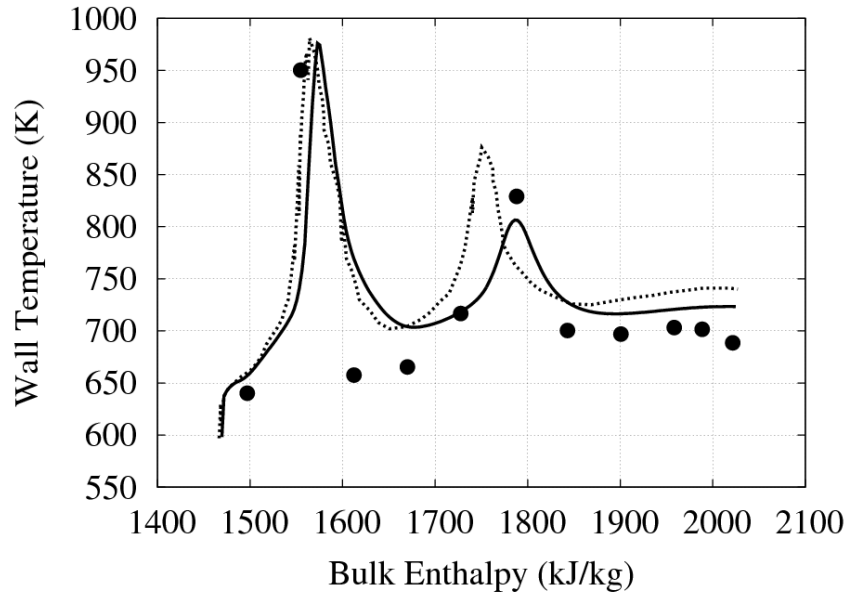
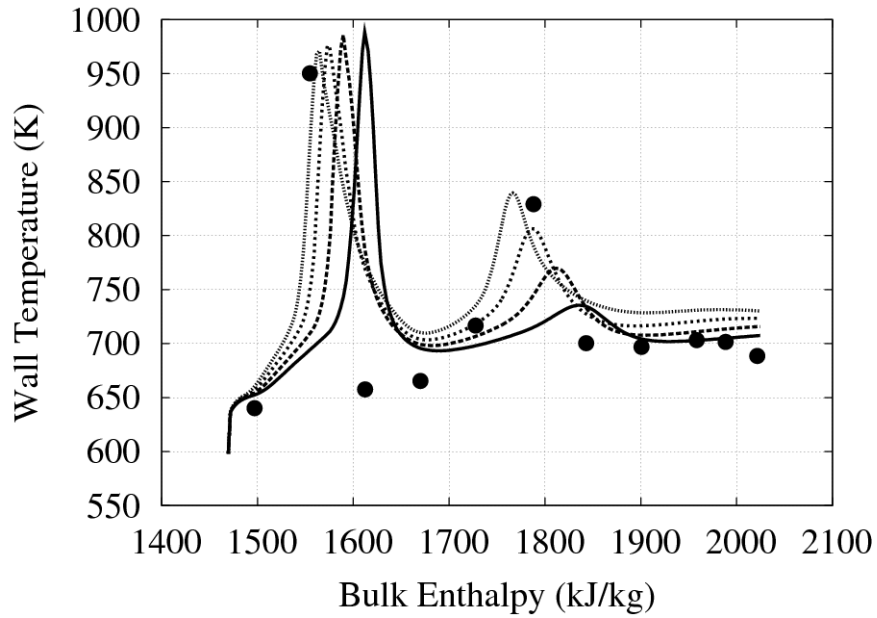


Figure 5.15: Comparison of wall temperature with Shitsman's experiment and Jaromin and Anglart's numerical work-  $Pr_t=0.9$  for case T1



Jaromin & Anglart ..... Present Study — Shitsman ●

Figure 5.16: Comparison of wall temperature with Shitsman's experiment and Jaromin and Anglart's numerical work-  $Pr_t=1$  for case T1



$Pr_t = 0.9$  —  $Pr_t = 1$  ..... Shitsman ●  
 $Pr_t = 0.95$  - · -  $Pr_t = 1.05$  - - -

Figure 5.17: Comparison of wall temperature with Shitsman's experiment for different  $Pr_t$  numbers for case T1

Table 5.16: RMS deviation of wall temperature from Shitsman’s experiment for different  $Pr_t$  numbers for case T1

<b>Turbulent Prandtl Number</b>	<b>RMS Difference (K)</b>
<b>0.9</b>	131.93
<b>0.95</b>	88.53
<b>1</b>	74.90
<b>1.05</b>	53.07

- Case T2

Figures 5.18 and 5.19 show the variation of wall temperature along the pipe for  $Pr_t$  numbers of 0.9 and 1 compared to experimental data and the numerical results of Jaromin and Anglart (2013). Here, the difference between the results of the present study and the results of Jaromin and Anglart is not noticeable like the Shitsman’s experiment and the reason is that the results of wall temperature for Ornatsky’s experiment are less sensitive to the value of  $y^+$  (Figure 5.8).

Figure 5.20 shows the variation of wall temperature along the pipe for different  $Pr_t$  numbers compared to the experimental data. All models are able to predict the trend of the axial temperature. The onset of the heat transfer deterioration is predicted accurately using all values of  $Pr_t$ . However, in the region of heat transfer deterioration, the results obtained using different values of  $Pr_t$  deviate and as  $Pr_t$  increases, the wall temperature in the region of deteriorated heat transfer increases. For any given  $Pr_t$ , the code fails to predict the decrease in the wall temperature at the outlet of the pipe.

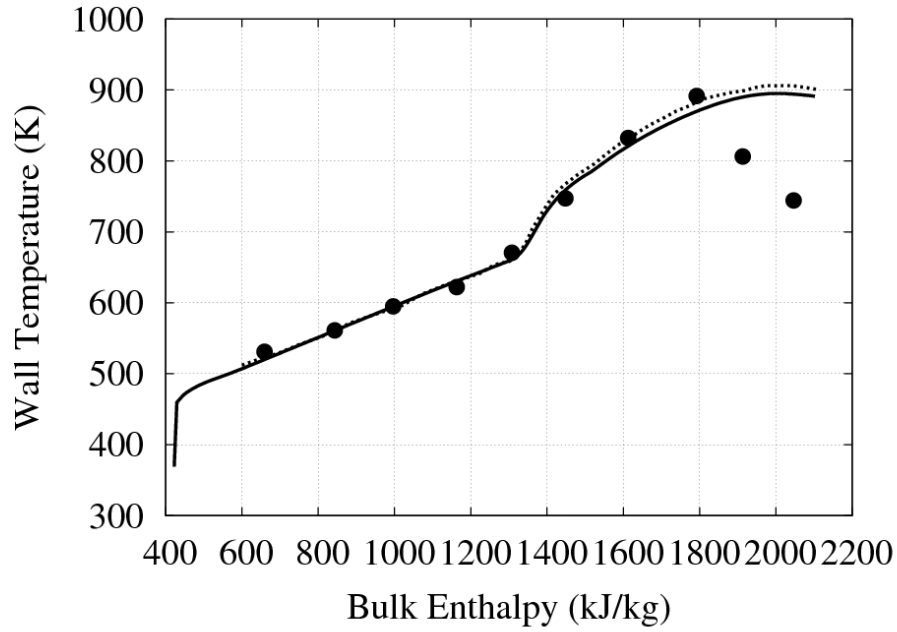


Figure 5.18: Comparison of wall temperature with Ornatsky's experiment and Jaromin and Anglart's numerical work-  $Pr_t=0.9$  for case T2

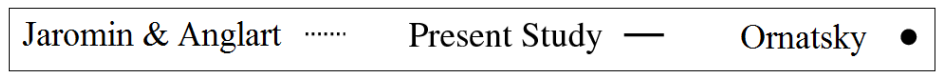
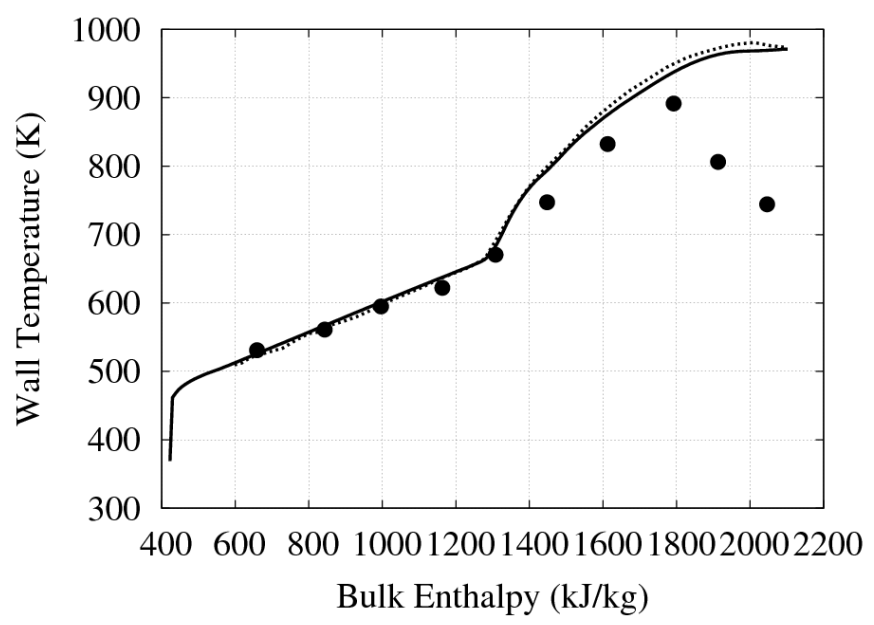


Figure 5.19: Comparison of wall temperature with Ornatsky's experiment and Jaromin and Anglart's numerical work-  $Pr_t=1$  for case T2

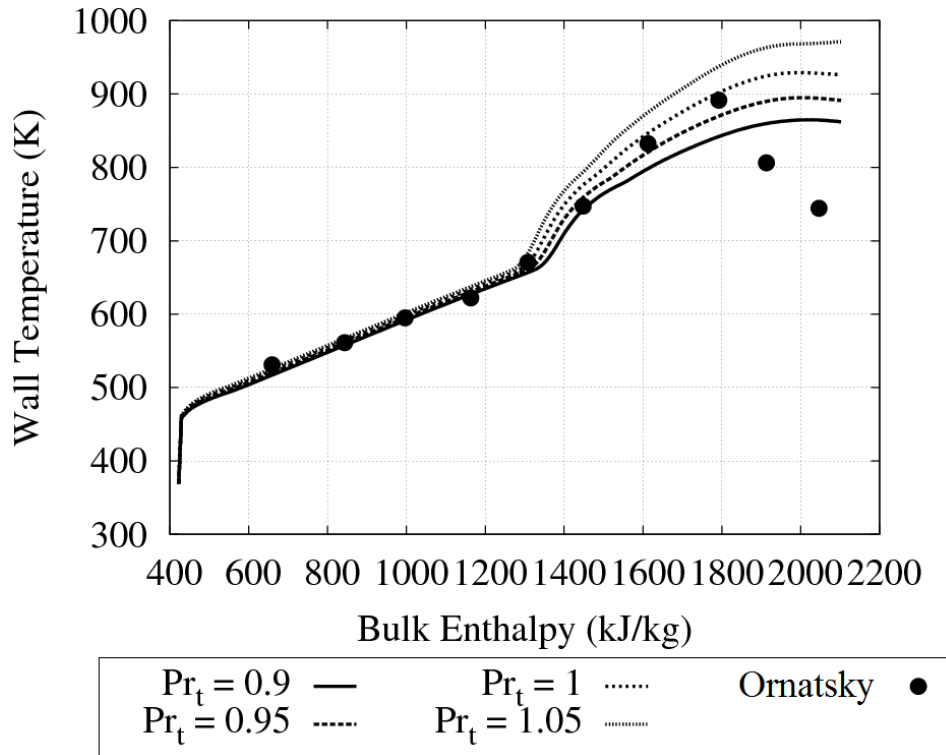


Figure 5.20: Comparison of wall temperature with Ornatsky’s experiment for different  $Pr_t$  numbers for case T2

Table 5.17 shows the RMS deviation of wall temperature from Ornatsky’s experiment for different  $Pr_t$  numbers.  $Pr_t$  equal to 0.9 has the smallest RMS difference with the experimental data and seems to give a better overall agreement of wall temperature along the pipe. Therefore,  $Pr_t$  of 0.9 was considered best for Ornatsky’s case.

Table 5.17: RMS deviation of wall temperature from Ornatsky’s experiment for different  $Pr_t$  numbers for case T2

<b>Turbulent Prandtl Number</b>	<b>RMS Difference (K)</b>
<b>0.9</b>	46.33
<b>0.95</b>	55.35
<b>1</b>	70.23
<b>1.05</b>	90.52

- Best value of  $Pr_t$

In the present study,  $Pr_t$  number of 0.95, which is the average of  $Pr_t$  numbers that best agreed with experimental data of Shitsman and Ornatsky, was selected for the remaining simulations.

## 5.4 Pressure Drop of Supercritical flow

### 5.4.1 Pressure Terminology in CFX

To validate the pressure drop with the experimental data, it is necessary to identify different pressure drop components. The pressure component can be obtained directly from built-in CFX functions or could be calculated using the flow solution. Below is the list of pressures that are used in the current numerical simulation with the abbreviation used to identify each term.

*Pressure-related terms available directly in CFX:*

Modified Pressure ( $P'$ ): This term is also called motion pressure. For certain turbulence models (e.g.  $k-\varepsilon$ ,  $k-\omega$ , and Reynolds Stress) this pressure includes an additional term due to the turbulence normal stress. When buoyancy is activated, this term excludes the hydrostatic pressure field.

Shear Stress ( $\tau$ ): Shear stress arises from the force vector component parallel to the cross section when specifying non-slip condition on the walls.

Total Pressure ( $P_{tot}$ ): For materials with variable density and specific heat like supercritical fluid, static enthalpy, static pressure and static entropy are used to calculate total pressure. These calculations are done within CFX and results can be used directly.

Reference Pressure ( $P_{ref}$ ): Reference Pressure is a property of the entire simulation. All relative pressures in CFX are set relative to this pressure. As a result, this pressure affects the value of all pressures in the domain.

Absolute Pressure ( $P_{abs}$ ): Absolute pressure includes the hydrostatic pressure and is useful when the true pressure is required to calculate the fluid properties. Absolute pressure is related to other pressure components as followed:

$$P_{abs} = P' + P_{ref} + \rho_{ref}g (\vec{x} - \overline{x_{ref}}) \quad (5.7)$$

where  $\overline{x_{ref}}$  is a reference location for buoyancy. By default, CFX sets the reference location at the centroid of one of the pressure-specified boundaries

*Pressure terms not given in CFX directly:*

Hydrostatic Pressure ( $P_{hyd}$ ): In flows where gravity is important, hydrostatic pressure is modeled by including the buoyancy, using:

$$P_{hyd} = \rho_{ref}g (\vec{x} - \overline{x_{ref}}) \quad (5.8)$$

Static Pressure ( $p$ ): To be consistent with the 1-D code terminology, Static pressure is shown by “ $p$ ”. Static pressure is related to absolute pressure by:

$$P_{abs} = p + P_{ref} \quad (5.9)$$

In the current CFD simulation, upward flow is analyzed in all of the cases and therefore buoyancy force exists. Therefore the static pressure in Equation (5.9) includes the component of hydrostatic pressure. So the difference of  $p$  and  $P'$  is the inclusion of hydrostatic pressure in  $p$  as follows:

$$p = P' + P_{hyd} \quad (5.10)$$

Acceleration Pressure ( $P_{acc}$ ): This pressure component is due to the density change in single-phase flows. The acceleration pressure drop between two locations along the pipe is calculated using:

$$\Delta P_{acc} = G^2 \left[ \frac{1}{\rho_2} - \frac{1}{\rho_1} \right] = (\rho_2 u_2^2 - \rho_1 u_1^2) \quad (5.11)$$

Gravitational Pressure ( $P_{gr}$ ): Gravitational pressure is caused by difference in elevation. The gravitational pressure drop between two locations along the pipe is calculated as follows:

$$\Delta P_{gr} = g \int \rho \, dx \quad (5.12)$$

Frictional Pressure ( $P_f$ ): Frictional Pressure is caused by the shear stress at the wall and can be obtained directly from CFX or by using the momentum equation. In the following section, the method for obtaining frictional Pressure is discussed in detail.

#### 5.4.2 Verification of Pressure Drop Using a Momentum Balance

In general, the pressure drop in supercritical flow is caused by four factors: frictional resistance, local flow obstruction, acceleration of flow and gravity (for vertical flow). In absence of loss coefficients, the momentum equation for a steady-state flow is written as:

$$\left( \frac{\partial(\rho U_j U_i)}{\partial x_j} \right) = -\frac{\partial P'}{\partial x_i} + \frac{\partial}{\partial x_j} \left( (\mu + \mu_t) \left[ \frac{\partial U_i}{\partial x_j} + \frac{\partial U_j}{\partial x_i} \right] \right) + S_{M,buoy} \quad (5.13)$$

where  $S_{M,buoy}$ , is added for buoyancy calculations and is equal to:

$$S_{M,buoy} = (\rho - \rho_{ref}) g_i \quad (5.14)$$

By replacing  $(\mu + \mu_t) \left[ \frac{\partial U_i}{\partial x_j} + \frac{\partial U_j}{\partial x_i} \right]$  with  $\tau_{ij}$  in Equation (5.13) and rearranging the equation, it becomes:

$$\left( \frac{\partial(\rho U_j U_i)}{\partial x_j} \right) + \rho_{ref} g_i = -\frac{\partial P'}{\partial x_i} + \frac{\partial \tau_{ij}}{\partial x_j} + \rho g_i \quad (5.15)$$

Writing Equation (5.15) in the  $x_1$  direction, it becomes:

$$\left( \frac{\partial(\rho U_j U_1)}{\partial x_j} \right) + \rho_{ref} g_1 = -\frac{\partial P'}{\partial x_1} + \frac{\partial \tau_{1j}}{\partial x_j} + \rho g_1 \quad (5.16)$$

Neglecting the insignificant terms of Equation (5.16), using linear approximations, and rewriting Equation (5.16) based on a pressure force gradient, it becomes:

$$\frac{\Delta P' A}{\Delta x_1} + \rho_{ref} g_1 A = -\frac{\Delta(\rho_1 U_1^2) A}{\Delta x_1} + \frac{\Delta \tau_{w1} A'}{\Delta x_1} + \frac{g_1 A \int \rho dx}{\Delta x_1} \quad (5.17)$$

where A is the cross sectional area, A' is the surface area of the pipe, and  $\tau_{w1}$  is the shear stress along the wall.

Also, the frictional pressure drop and the shear stress between two locations along the pipe are related using the following:

$$\Delta \tau_{w1} A' = \Delta P_{f1} A \quad (5.18)$$

The left hand side term in Equation (5.18) can be obtained from CFX directly. Therefore, there are two methods for obtaining the frictional pressure drop. It can be obtained directly from CFX by determining the pressure force along the wall. The other way of obtaining the frictional pressure drop is using Equation (5.17). To verify that pressure drop components are calculated correctly, the frictional pressure drops obtained from these methods were compared. First, the pipe was divided in to 1000 parts and for each two locations along the pipe, separated by a distance  $\Delta x$ , Equation (5.19) was used to determine pressure drop components.

$$\frac{\Delta P' A}{\Delta x_1} + \rho_{ref} g_1 A = -\frac{\Delta(\rho_1 U_1^2) A}{\Delta x_1} + \frac{\Delta \tau_{w1} A'}{\Delta x_1} + \frac{g_1 A \int \rho dx}{\Delta x_1} \quad (5.19)$$

(1)            (2)            (3)            (4)            (5)

where  $\Delta = (\text{properties at point 1} - \text{properties at point 2})$  along the pipe. The flow conditions used to verify pressure drop terms are shown in Table 5.18.

Table 5.18: Flow conditions for the case used to verify pressure drop terms

System Pressure (MPa)	Inlet Temperature (C)	Power (kW)	Mass Flow Rate (kg/s)	K Factor
25	350	100	0.068	0

Figure 5.21 shows the variation of both sides of Equation (5.19) vs. the non-dimensional length of the pipe. As shown, the left hand side and the right hand side of the equation are similar.

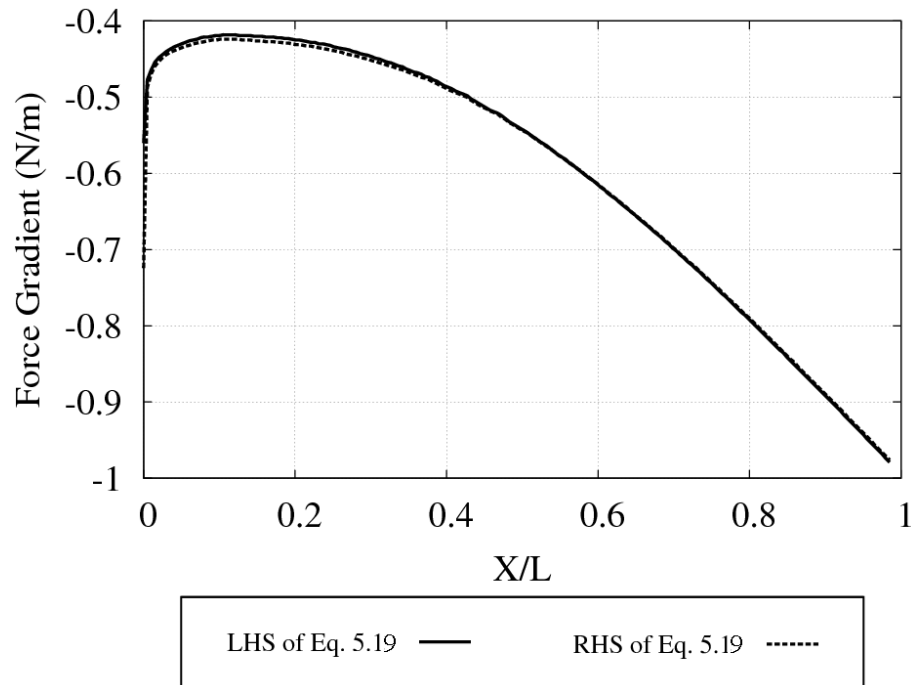


Figure 5.21: Comparison of right and left hand sides of Equation (5.19) vs. the non-dimensional length of the pipe

Figure 5.22 shows the variation different terms of Equation (5.19) with the non-dimensional length of the pipe.

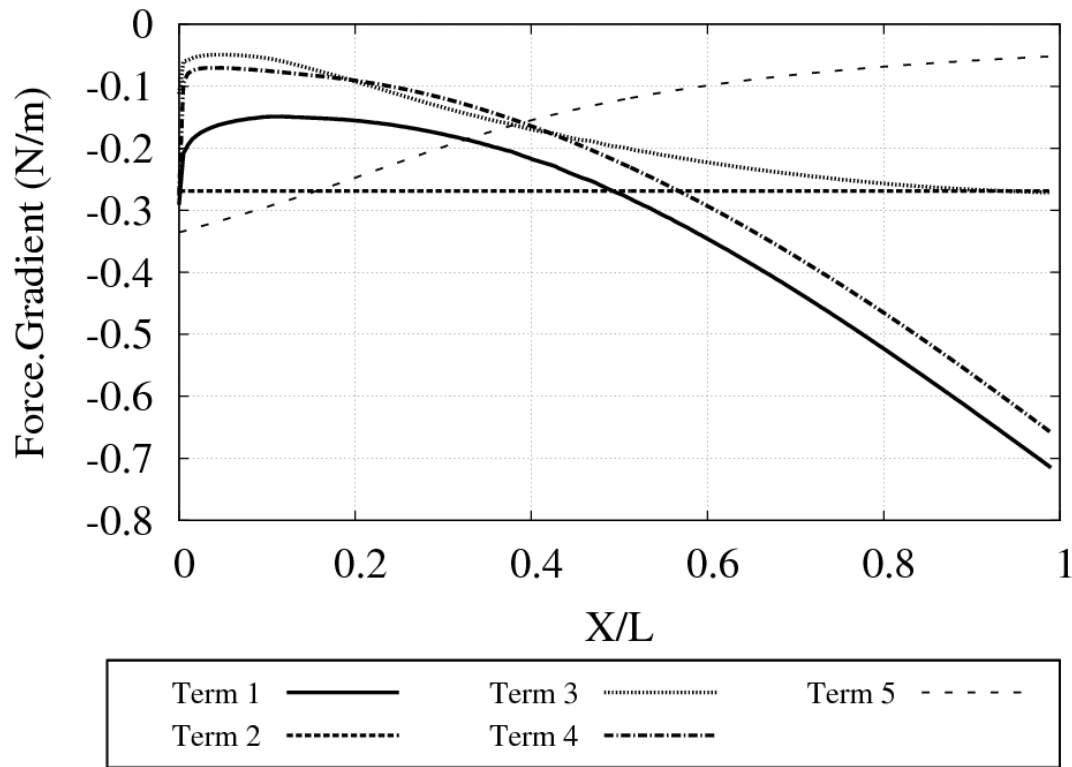


Figure 5.22: Variation of different terms in Equation (5.19) vs. the non-dimensional length of the pipe

Figure 5.23 shows the comparison of frictional pressure drops obtained using the shear stress directly from CFX and Equation (5.19). Since both methods produce the same frictional pressure drop, it can be concluded that the frictional pressure drop is calculated correctly.

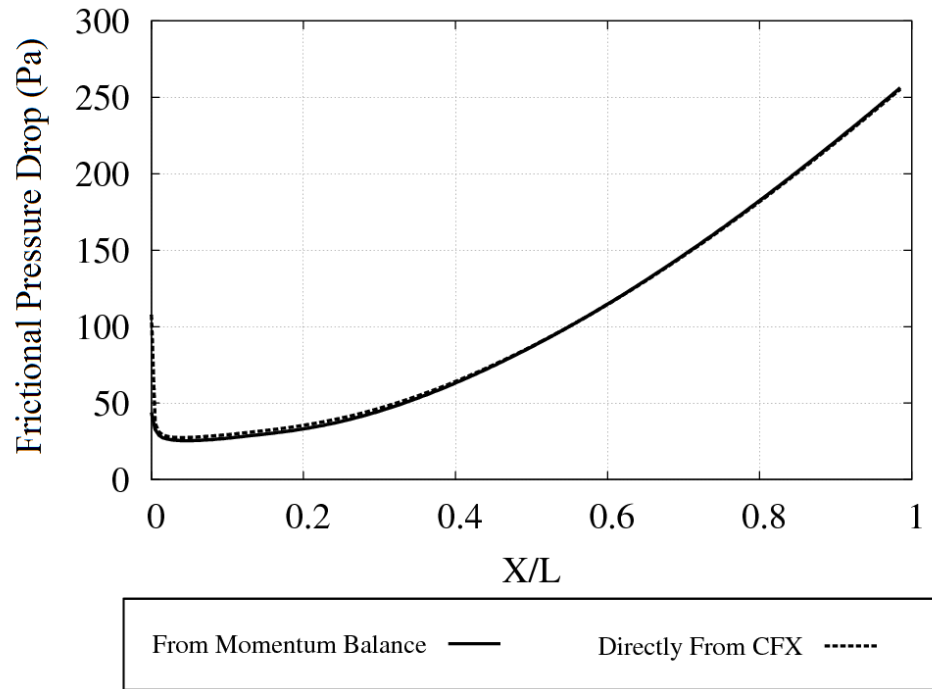


Figure 5.23: Comparison of frictional pressure drops between two methods

## 5.5 Comparison with Experimental Results

### 5.5.1 Comparison of Frictional Pressure Drop from CFX with Experimental Results

Table 5.19 summarizes flow conditions and geometry specifications for the dataset chosen (Ishigai et al, 1981).

Table 5.19: Flow conditions for the cases used to validate the CFX code

Reference Pressure (MPa)	G (kg/m <sup>2</sup> s)	Power (kW)	Pipe Diameter (mm)	Pipe Length (m)
25.3	1000	2.237	3.92	0.625

The experiment of Ishigai et al. (1962) was conducted with different inlet temperatures while other flow conditions remained fixed. Figure 5.24 shows the comparison of CFD results using both the SST model and the  $k-\varepsilon$  model with the experimental data. Each

point on Figure 5.24 corresponds to a specific inlet temperature. The  $k-\varepsilon$  turbulence model under-predicts the frictional pressure drop. However, both turbulence models show good agreement with the experimental data

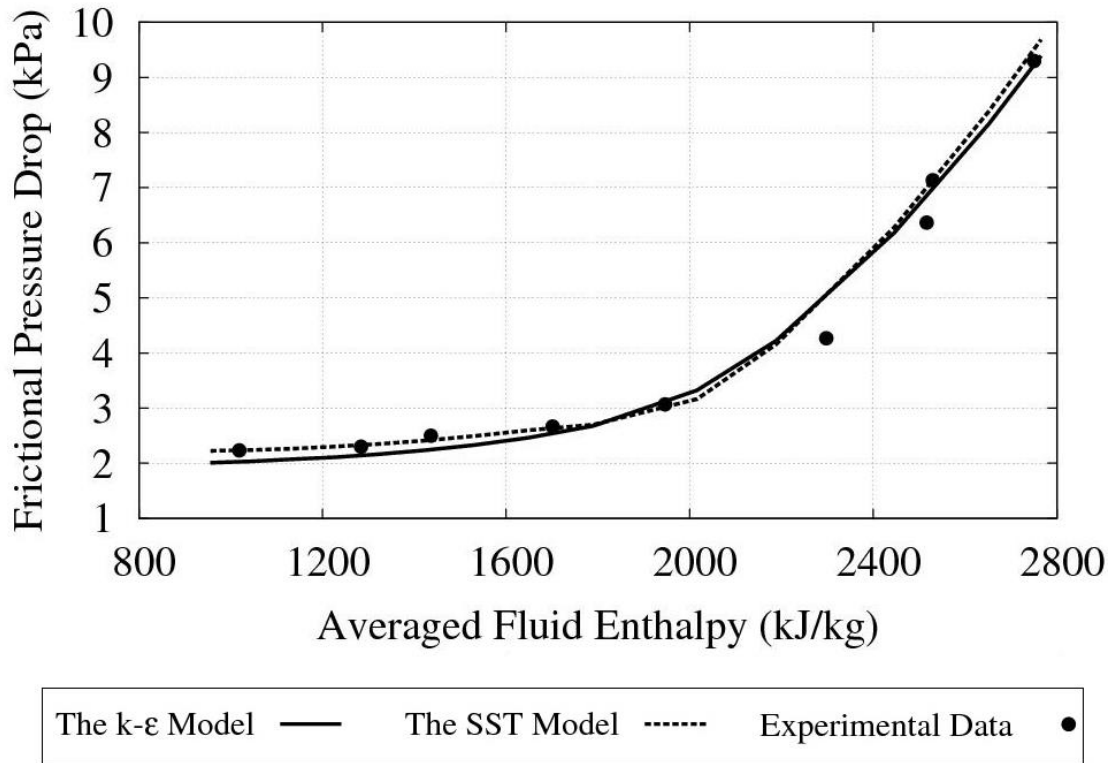


Figure 5.24: Comparison of frictional pressure drop using the SST and the  $k-\varepsilon$  models with experimental results

### 5.6 Grid Independence Study: Ambrosini’s Geometry

The computational domain for this study was discussed in Chapter 3. This section presents mesh-independence tests that were performed using this case.

Table 5.20 summarizes flow conditions and geometry specifications for this case. This case was used since it has heat transfer deterioration near the outlet of the flow and therefore needs an adequately fine grid to simulate the flow behaviour accurately.

Table 5.20: Flow conditions for mesh-independence check using Ambrosini’s geometry

<b>System Pressure (MPa)</b>	<b>Inlet Temperature (K)</b>	<b>Mass Flux (kg/m<sup>2</sup>s)</b>	<b>Heat Flux (kW/m<sup>2</sup>)</b>	<b>Pipe Diameter (mm)</b>	<b>Pipe Length (m)</b>	<b>Outlet K factor</b>
25	323.15	911.35	893	8.36	4.2672	15

Ten grids with different numbers of nodes in different sections were created to examine the number of axial nodes, radial nodes, angular nodes, and near-wall spacing and to determine a grid with acceptable numerical accuracy. The grids used to study mesh independence using Ambrosini’s geometry are listed in Table. 5.21.

Table 5.21: Grids used for mesh-independence check for the Ambrosini test case

<b>Grid</b>	<b>Number of Nodes</b>			<b>First Near-Wall Spacing [mm]</b>	<b>Maximum y<sup>+</sup></b>
	<b>Axial</b>	<b>Radial</b>	<b>Angular</b>		
<b>1-A</b>	250	100	7	$1 \times 10^{-3}$	0.65
<b>2-A</b>	440	100	7	$1 \times 10^{-3}$	0.65
<b>3-A</b>	600	100	7	$1 \times 10^{-3}$	0.65
<b>4-A</b>	440	50	7	$1.5 \times 10^{-4}$	0.1
<b>5-A</b>	440	100	7	$1.5 \times 10^{-4}$	0.1
<b>6-A</b>	440	150	7	$1.5 \times 10^{-4}$	0.1
<b>7-A</b>	440	100	11	$1 \times 10^{-3}$	0.65
<b>8-A</b>	440	100	15	$1 \times 10^{-3}$	0.65
<b>9-A</b>	440	100	7	$4 \times 10^{-4}$	0.26
<b>10-A</b>	440	100	7	$5 \times 10^{-5}$	0.033

The axial variation average angular of wall temperature and the static pressure drop along the tube length were compared between the grids. Table 5.22 shows the maximum

percentage difference and the RMS difference of axial variation of average angular wall temperature and static pressure drop between different grids.

Table 5.22: RMS and maximum percentage deviation of axial variation of average angular wall temperature and static pressure drop between grids for the Ambrosini test case

Parameter studied	Grids compared	Static Pressure Drop		Wall Temperature	
		RMS Difference (Pa)	Max. Difference (%)	RMS Difference (K)	Max. Difference (%)
Number of axial nodes	1-A and 2-A	41.03	0.73	35.29	20.22
	2-A and 3-A	3.21	0.13	0.48	0.73
Number of radial nodes	4-A and 5-A	37.62	2.05	16.41	7.20
	5-A and 6-A	3.66	0.74	0.77	0.35
First Near-Wall Spacing	9-A and 5-A	11.2	0.5	5.38	2.25
	5-A and 10-A	12.8	0.72	3.32	1.35

From the results shown in Table 5.22, 440 nodes in axial direction and 100 nodes in radial direction were considered adequate. The results of average angular wall temperature are sensitive to the  $y^+$  of the grid due to the strong variation of near-wall thermo-physical properties at supercritical pressures. The maximum percentage difference between grids 5-A and 10-A is about 1.35%. Due to convergence problems at very small values of  $y^+$ , the variation of average angular wall temperature are examined in detail. Figures 5.25 and 5.26 show the variation of average angular wall temperature and static pressure drop along the pipe using different maximum  $y^+$  values. As the value of  $y^+$  decreases and the mesh becomes more refined near the wall, the peak in the average angular wall temperature shifts slightly toward the outlet in the  $x$  direction and the value

of average angular wall temperature at the peak reduces. However, between grids 5-A and 10-A the average angular wall temperature does not change considerably and the maximum  $y^+$  of 0.1 was found sufficient for grid independency. Both 9-A and 5-A are capable of predicting the static pressure drop in the pipe.

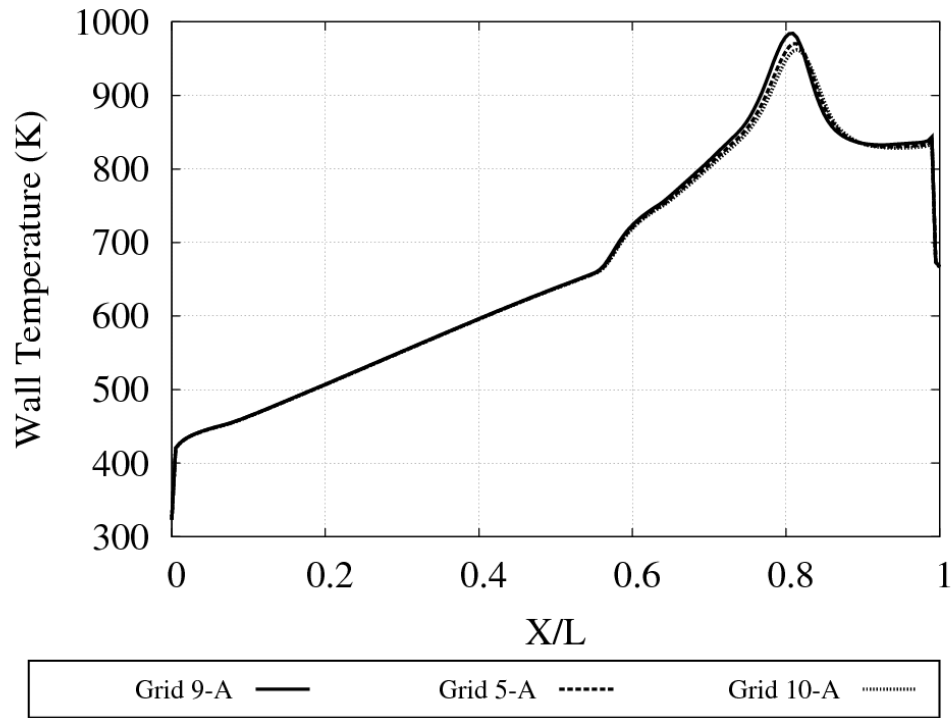


Figure 5.25: Effect of near-wall spacing on average angular wall temperature along the pipe for the Ambrosini test case

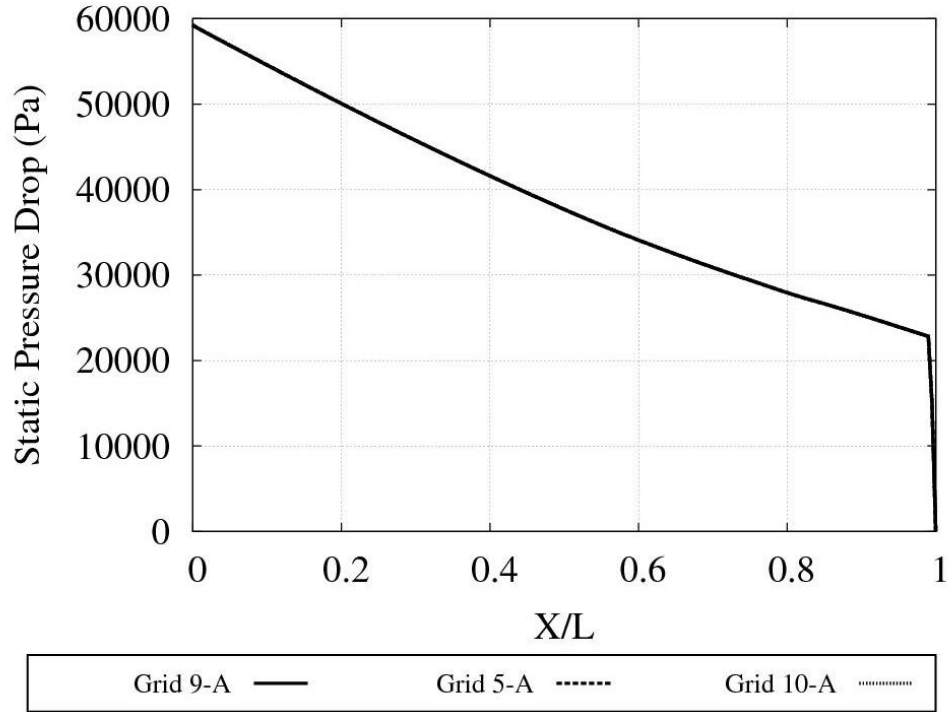


Figure 5.26: Effect of near-wall spacing on static pressure drop along the pipe for the Ambrosini test case

To study the effect of number of angular nodes, the maximum difference of wall temperature in the angular direction at each axial location along the pipe was compared between grids and is shown in Figure 5.27. This figure suggests that Grid 2-A with 7 nodes in the angular direction produces a more uniform angular temperature distribution compared to 11, and 15 numbers of nodes. Grid 2-A also has a maximum variable in temperature of less than 0.06 K which is acceptable.

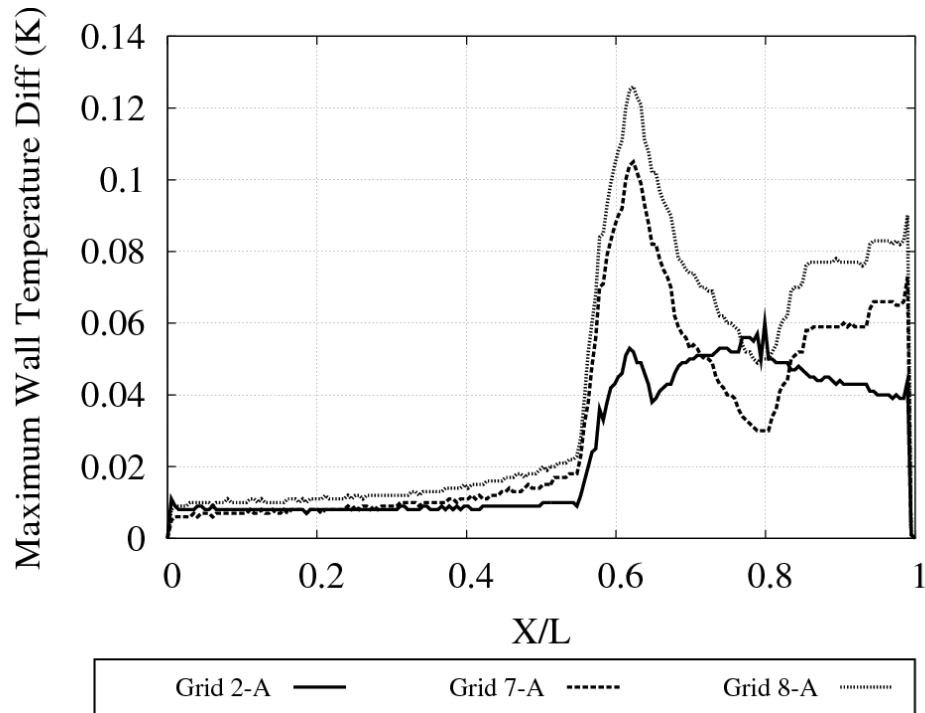


Figure 5.27: Maximum difference in angular wall temperature at each axial location along the pipe for the Ambrosini test case

The mesh-independence tests were also conducted using coarse, medium, and fine meshes of 89,750, 311,960, and 635,400 nodes, respectively. Table 5.23 shows the number of nodes in different sections of the grids.

Table 5.23: Grids used to study the effect of changing the number of radial and axial nodes simultaneously for the Ambrosini test case

Grid	Number of Nodes			First Near-Wall Spacing (mm)
	Axial	Radial	Angular	
Coarse-A	250	50	7	$1.5 \times 10^{-4}$
Medium-A	440	100	7	$1.5 \times 10^{-4}$
Fine-A	600	150	7	$1.5 \times 10^{-4}$

The axial variation of average angular wall temperature and the static pressure drop along the tube length were determined and compared between grids. Table 5.24 shows the maximum percentage difference and the RMS difference of average angular wall temperature and static pressure drop between coarse, medium and fine grids. Since the percentage and RMS error between the medium and fine grids were small, the medium grid was considered suitable.

Table 5.24: RMS and maximum percentage deviation of axial variation of average angular wall temperature and static pressure drop between coarse, medium and fine grids for the Ambrosini test case

<b>Grids compared</b>	<b>Static Pressure Drop</b>		<b>Wall Temperature</b>	
	<b>RMS Difference (Pa)</b>	<b>Max. Difference (%)</b>	<b>RMS Difference (K)</b>	<b>Max. Difference (%)</b>
<b>Coarse- A and Medium-A</b>	89.69	0.29	34.59	25.45
<b>Medium-A and Fine-A</b>	2.61	0.02	0.79	0.55

Figures 5.28 and 5.29 show the variation of average angular wall temperature and static pressure along the pipe for coarse, medium and fine grids. The results for the coarse grid in Figure 5.28 were double checked. It is not clear why there are such strong oscillations in the wall temperature for this particular case. It might be due to the low number of axial nodes used.

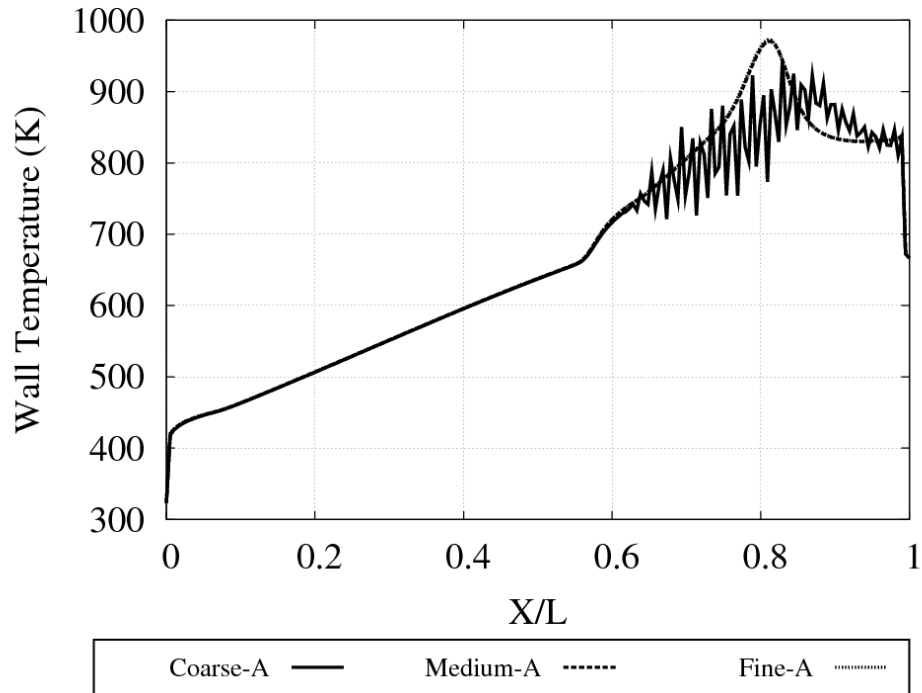


Figure 5.28: Comparison of average angular wall temperature between three grids for the Ambrosini test case

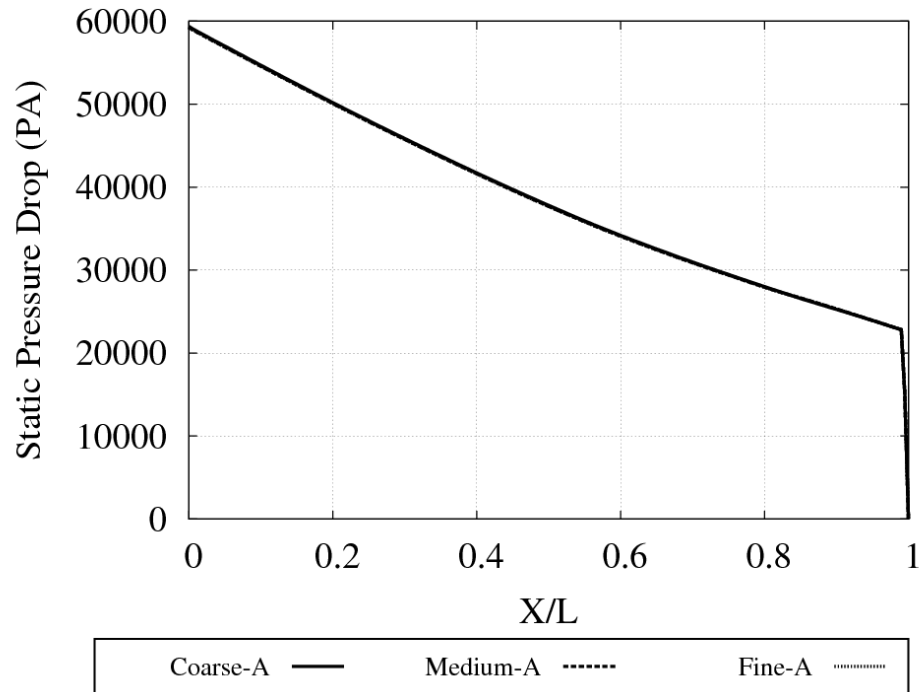


Figure 5.29: Comparison of static pressure between three grids for the Ambrosini test case

Two radial lines at the middle and at the outlet of pipe were defined to study the mesh independence for variations in radial direction. Table 5.25 shows the maximum percentage difference and the RMS difference of velocity between coarse, medium and fine grids. The percentage and RMS error between the medium and fine grids are small, so the medium grid is considered suitable.

Table 5.25: RMS and maximum percentage deviation of radial velocity between coarse, medium and fine grids for the Ambrosini test case

Grids compared	Outlet Radial Velocity		Radial Velocity at $\frac{x}{L} = \frac{1}{2}$	
	RMS Difference (K)	Max. Difference (%)	RMS Difference (Pa)	Max. Difference (%)
Coarse-A and Medium-A	0.018	1.1	0.0014	0.66
Medium-A and Fine-A	0.0017	0.23	8.9e-5	0.058

Figures 5.30 and 5.31 show the variation of radial velocity at the middle and at the outlet of the pipe, respectively, for coarse, medium and fine grids. There is a slight difference between the coarse and medium grids. However, the medium grid gives the same results as the fine grid both at the middle and at the outlet of the pipe.

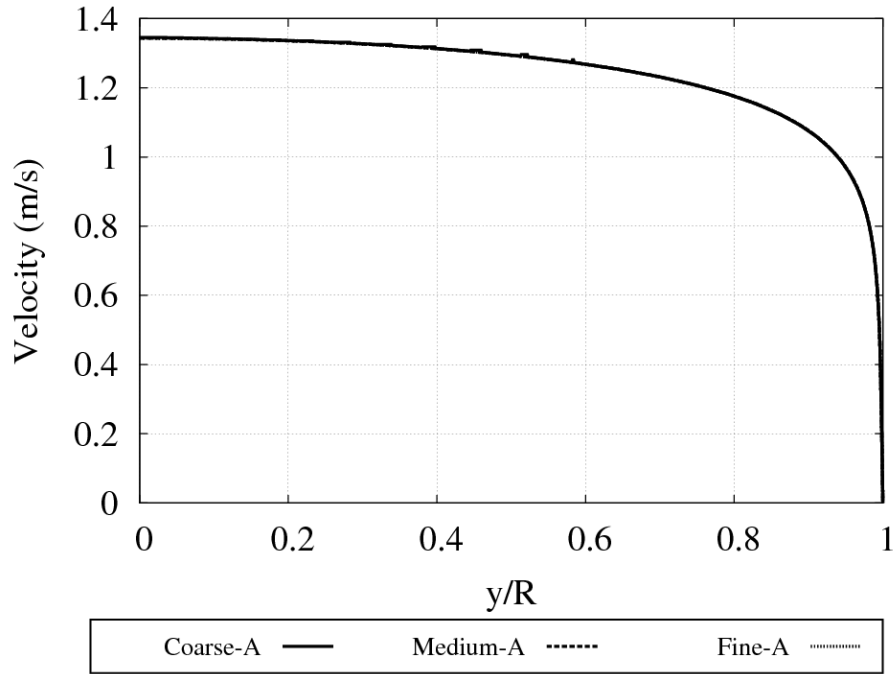


Figure 5.30: Comparison of radial variation of velocity at  $\frac{x}{L} = \frac{1}{2}$  between three grids for the Ambrosini test case

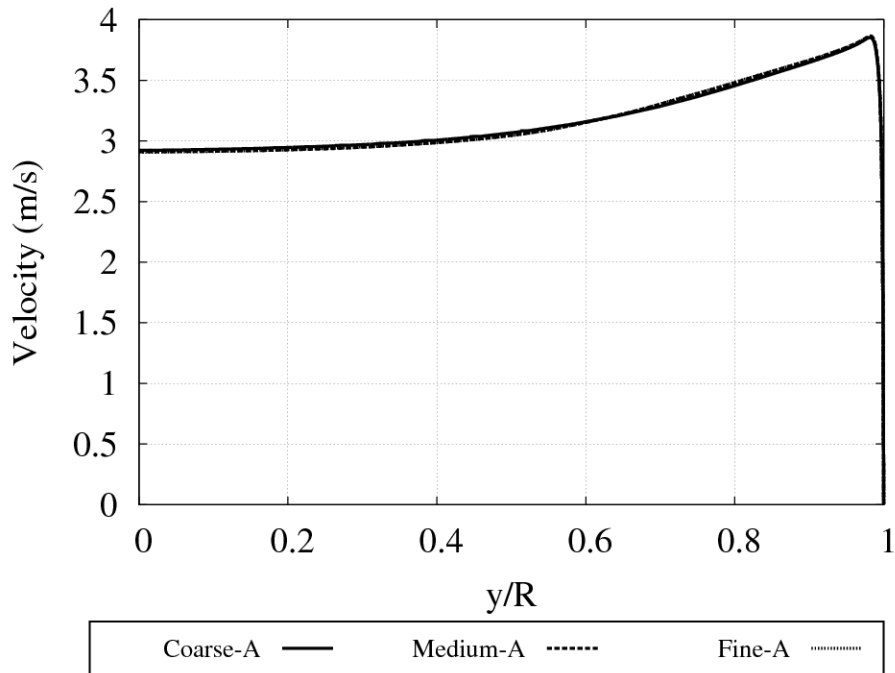


Figure 5.31: Comparison of radial variation of outlet velocity between three grids for the Ambrosini test case

Table 5.26 shows the maximum percentage difference and the RMS difference of temperature between coarse, medium and fine grids along the radial lines at the middle and at the outlet of the pipe. The percentage and RMS error between the medium and fine grids are small enough to consider the medium grid suitable.

Table 5.26: RMS and maximum percentage deviation of radial temperature between coarse, medium and fine grids for the Ambrosini test case

Grids compared	Outlet Radial Temperature		Radial Temperature at $\frac{x}{L} = \frac{1}{2}$	
	RMS Difference (K)	Max. Difference (%)	RMS Difference (Pa)	Max. Difference (%)
Coarse-A and Medium-A	0.11	0.025	0.14	0.16
Medium-A and Fine-A	0.019	0.017	0.046	0.047

Figures 5.32 and 5.33 show the variation of radial temperature at the middle and at the outlet of the pipe, respectively, for coarse, medium and fine grids. There is a slight difference between the coarse and medium grids especially at the outlet of the pipe. However, the medium grid gives the same results as the fine grid both at the middle and at the outlet of the pipe.

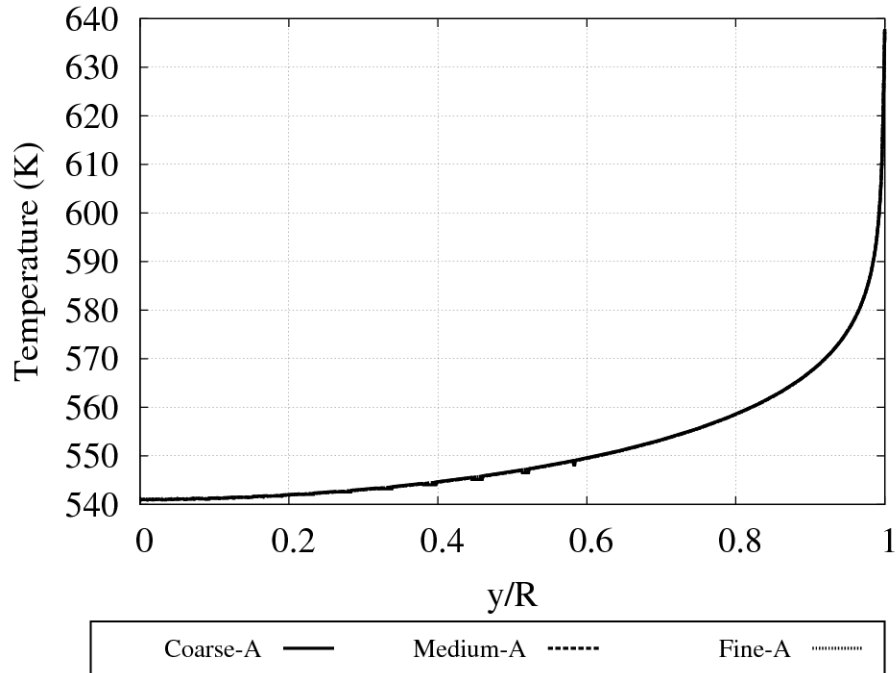


Figure 5.32: Comparison of radial variation of temperature at  $\frac{x}{L} = \frac{1}{2}$  between three grids for the Ambrosini test case

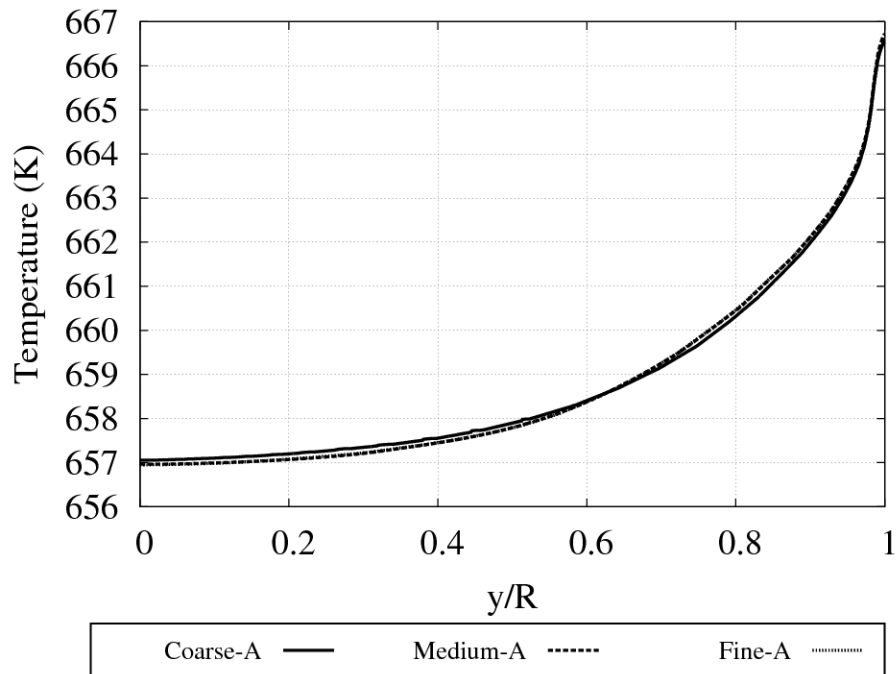


Figure 5.33: Comparison of radial variation of outlet temperature between three grids for the Ambrosini test case

Table 5.27 shows the maximum percentage difference and the RMS difference of static pressure between coarse, medium and fine grids along a radial line at the middle of the pipe. This table also confirms that the medium grid produces an acceptable solution.

Table 5.27: RMS and maximum percentage deviation of radial pressure between coarse, medium and fine grids for the Ambrosini test case

<b>Grids compared</b>	<b>Radial Pressure Difference at <math>\frac{x}{L} = \frac{1}{2}</math></b>	
	<b>RMS Difference (Pa)</b>	<b>Max. Difference (%)</b>
<b>Coarse-A and Medium-A</b>	102.19	0.29
<b>Medium-A and Fine-A</b>	4.5	0.06

Finally, since a very small value of  $y^+$  was used in the simulations, to decrease the maximum aspect ratio of the grid and improve the convergence rate, 600 axial nodes were implemented in the final mesh.

The specifications of the final grid used in the simulations are shown in Table 5.28.

Table 5.28: The final grid used in the simulations for the Ambrosini test case

<b>Number of Nodes</b>			<b>First Near-Wall Spacing (mm)</b>
<b>Axial</b>	<b>Radial</b>	<b>Angular</b>	
600	100	7	$1.5 \times 10^{-4}$

## CHAPTER 6

### RESULTS AND DISCUSSION

#### 6.1 Introduction

In this chapter, four cases each of static and oscillatory instabilities were performed. Results are presented for the prediction of mass flow rate at the instability threshold in the computational domain, defined in Chapter 3. The effects of  $Pr_t$ , outlet K factor, and inlet temperature on the instability boundary are discussed. Results for both static and oscillatory instabilities are obtained using the  $k-\varepsilon$  and the SST turbulence models and compared with nonlinear 1-D results. Results for one static instability case and one oscillatory instability case are presented and discussed in detail, followed by a summary of results obtained for other cases. An explanation of the behaviour of the flow near the HTD region is also presented in this chapter.

#### 6.2 Determining the instability threshold

The threshold for instability was determined using ANSYS CFX v.14.5 as follows: starting from a relatively high mass flow rate, a steady-state analysis was obtained first to determine the pressure drop between inlet and outlet of the pipe. In this steady-state analysis, the static pressure was specified at the outlet and the mass flow rate was specified at the inlet. This pressure drop was then used to specify the inlet static pressure for a transient analysis. The stability of the flow was determined by monitoring the inlet and outlet mass flow rates during the transient analysis. In the case of static instability, the mass flow rate moves away from its equilibrium position in an excursive manner without returning to the original state (i.e. the mass flow rate drifts from its steady-state value to a higher or a lower value). In this study, for a stable case, a small difference was

observed between the mass flow rate predicted by a transient run and the mass flow rate in the initial conditions that was derived from a steady-state run. This difference is due to the solution of the steady-state equation versus the transient equations. For a typical static instability case that difference was on the order of 0.13%. To ensure that the change in mass flow in a static instability case was due to the instability and not the above-mentioned numerical solution difference, a criterion for a minimum change in mass flow was developed. In this study, criterion of 1% change in mass flow rate was used to declare static instability and the instability threshold was taken as the higher mass flow rate value that the system drifted to over time (at least 20 s is needed to clarify that the flow is stable or unstable).

For oscillatory instability on the other hand, the oscillation amplitudes grow if the flow is unstable. If the flow is stable, any ensuing oscillations diminish with time. In any given case, if the flow was stable, a lower inlet mass flow rate was tried next until sustained or diverging oscillations of mass flow rate was achieved over time (about 10 s is needed to clarify whether the flow is stable or unstable). The instability threshold was stated as the mass flow rate that caused sustained oscillations without amplification or decay in the mass flow rate. To find the instability threshold for a particular case, a significant number of steady-state and transient runs should be done based on a trial and error basis with a sufficient increment of mass flow rate (an increment of 0.0005 kg/s was used in this study). Transient analyses should be performed for a sufficient amount of time to clarify that the flow is stable or unstable and that requires a significant amount of computational costs.

### 6.3 Static and Oscillatory Instability Cases

Tables 6.1 and 6.2 show the specifications of the cases used to study the static and oscillatory instabilities. An explanation is necessary here on the cases chosen to study. For a specific operational pressure and power with no inlet K factor, a combination of different inlet temperatures and outlet K factors can lead to oscillatory or static instabilities. According to Chatoorgoon (2013), above a certain temperature (244°C), static instability is not possible for horizontal flow. Also, the static instability is not very likely to occur in vertical up-flow, unless a relatively high outlet K factor is introduced at the outlet of the flow. Therefore, there are restrictions in choosing flow conditions to encounter either static or oscillatory instabilities. From the preliminary analyses, with the current flow conditions, an outlet K factor higher than 10 and an inlet temperature lower than 244°C was required to obtain static instability. Also the SCW CANDU is suggested to work at an inlet temperature of 350°C and the operational pressure of 25 MPa. Therefore, inlet temperatures of 250°C and 350°C were chosen for oscillatory instability cases and two values of K factor (0 and 10) were selected to study the effect of K factor on the instability threshold.

Table 6.1: Flow conditions for the cases used in the simulations, leading to static instability

<b>Case</b>	<b>Reference Pressure (MPa)</b>	<b>Power (kW)</b>	<b>Inlet Temperature (C)</b>	<b>Outlet K Factor</b>
<b>S1</b>	25	100	50	20
<b>S2</b>	25	100	50	15
<b>S3</b>	25	100	100	20
<b>S4</b>	25	100	100	15

Table 6.2: Flow conditions for the cases used in the simulations, leading to oscillatory instability

Case	Reference Pressure (MPa)	Power (kW)	Inlet Temperature (C)	Outlet K Factor
O1	25	100	250	0
O2	25	100	250	10
O3	25	100	350	0
O4	25	100	350	10

### 6.3.1 CFX Static Instability Results

As discussed in Chapter 3, in the present study, a  $Pr_t$  number of 0.95, which is the average of  $Pr_t$  numbers that best agreed with experimental data of Shitsman and Ornatsky, was selected for the instability simulations. Figure 6.1 shows the inlet mass flow rate time response predicted by the CFD code for an initial mass flow rate of 0.0575 kg/s, an inlet temperature of 50°C, a power of 100 kW, and an outlet K factor of 20 (Case S1). The change in mass flow rate is 1.2%, indicating an unstable system. Figure 6.2 shows the CFD response when the initial mass flow rate was 0.058 kg/s. The change in mass flow rate is 0.65% indicating a stable system. Thus, the instability threshold predicted by the CFD code is between 0.0575 kg/s and 0.058 kg/s. The higher values of instability boundary ranges are reported in this study, to assure the safety of the system.

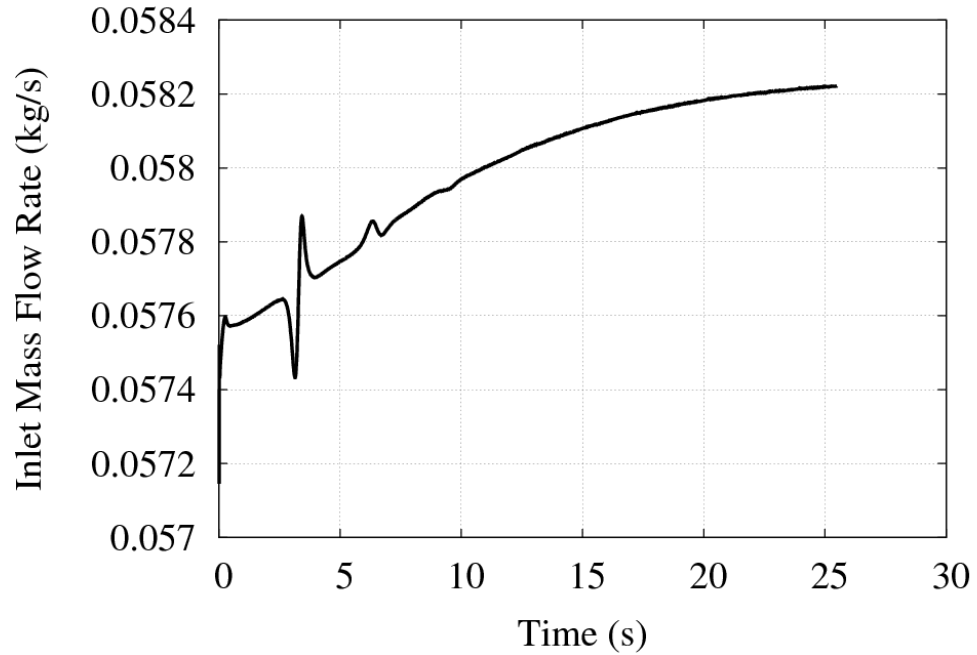


Figure 6.1: CFD results for an unstable case using the SST model for Case S1 ( $\dot{m} = 0.0575 \text{ kg/s}$ )

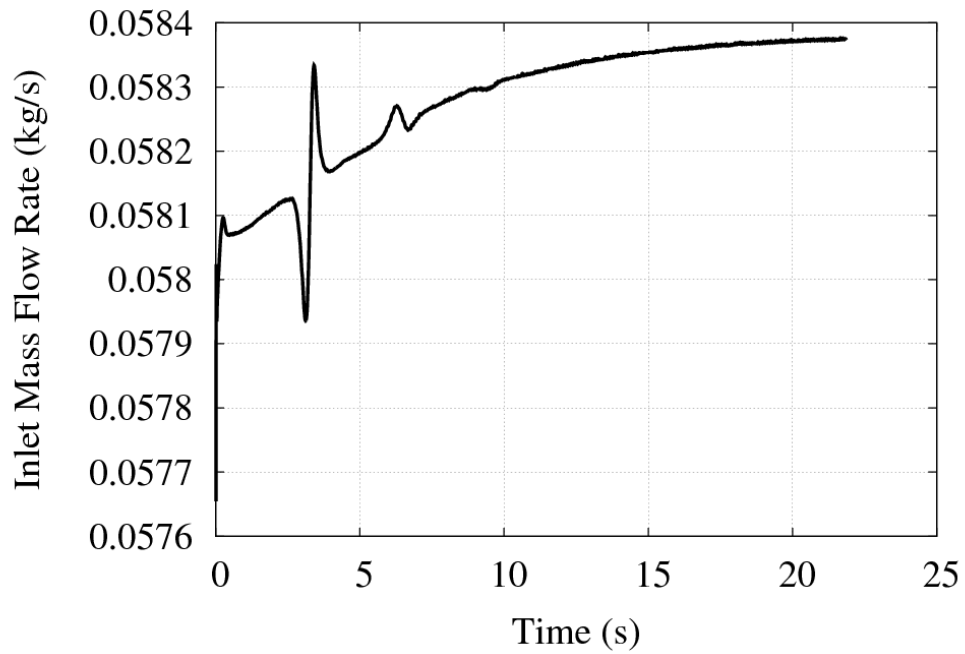


Figure 6.2: CFD results for a stable case using the SST model for Case S1 ( $\dot{m} = 0.058 \text{ kg/s}$ )

Table 6.3 summarizes the static instability threshold results for the cases shown in Table 6.1, using the  $k-\varepsilon$  and the SST turbulence models. Table 6.3 suggests that the results of instability thresholds between the  $k-\varepsilon$  and the SST models are close and the largest difference, which appears in Case S4, is 7.38%.

Table 6.3: Static instability threshold mass flow rates predicted by CFD

Case	CFD Instability Threshold Mass Flow Rate (kg/s)		Difference of Instability Threshold SST and $k-\varepsilon$ models (%)
	$k-\varepsilon$ model	SST model	
<b>S1</b>	0.0585	0.058	0.86
<b>S2</b>	0.053	0.0525	0.95
<b>S3</b>	0.0625	0.0615	1.62
<b>S4</b>	0.0565	0.061	7.38

The SST and the  $k-\varepsilon$  turbulence models give similar predictions of the bulk flow properties. The main region where their results deviate is near the wall, where the SST model uses a much greater resolution of the turbulent boundary layer. To find out the reason for the difference of instability threshold between the  $k-\varepsilon$  and SST models, Case S4 (which has the largest difference) was chosen for examination. Figure 6.3 shows the axial variation of wall temperature for the  $k-\varepsilon$  and SST models for Case S4. Overall, the  $k-\varepsilon$  model appears less capable of resolving the boundary layer, leading to a very different prediction of the wall temperature, compared to the SST model results. The higher wall temperature predicted by the SST model is believed to be more physically realistic.

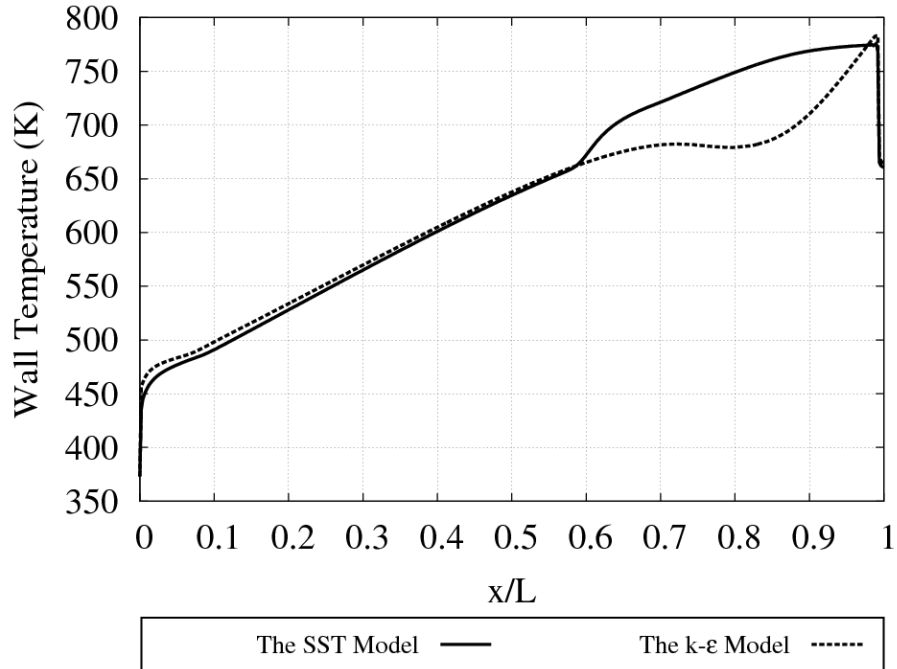


Figure 6.3: Axial wall temperature of the  $k-\varepsilon$  and the SST models for Case S4 ( $\dot{m} = 0.06 \text{ kg/s}$ )

The deficiency of the  $k-\varepsilon$  model in predicting the near-wall behavior of the flow has only a small effect on the axial pressure drop, as shown in Figure 6.4. Furthermore, a significant amount of pressure drop is caused by the outlet K factor, which is not greatly affected by the turbulence model used.

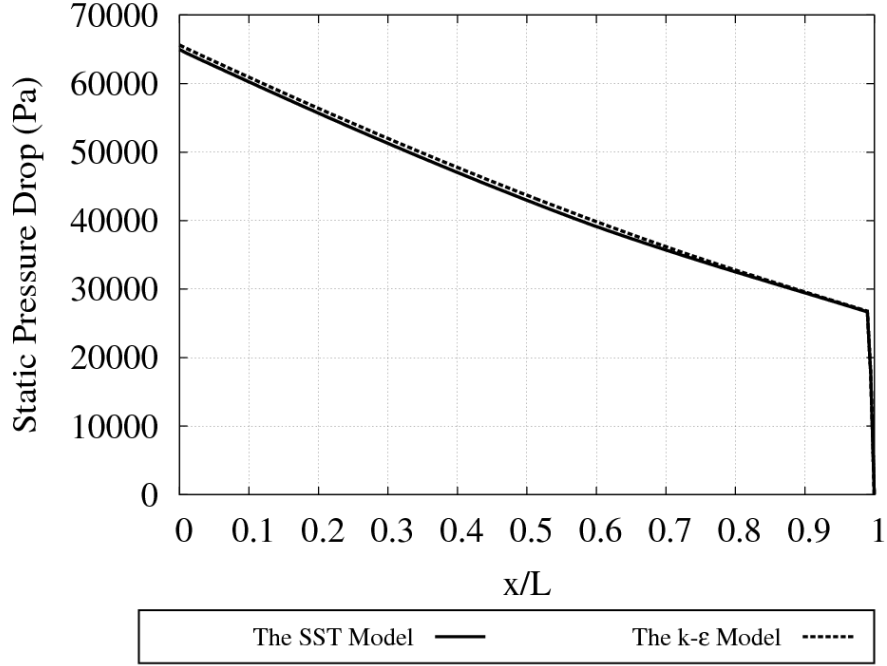


Figure 6.4: Axial static pressure drop of the  $k-\varepsilon$  and the SST models for Case S4 ( $\dot{m} = 0.06$  kg/s)

To find the pressure drop component that causes the difference in the static pressure drop between the  $k-\varepsilon$  and the SST models, the variations of different terms of Equation (6.1) (the same as Equation (5.19)) with the non-dimensional length of the pipe are examined for Case S4 for the region before the K factor, using the  $k-\varepsilon$  and the SST turbulence model.

$$\begin{aligned}
 \frac{\Delta P' A}{\Delta x_1} + \rho_{ref} g_1 A = & - \frac{\Delta(\rho_1 U_1^2) A}{\Delta x_1} + \frac{\Delta \tau_{w1} A'}{\Delta x_1} + \frac{g_1 A \int \rho dx}{\Delta x_1} \quad (6.1) \\
 \text{(T1)} \quad \quad \quad \text{(T2)} \quad \quad \quad \text{(T3)} \quad \quad \quad \text{(T4)} \quad \quad \quad \text{(T5)}
 \end{aligned}$$

The hydrostatic term (T2) stays the same for both turbulence models and the RMS differences of gravitational (T5) and acceleration pressure drops (T3) between the two models are 0.00048 N/m (0.1% of the averaged magnitude along the pipe) and 0.0032 N/m (1% of the averaged magnitude along the pipe), respectively. Other terms of

Equation (6.1) (T1 and T4) are shown in Figure 6.5. This figure shows that the friction force gradient caused by the frictional pressure drop is the main component that is different between the two turbulence models and it causes the difference in the static pressure drop.

For the SST model, the absolute value of force gradient decreases suddenly at the  $x/L$  equal to 0.58. This location corresponds to the onset of heat transfer deterioration. Due to an increase in the wall temperature, the dynamic viscosity decreases and, therefore, the shear stress and the frictional pressure drop decrease. However, the  $k-\varepsilon$  model is not able to predict the near-wall properties and, therefore, it fails to predict the onset of HTD accurately.

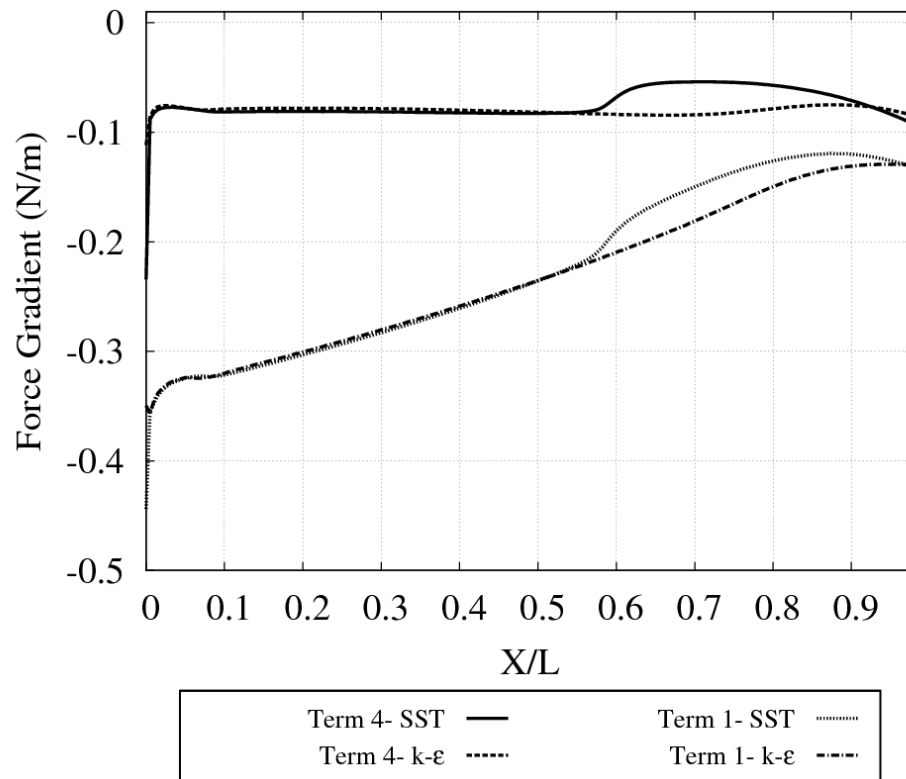


Figure 6.5: Variation of Term 1 and Term 4 in Equation (6.1) versus the non-dimensional length of the pipe using the  $k-\varepsilon$  and the SST models for Case S4 ( $\dot{m} = 0.06$  kg/s)

In Figure 6.5, the reason for the steep variation of the force gradient near the inlet of the flow is the fact that a uniform inlet velocity profile was used.

### 6.3.2 Comparison of CFX Results with 1-D Non-Linear Results for Static Instability

A 1-D non-linear code, SPORTS (Chatoorgoon, 1986) was used to determine the static instability boundary for the same initial flow conditions.

The SPORTS simulations are shown in Figures 6.6 and 6.7, also for an inlet temperature of 50°C, power of 100 kW, and K factor of 20 (Case S1). Figure 6.6 shows a stable response for an initial flow rate of 0.058 kg/s, while Figure 6.7 shows an unstable response for an initial flow rate of 0.056 kg/s. Thus, the 1-D solution deviates from the  $k-\epsilon$  model by 0.85%.

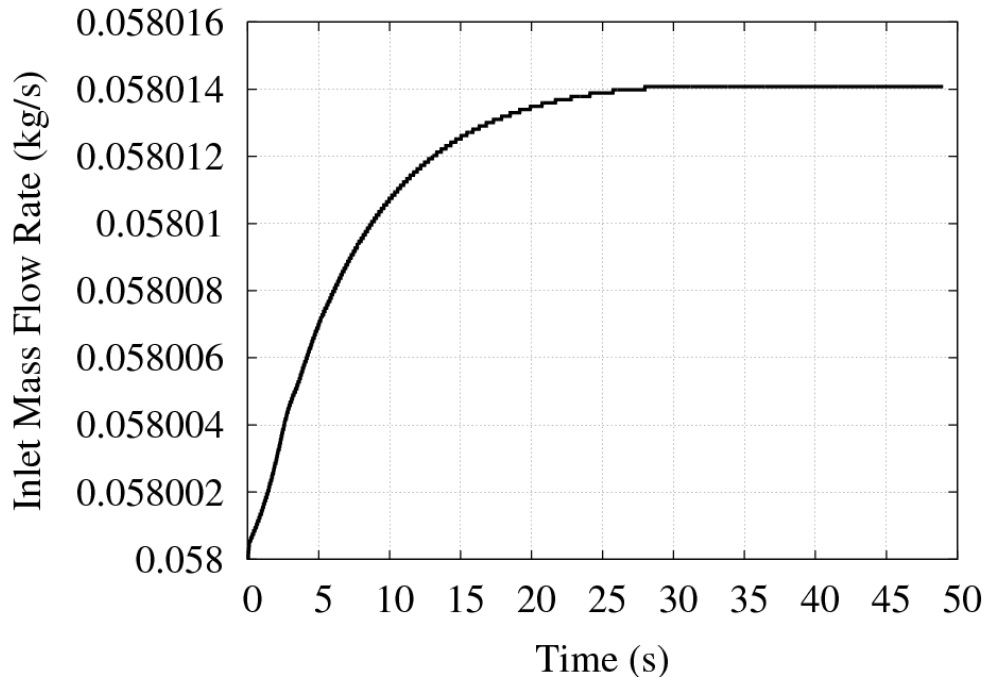


Figure 6.6: 1-D non-linear (SPORTS) results for a stable case for Case S1 ( $\dot{m} = 0.058$  kg/s)

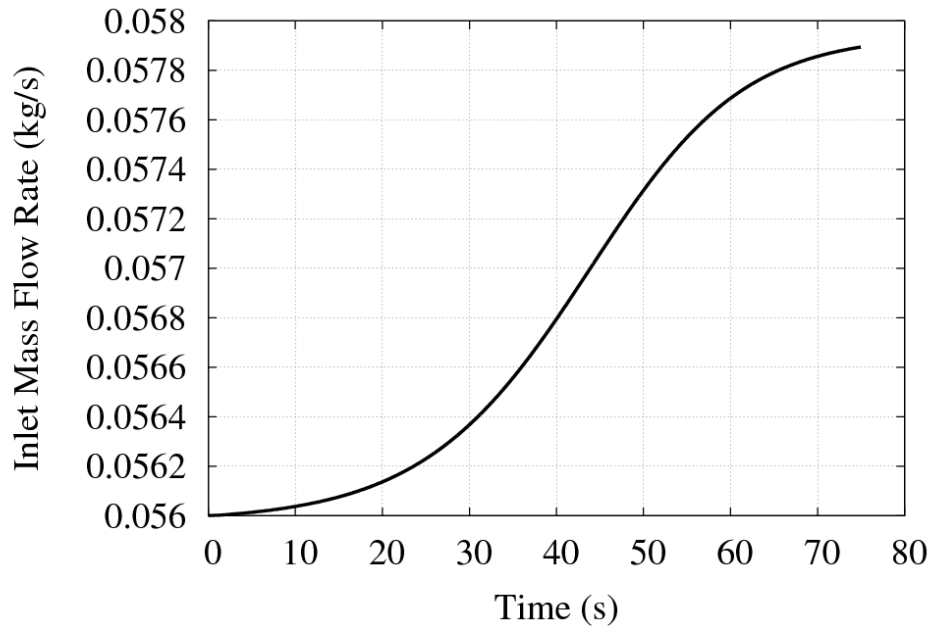


Figure 6.7: 1-D non-linear (SPORTS) results for an unstable case for Case S1 ( $\dot{m} = 0.056$  kg/s)

Table 6.4 summarizes the results of instability analyses using 1-D non-linear code and the comparison of results with the CFX results obtained using the  $k-\epsilon$  and the SST turbulence models. The maximum difference of CFD and 1-D instability threshold is for Case S4, using the  $k-\epsilon$  model.

Table 6.4: Static instability threshold mass flow rates predicted by 1-D code and comparison with CFD

Case	1-D Non-Linear Instability Threshold Mass Flow Rate (kg/s)	Difference of Instability Threshold $k-\epsilon$ model and 1-D Non-Linear Code (%)	Difference of Instability Threshold SST model and 1-D Non-Linear Code (%)
S1	0.058	0.85	0
S2	0.056	5.66	6.67
S3	0.063	0.8	2.44
S4	0.061	7.96	0

One of the reasons for the difference between 1-D and CFD instability results is the difference in the pressure drop prediction between these two codes. While a CFD code with a chosen turbulence model calculates the wall shear automatically via the wall functions used in the momentum equations, a 1-D code must rely on an empirical friction-factor correlation to determine the frictional pressure drop. The SPORTS code uses the Blasius (1913) friction-factor formula for isothermal flow which is as follows:

$$f = 0.184 Re^{-0.2} \quad \text{for} \quad 3000 \leq Re \leq 10^6 \quad (6.2)$$

Figure 6.8 shows the variation of the static pressure drop for 1-D code and the SST model for Case S1 and mass flow rate of 0.058 kg/s. The pressure drop predictions between these two codes are very different because different methods are used by each code to determine the pressure drop. The Blasius friction-factor formula used by SPORTS is calculated based on bulk values of the Reynolds number and it does not take into account the near-wall properties. However, in CFX, the pressure drop is calculated locally using the momentum equations. Also the calculation of pressure drop when having a K factor is not the same between the 1-D and the CFD codes, since 1-D code calculates the pressure drop based on the bulk values of velocity and density, while in CFX, the pressure drop is calculated based on local values of velocity and density and is then area-averaged. The calculations of pressure drop due to K factor will be discussed in more detail in Appendix B.

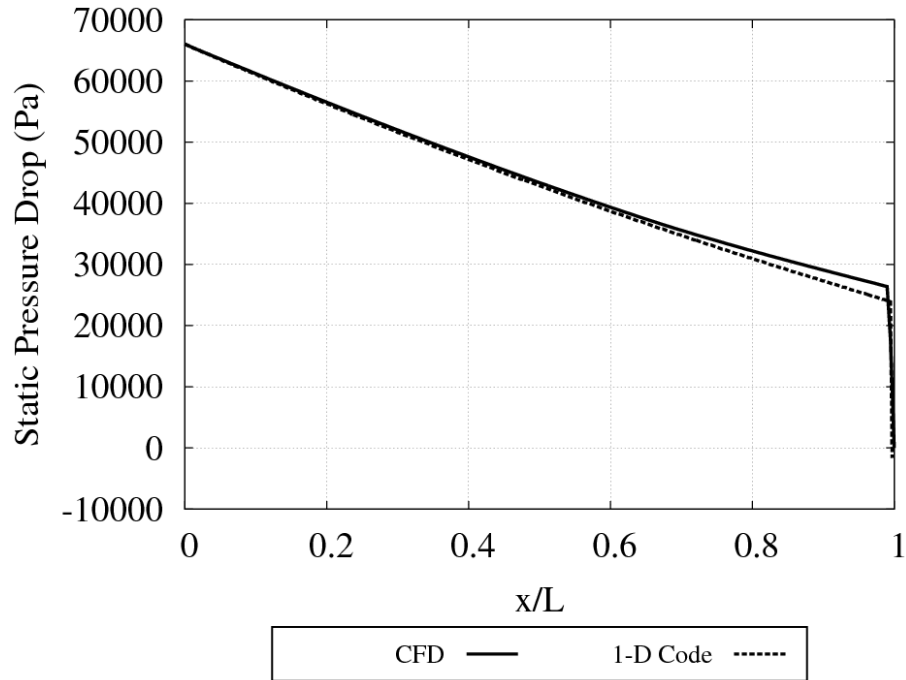


Figure 6.8: Axial static pressure drop using 1-D code and the SST model for Case S1 ( $\dot{m} = 0.058 \text{ kg/s}$ )

### 6.3.3 Assessing Ledinegg’s and Chatoorgoon’s Conditions for Approximating the Static Instability Threshold

As mentioned earlier, a significant number of steady-state and transient runs should be performed to find the instability threshold for a particular case and that requires a significant amount of computational cost. However, knowing the approximate location of the instability threshold, fewer runs may be needed to find the exact instability threshold. Ledinegg (1938) and Chatoorgoon (2013) have proposed conditions that make it possible to find the approximate threshold of static instability without a need to perform transient analyses. Ledinegg (1938) suggested that two-phase flow instability occurs when the slope of the channel pressure drop versus mass flow rate curve is negative and steeper than the loop supply pressure-drop versus flow rate curve, which corresponds to the

minimum of channel static pressure drop ( $\Delta p$ ) versus mass flow rate plot. However, whether this condition applies to the supercritical flow is examined in this study. Chatoorgoon (2013) suggested that the minimum of  $\Delta(p + \rho u^2)$  versus mass flow rate plot lies close to the static instability boundary for conditions with plena. It is noteworthy that in this study, his condition is tested without inlet and outlet plena. The plots in Figure 6.9 are the channel  $\Delta(p + \rho u^2)$  and the channel  $\Delta p$  versus mass flow rate for the CFD code, using the  $k-\varepsilon$  and the SST models and the 1-D code, for Case S1. Then, the instability boundary point of the  $k-\varepsilon$  and the SST models and 1-D code are inserted into the curves of Figure 6.9.

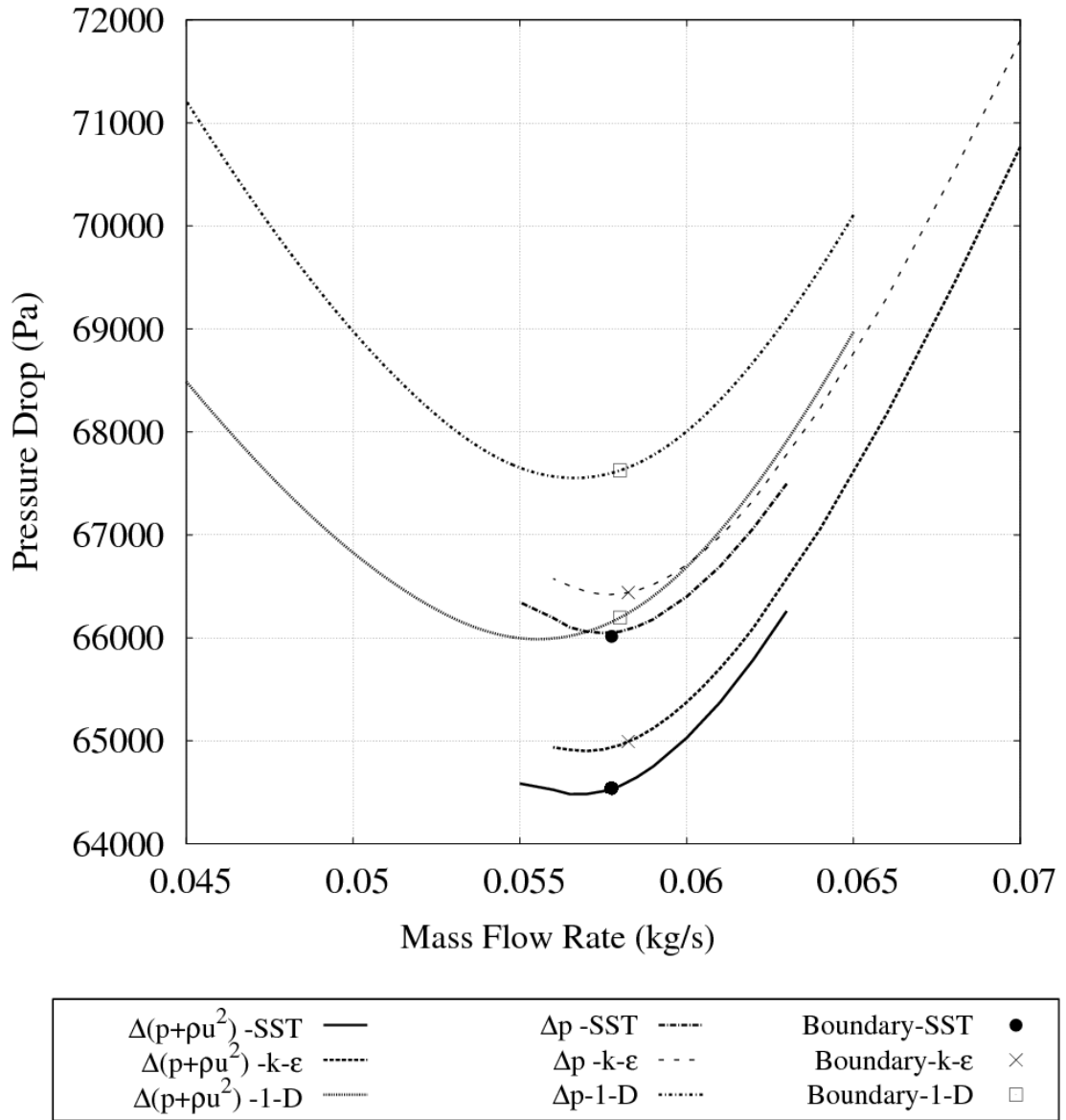


Figure 6.9: Instability boundary and  $\Delta(p + \rho u^2)$  and  $\Delta p$  of the channel versus mass flow rate using the  $k-\varepsilon$  and the SST models and 1-D code for Case S1

To see the pressure drops and instability boundary predicted by each model in more detail, the channel  $\Delta(p + \rho u^2)$  and  $\Delta p$  with respect to mass flow rate as well as the instability threshold predicted are shown in Figures 6.10, 6.11 and 6.12 for the  $k-\varepsilon$  model, the SST model, and the 1-D code, respectively. As these figures show, the value of

$\Delta(p + \rho u^2)$  is always lower than  $\Delta p$ . This is because  $\rho u^2$  is higher at the outlet than the inlet, since the velocity is higher at the outlet.

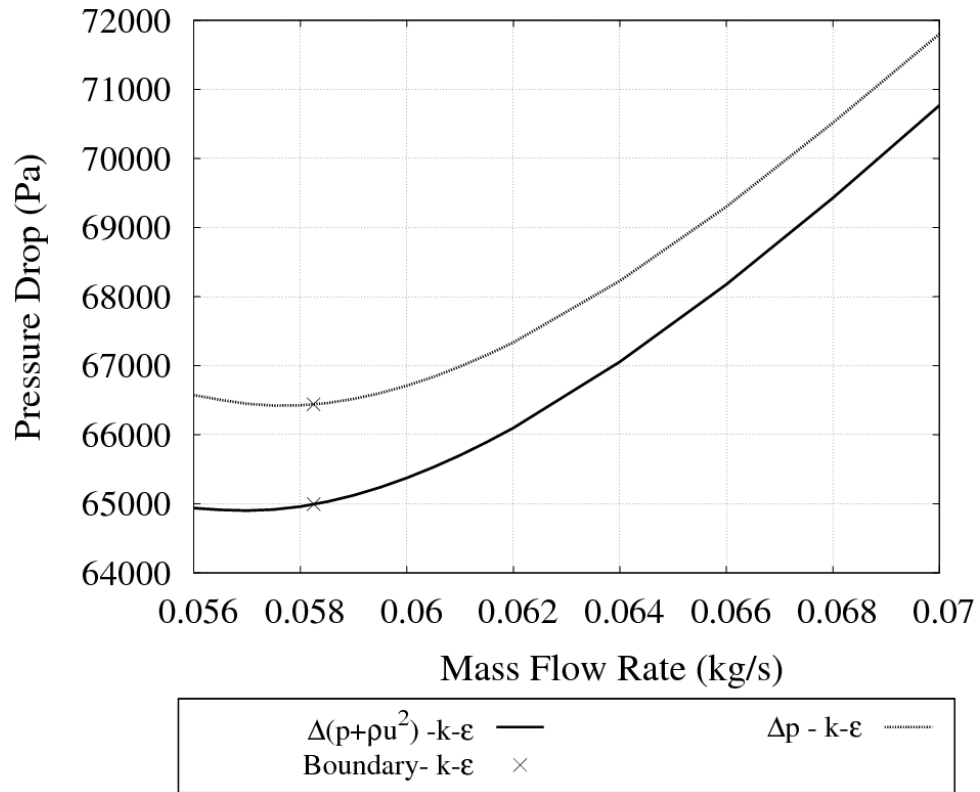


Figure 6.10: Instability boundary and  $\Delta(p + \rho u^2)$  and  $\Delta p$  of the channel versus mass flow rate using the  $k-\epsilon$  model for Case S1

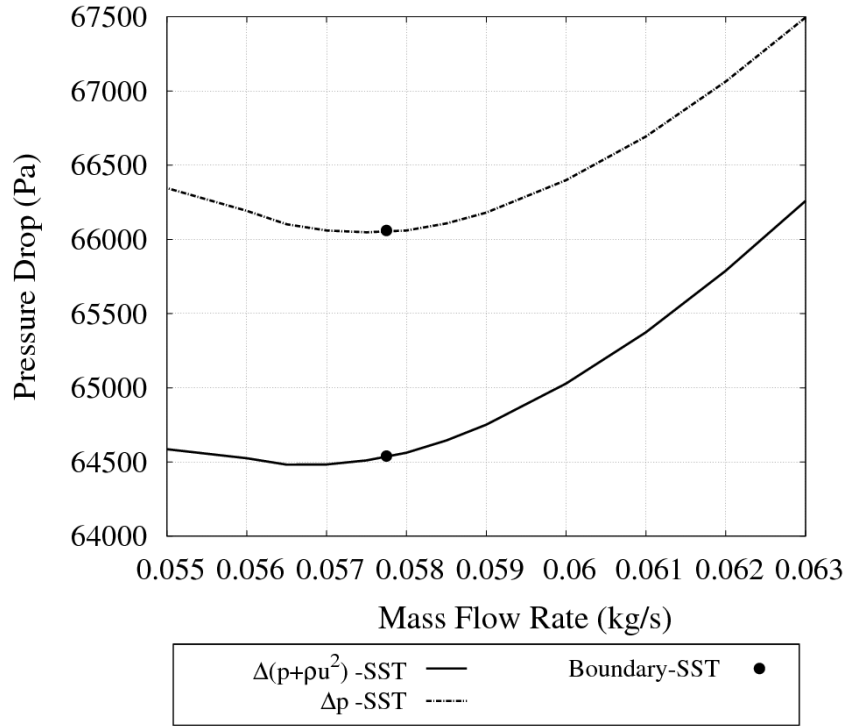


Figure 6.11: Instability boundary and  $\Delta(p + \rho u^2)$  and  $\Delta p$  of the channel versus mass flow rate using the SST model for Case S1

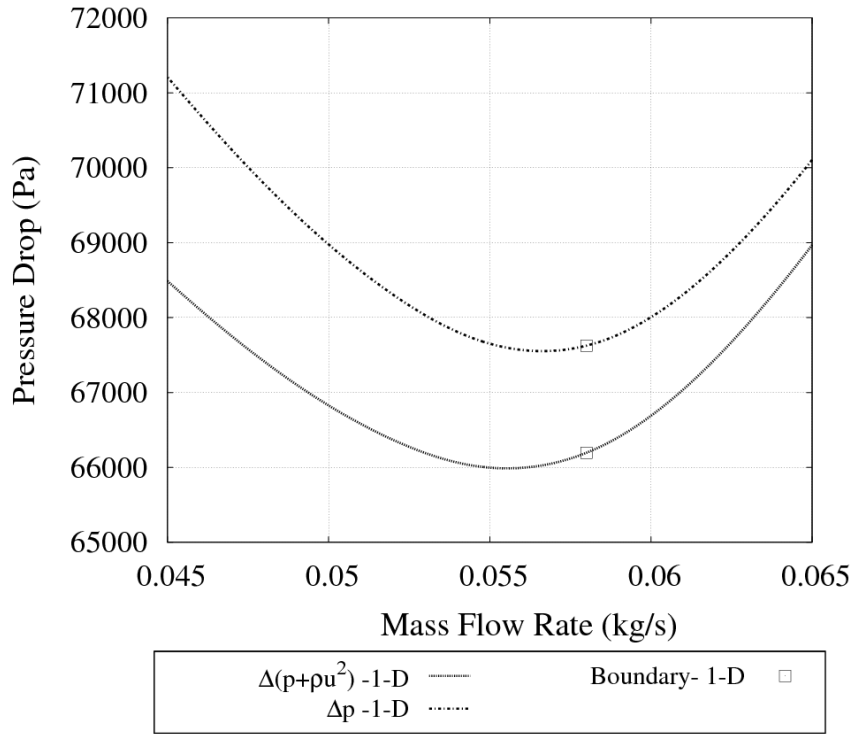


Figure 6.12: Instability boundary and  $\Delta(p + \rho u^2)$  and  $\Delta p$  of the channel versus mass flow rate using the 1-D code for Case S1

Table 6.5 summarizes the results of CFD corresponding to the static instability thresholds and Chatoorgoon’s and Ledinegg’s criteria for the static instability using the  $k-\varepsilon$  and the SST models. As discussed in Chapter 3, the IAPWS property package that was used by CFX v.14.5 had a limited range of validity. For pressures more than 10 MPa, and less than 100 MPa, the temperature should be less than 800°C (1073 K). Therefore, an attempt was made to keep the temperature and pressure of all cases in the range of validity of IAPWS, to ensure the results are correct. In low mass flow rate cases where the outlet temperature is high and specially in cases where heat transfer deterioration occurs, there is a risk that the temperature exceeds 800°C. Among the cases examined for static instability, the minimum of the  $\Delta(p + \rho u^2)$  curve for Case S2, using the SST model could not be obtained, as the temperature exceeded the validity limit of IAPWS. However, the minimum of the  $\Delta p$  curve and the instability threshold were obtained for this case. As Table 6.5 suggests, for all the cases used in this study, the minimum of  $\Delta(p + \rho u^2)$  happens at an equal or a lower mass flow rate than the minimum of  $\Delta p$ .

Table 6.5: CFD mass flow rate predictions corresponding to Chatoorgoon’s and Ledinegg’s criteria for static instability

Case	Instability Threshold Mass Flow Rate (k/s)		Mass Flow Rate at $\partial \Delta(p + \rho u^2)/\partial \dot{m} = 0$ (kg/s)		Mass Flow Rate at $\partial (\Delta p)/\partial \dot{m} = 0$ (kg/s)	
	$k-\varepsilon$	SST	$k-\varepsilon$	SST	$k-\varepsilon$	SST
<b>S1</b>	0.0585	0.058	0.057	0.0565	0.0575	0.0575
<b>S2</b>	0.053	0.0525	0.049	Property Table limit reached	0.0525	0.0525
<b>S3</b>	0.0625	0.0615	0.061	0.06	0.0625	0.062
<b>S4</b>	0.0565	0.061	0.0515	0.054	0.0555	0.0595

Table 6.6 summarizes the results of the 1-D code corresponding to instability thresholds and Chatoorgoon's and Ledinegg's criteria for static instability. Like the CFD code, for 1-D code also, the minimum of  $\Delta(p + \rho u^2)$  happens at an equal or a lower mass flow rate than the minimum of  $\Delta p$  in all of the cases.

Table 6.6: 1-D code mass flow rate predictions corresponding to Chatoorgoon's and Ledinegg's criteria for static instability

Case	Instability Threshold Mass Flow Rate at (kg/s)	Mass Flow Rate at $\partial \Delta(p + \rho u^2)/\partial \dot{m} = 0$ (kg/s)	Mass Flow Rate at $\partial (\Delta p)/\partial \dot{m} = 0$ (kg/s)
S1	0.058	0.0555	0.0566
S2	0.056	0.0529	0.055
S3	0.063	0.061	0.0625
S4	0.061	0.0568	0.0604

Table 6.7 summarizes the comparison of results of 1-D and CFD codes corresponding to Chatoorgoon's and Ledinegg's criteria for static instability with the instability thresholds obtained using each model. The maximum difference between the mass flow rate at the instability threshold and the mass flow rate corresponding to  $\partial \Delta(p + \rho u^2)/\partial \dot{m} = 0$  happens in Case S4 using the SST model and is equal to 11.5%. While the maximum difference between the mass flow rate at the instability threshold and the mass flow rate corresponding to  $\partial \Delta(p)/\partial \dot{m} = 0$  happens in Case S4 using the SST model and is equal to 2.46 %. For other cases the difference is insignificant. A reason for this disagreement is the fact that the values of mass flow rates used in this study are very low, and a small difference in mass flow rate at the instability threshold results in a large percentage difference. To prove that, Case S4 with the maximum difference between mass flow rate

instability threshold of CFD and mass flow rate corresponding to Chatoorgoon's condition ( $\partial \Delta(p + \rho u^2)/\partial \dot{m} = 0$ ) was examined with doubled, i.e. 200 kW. Using this power, the percentage difference of mass flow rate at the instability boundary between Chatoorgoon's condition and the CFD codes is 3%. For this case, the percentage difference of mass flow rate at the instability boundary between Ledinegg's condition and the CFD codes is negligible. Hence, approximating the flow instability threshold by the minimum of the  $\Delta(p + \rho u^2)$  versus mass flow rate curve and the minimum of  $\Delta p$  versus mass flow rate curve holds true for a CFD solution. Although, Ledinegg's criterion agrees better with the CFD and 1-D non-linear results (when there are no inlet and outlet plena). This finding has to be re-examined with CFD when the inlet-outlet plena are added to the geometry.

Table 6.7: Differences in CFD and 1-D mass flow rate predictions corresponding to Chatoorgoon's and Ledinegg's criteria for static instability and the instability thresholds

Case	Difference in Mass Flow Rate at the Instability Threshold and at $\partial \Delta(p + \rho u^2)/\partial \dot{m} = 0$ (%)			Difference in Mass Flow Rate at the Instability Threshold and at $\partial (\Delta p)/\partial \dot{m} = 0$ (%)		
	1-D	$k-\varepsilon$	SST	1-D	$k-\varepsilon$	SST
<b>S1</b>	4.3	2.56	2.58	2.4	1.71	0.86
<b>S2</b>	5.53	7.54	Property Table limit reached	1.78	0.94	0
<b>S3</b>	3.17	2.4	2.44	0.8	0	0.81
<b>S4</b>	6.88	8.85	11.5	0.98	1.77	2.46

#### 6.3.4 CFX Oscillatory Instability Results

To study the oscillatory instability, four cases shown in Table 6.2 were modeled. Among these cases, Case O1 has a zero K factor and, therefore, the instability boundary happens at a lower mass flow rate compared to Case O2 (the effect of K factor on the instability threshold is discussed in Section 6.5). This case also has a small inlet temperature and the instability threshold happens at a lower mass flow rate compared to Case O3. From the preliminary analyses, the instability boundary for Case O1 could not be obtained as the wall temperature exceeded 800°C. One of the parameters which affect the wall temperature is the  $Pr_t$ , where decreasing the  $Pr_t$ , reduces the wall temperature (as Shown in Figures 5.17 and 5.20). Therefore, to move forward with Case O1, this case was simulated using  $Pr_t$  equal to 0.7. Other cases shown in Table 6.2 are simulated using  $Pr_t$  equal to 0.95. The effect of  $Pr_t$  on the instability threshold is discussed in Section 6.5.

Figure 6.13 shows the inlet mass flow rate time response predicted by the CFD code for an initial mass flow rate of 0.067 kg/s, an inlet temperature of 350°C and a power of 100 kW (Case O3), using the  $k-\varepsilon$  model. The amplitude of oscillations diminishes with time, indicating a stable system. Figure 6.14 shows the CFD response when the initial mass flow rate was 0.0665 kg/s. The system is unstable. The oscillation period for this case is 1.8 s. Thus, the instability threshold predicted by the CFD code is between 0.0665 kg/s and 0.067 kg/s. As in the cases of static instability, here also the higher values of instability boundary ranges are reported, to assure the safety of the system.

For the instability boundary of Case O3, variations of inlet and outlet mass flow rates obtained using the  $k-\varepsilon$  model are shown in Figure 6.15 during time. Inlet and outlet mass flow rates oscillate out-of-phase to keep the mass flow rate constant along the pipe.

Table 6.8 summarizes the oscillatory instability threshold and period of oscillation results for the cases shown in Table 6.2, using the  $k-\varepsilon$  and the SST turbulence models.

It is worth noting that in this study the disturbance employed on the flow arose from changing the boundary conditions from the steady-state solution to the transient solution and no actual disturbance was introduced. To see whether this disturbance was large enough to shift the instability boundary, one oscillatory instability case (O1) and one static instability case (S4) were re-examined by introducing a large disturbance in the transient simulation. This perturbation was employed by introducing a higher pressure drop (which was associated with a mass flow rate 1% higher than the original mass flow rate) for the first 1 s of the transient simulation. Results showed that the uncertainty of the instability thresholds for the two cases examined is less than 4%.

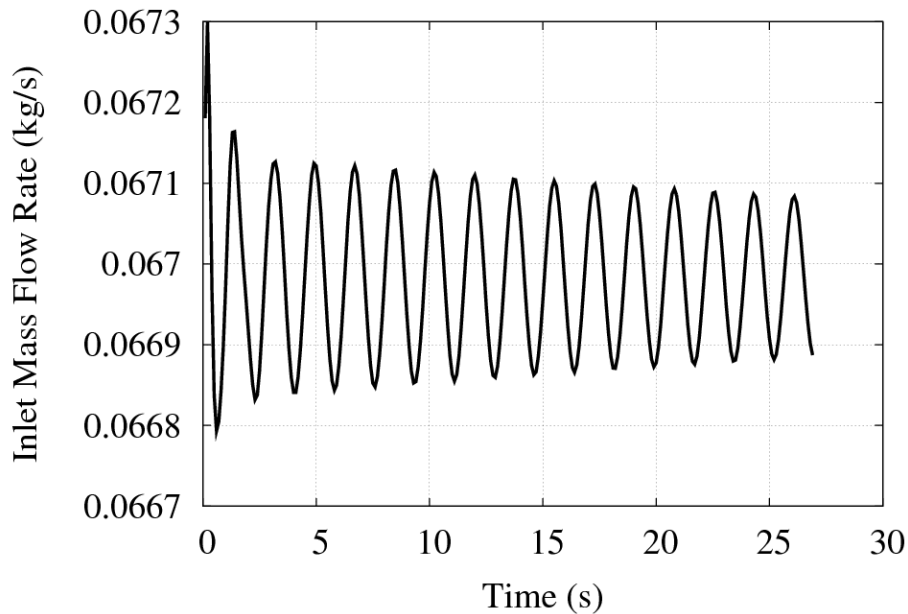


Figure 6.13: CFD results for a stable case, using the  $k-\varepsilon$  model for Case O3 ( $\dot{m} = 0.067$  kg/s)

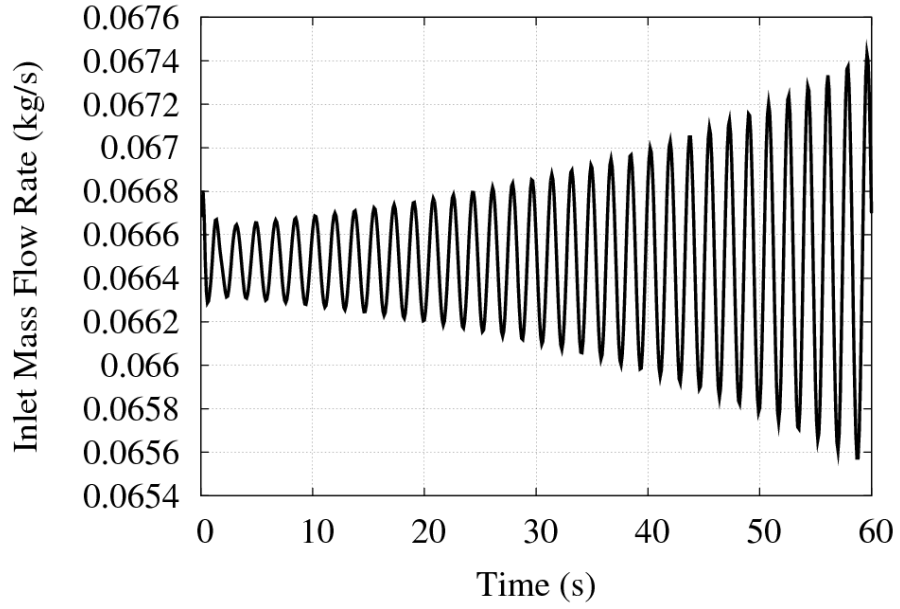


Figure 6.14: CFD results for an unstable case using the  $k-\varepsilon$  model for Case O3 ( $\dot{m} = 0.0665 \text{ kg/s}$ )

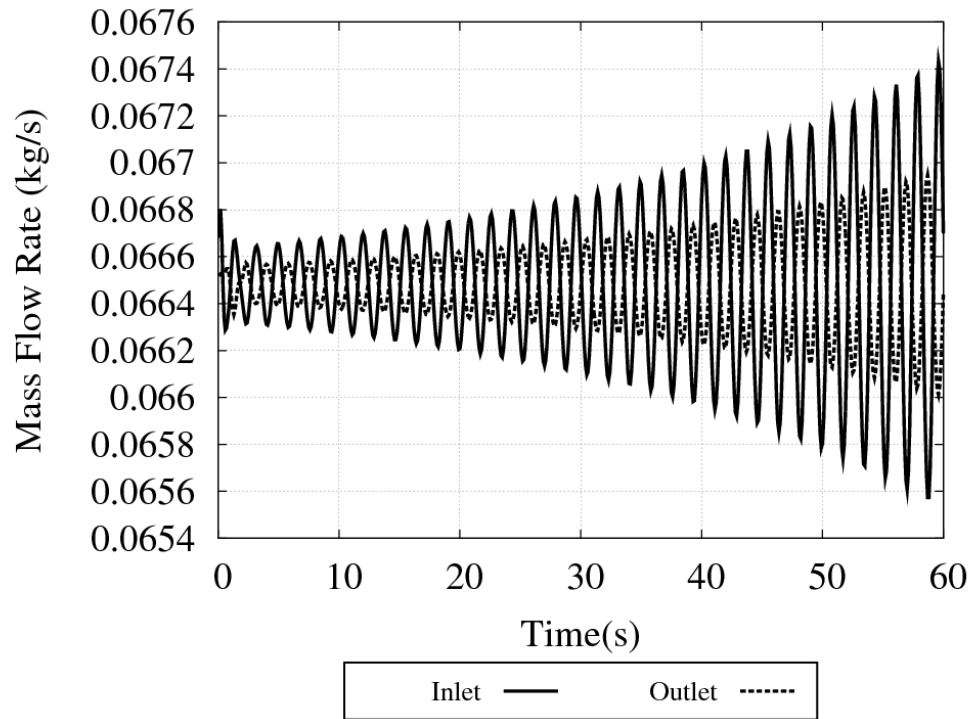


Figure 6.15: Variation of inlet and outlet mass flow rates with time for Case O3 ( $\dot{m} = 0.0665 \text{ kg/s}$ )

Table 6.8: Oscillatory instability threshold mass flow rates and period of oscillation predicted by CFD

Case	CFD Instability Threshold Mass Flow Rate (kg/s)		Period of Oscillation (s)		Difference of Instability Threshold- SST and $k-\varepsilon$ models (%)
	$k-\varepsilon$ model	SST model	$k-\varepsilon$ model	SST model	
<b>O1</b>	0.052	0.053	3.5	3.74	1.9
<b>O2</b>	0.0705	0.0695	5.2	5.48	1.44
<b>O3</b>	0.067	0.067	1.8	1.81	0
<b>O4</b>	0.086	0.09	1.9	1.76	4.44

Table 6.8 suggests that the results of instability thresholds between the  $k-\varepsilon$  and the SST models are close and the largest difference, that appears in Case O4, is 4.44%.

Figure 6.16 shows the comparison of wall temperature between the  $k-\varepsilon$  and the SST models for Case O4 at the mass flow rate of 0.086 kg/s. There is a maximum of about 20 K difference between the two models and the  $k-\varepsilon$  model predicts a much lower wall temperature.

Figure 6.17 shows the comparison of static pressure drop between the  $k-\varepsilon$  and the SST models for Case O4 at a mass flow rate close to the instability boundary. In this case, the lower resolution of the  $k-\varepsilon$  model in predicting the near-wall behavior of the flow has a small effect on the axial pressure drop. Also, a significant amount of pressure drop is caused by the outlet K factor, which is not greatly affected by the turbulence model used.

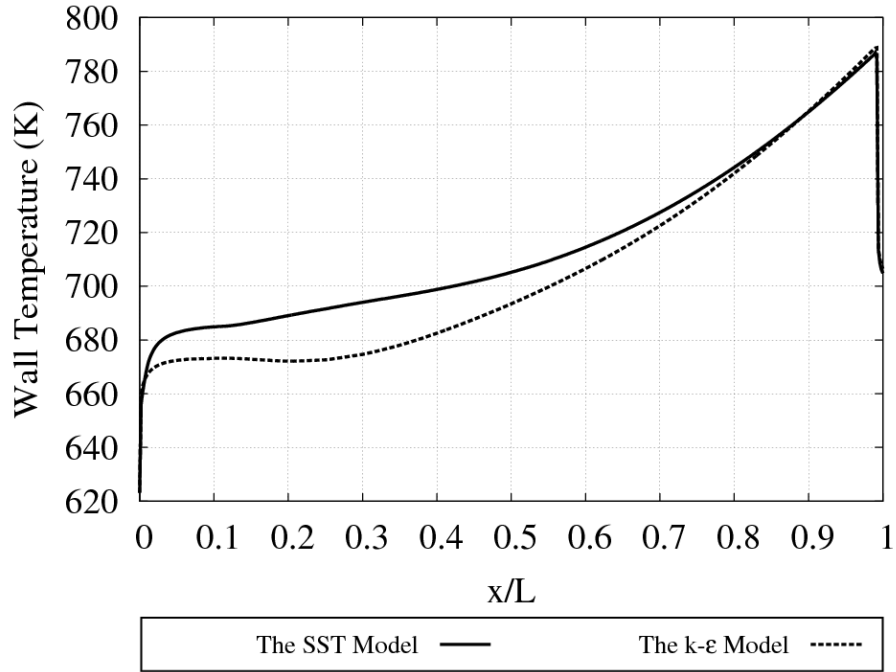


Figure 6.16: Axial wall temperature of the  $k-\epsilon$  and the SST models for Case O4 ( $\dot{m} = 0.086 \text{ kg/s}$ )

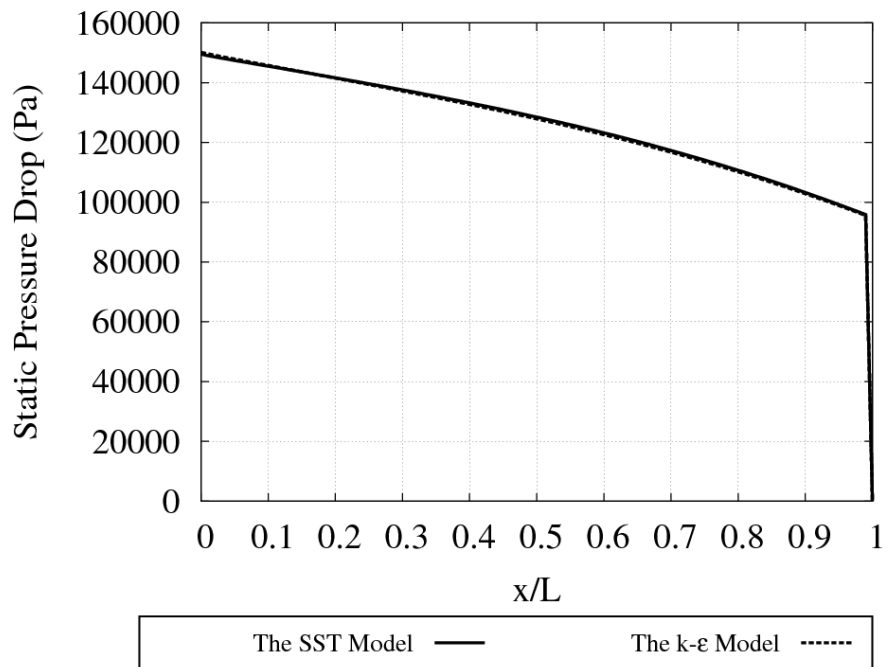


Figure 6.17: Axial pressure drop of the  $k-\epsilon$  and the SST models for Case O4 ( $\dot{m} = 0.086 \text{ kg/s}$ )

To determine the pressure drop component that causes the difference in the static pressure drop between the  $k-\varepsilon$  and SST models, the variations of different terms of Equation (6.1) with the non-dimensional length of the pipe are examined for Case O4 using the  $k-\varepsilon$  and the SST turbulence models for the region before the K factor. Like Case S4, in this case also the hydrostatic term stays the same for both turbulence models. The RMS differences of gravitational and acceleration pressure drops between the two models are 0.0001 N/m (0.05% of the averaged magnitude along the pipe) and 0.0022 N/m (1.1% of the averaged magnitude along the pipe), respectively. Other terms of Equation (6.1) are shown in Figure 6.18. This figure shows that the friction force gradient caused by the frictional pressure drop is the main component that is different between the two turbulence models and it causes the difference in the static pressure drop.

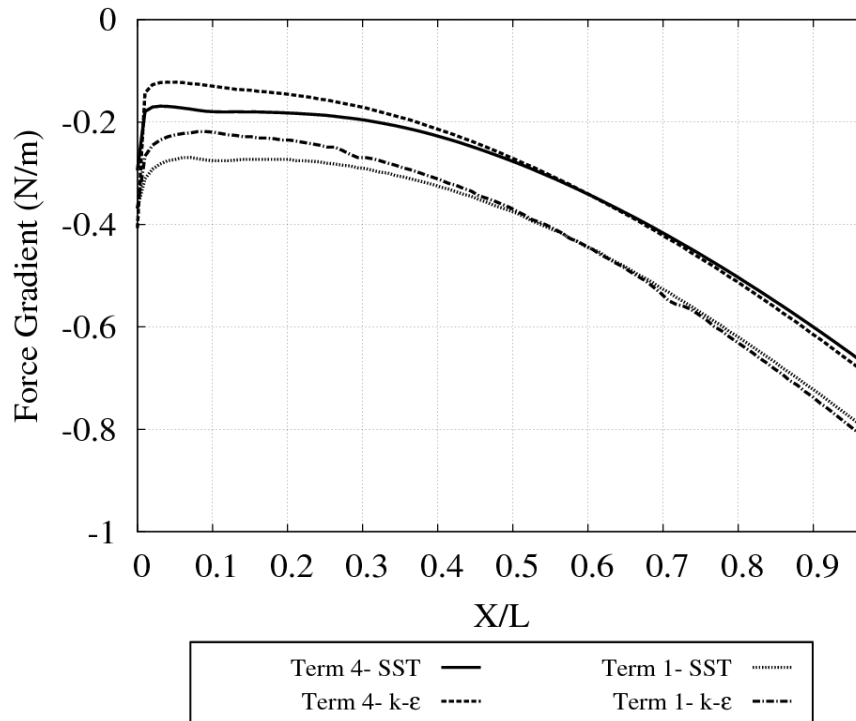


Figure 6.18: Variations of Term 1 and Term 4 in Equation (6.1) vs. the non-dimensional length of the pipe using the  $k-\varepsilon$  and the SST models for Case O4 ( $\dot{m} = 0.086$  kg/s)

### 6.3.5 Comparison of CFX Results with 1-D Non-Linear Results for Oscillatory Instability

The 1-D non-linear code simulations are shown in Figures 6.19 and 6.20, for an inlet temperature of 350°C and power of 100 kW (Case O3). Figure 6.19 shows a stable response for an initial flow rate of 0.058 kg/s, while Figure 6.20 shows an unstable response for an initial flow rate of 0.057 kg/s. Thus, for this case, the 1-D solution predictions are approximately 14% lower than those of the CFD solutions. The period of oscillation obtained using the 1-D code is 1.82 s for this case.

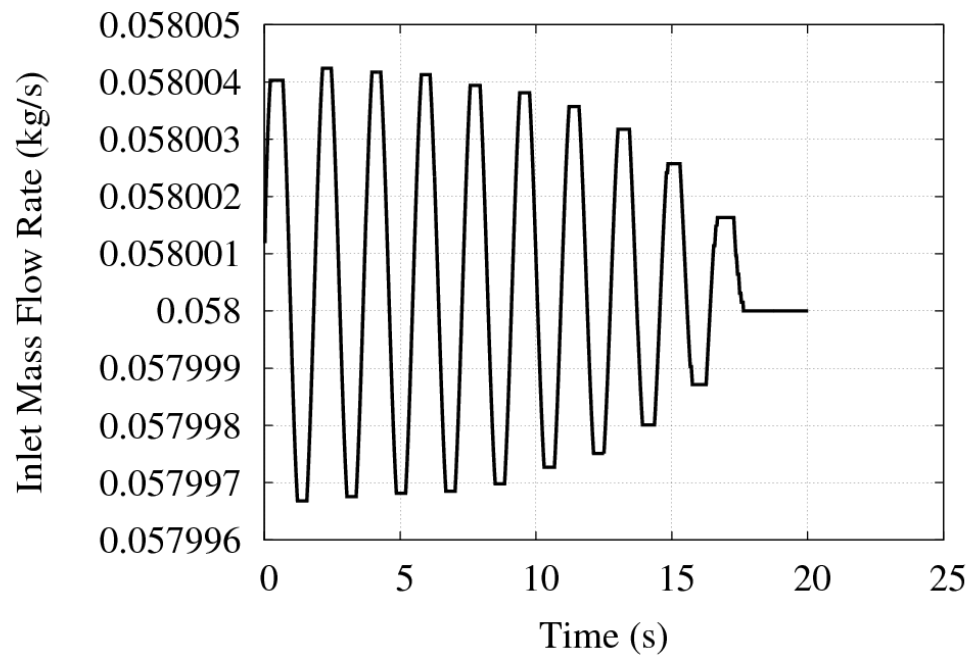


Figure 6.19: 1-D non-linear (SPORTS) results for a stable case for Case O3 ( $\dot{m} = 0.058$  kg/s)

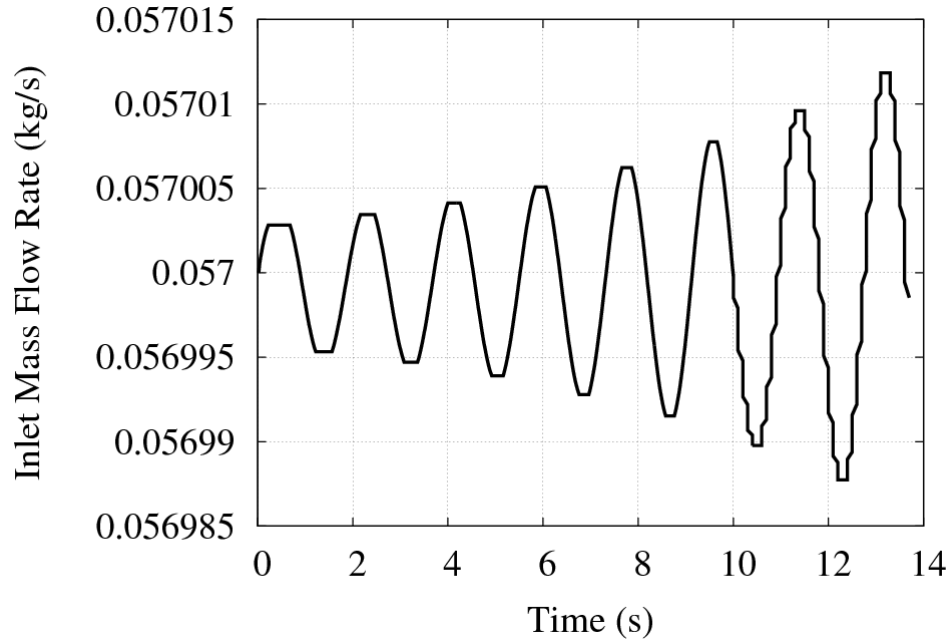


Figure 6.20: 1-D non-linear (SPORTS) results for an unstable case for Case O3 ( $\dot{m} = 0.057 \text{ kg/s}$ )

Table 6.9 summarizes the results of instability analyses using the 1-D non-linear code and the comparison of results with the CFX results obtained using the  $k-\epsilon$  and the SST turbulence models. The maximum difference of CFD and 1-D instability threshold is for Case O1, using the SST model. Overall, for the cases analyzed in this study, the differences between the 1-D instability thresholds and the CFD thresholds are more significant in the oscillatory instability than the static instability. One of the reasons for that is the lower K factors used in the oscillatory instability cases. For the cases of high K factors, the system pressure drop is dominated by the K factors and, therefore, the difference in pressure drop predictions between 1-D and CFD codes is less significant. However, there is good agreement on the period of oscillations between CFD and 1-D non-linear codes (compare Tables 6.8 and 6.9).

Table 6.9: Oscillatory instability threshold predicted by 1-D code and comparison with the CFD results

<b>Case</b>	<b>1-D Non-Linear Instability Threshold Mass Flow Rate (kg/s)</b>	<b>Period of Oscillation 1-D (s)</b>	<b>Difference of Instability Threshold <math>k</math>-<math>\epsilon</math> model and 1-D Non-Linear Code (%)</b>	<b>Difference of Instability Threshold SST model and 1-D Non-Linear Code (%)</b>
<b>O1</b>	0.0415	3.8	20.19	21.70
<b>O2</b>	0.065	5.73	7.8	6.47
<b>O3</b>	0.0575	1.82	14.18	14.18
<b>O4</b>	0.081	1.81	5.81	10

Figure 6.21 shows the variation of static pressure for 1-D and CFD codes for Case O1 and mass flow rate of 0.052 kg/s. The pressure drop predictions between these two codes are very different. The reasons for the difference between CFD and 1-D results were discussed in section 6.3.2.

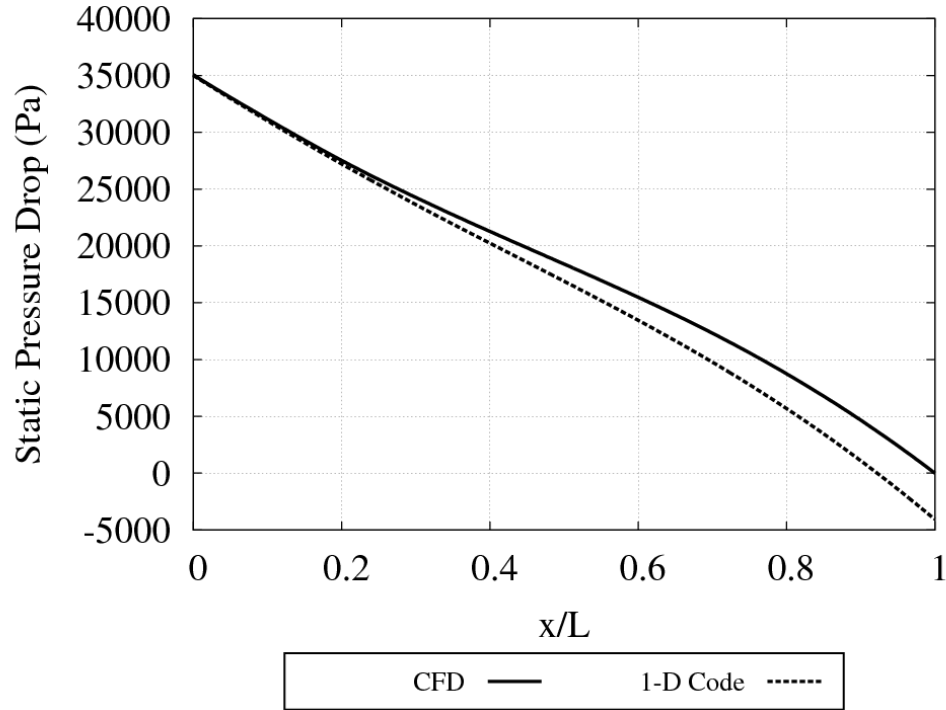


Figure 6.21: Axial static pressure for 1-D code and the SST model for Case O1 ( $\dot{m} = 0.052 \text{ kg/s}$ )

### 6.3.6 Assessing Chatoorgoon's Condition for Approximating the Oscillatory Instability Threshold

The  $\partial\Delta(p + \rho u^2)/\partial\dot{m}$  plot is deemed important by Chatoorgoon (2006), as he suggested that the minimum of that profile lies close to the oscillatory instability boundary. Figure 6.22 shows the channel  $\Delta(p + \rho u^2)$  for the CFD code using the  $k-\varepsilon$  and the SST models and 1-D code for Case O3. This figure shows that the channel  $\Delta(p + \rho u^2)$  is very different between the CFD and 1-D codes (about 25%) due to different methods used for determining the pressure drop. This was discussed in section 6.3.2.

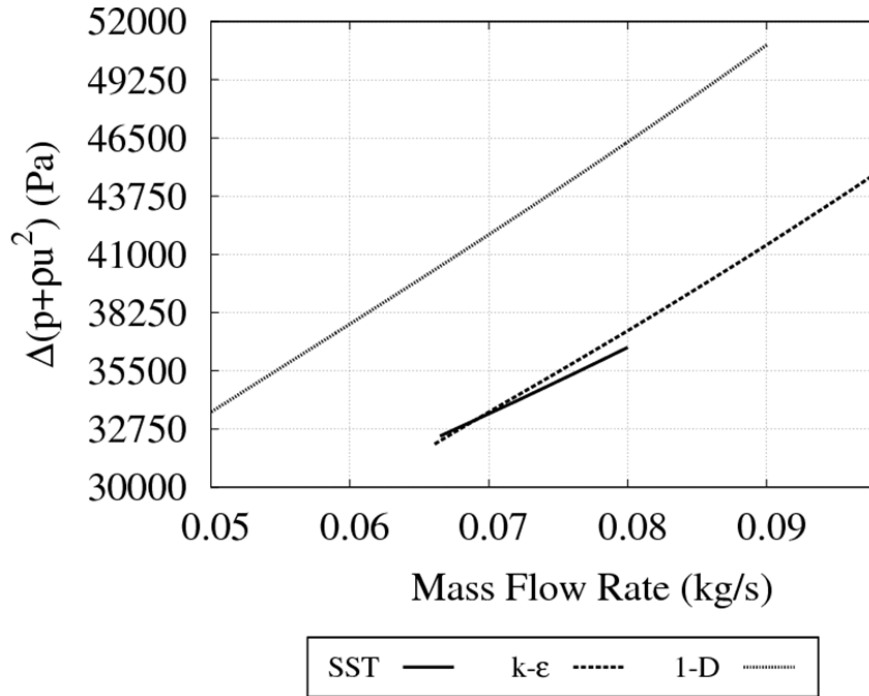


Figure 6.22:  $\Delta(p + \rho u^2)$  of the channel versus mass flow rate using CFD and 1-D codes for Case O3

Figure 6.23 shows the variation of  $\Delta(p + \rho u^2)$  and  $\partial \Delta(p + \rho u^2) / \partial \dot{m}$  with mass flow rate for the CFD code using the  $k-\epsilon$  and the SST models. Also shown are the instability boundary points of the  $k-\epsilon$  and the SST models. This figure shows that, although the instability thresholds obtained using the  $k-\epsilon$  and the SST models are close to each other in value, the minimum of  $\partial \Delta(p + \rho u^2) / \partial \dot{m}$  is different between the two models. For this case, the SST model shows a 2.43% difference between the instability threshold and the minimum of  $\partial \Delta(p + \rho u^2) / \partial \dot{m}$ , while for the  $k-\epsilon$  model, the difference is about 6.71%.

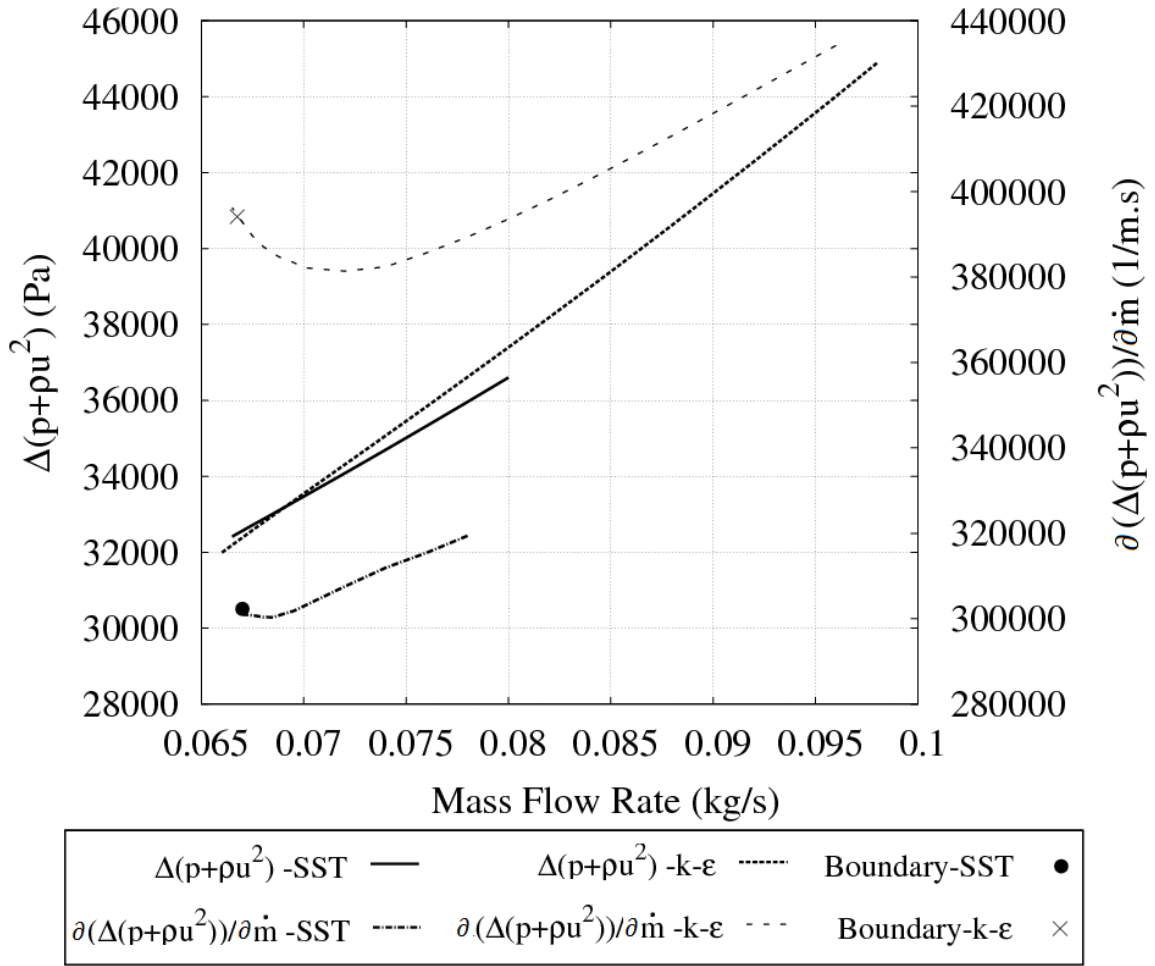


Figure 6.23: Instability boundary,  $\Delta(p + \rho u^2)$  of the channel, and  $\partial \Delta(p + \rho u^2)/\partial \dot{m}$ , using CFD for Case O3

To see the pressure drops and instability boundary predicted by each model in more detail, the variation of  $\Delta(p + \rho u^2)$  and  $\partial \Delta(p + \rho u^2)/\partial \dot{m}$  with respect to mass flow rate as well as the instability threshold predicted are shown in Figures 6.24, 6.25, and 6.26 for the  $k-\epsilon$  model, the SST model, and the 1-D code, respectively, for Case O3. For this case, the 1-D code also shows good agreement between the instability threshold and the minimum of  $\partial \Delta(p + \rho u^2)/\partial \dot{m}$ .

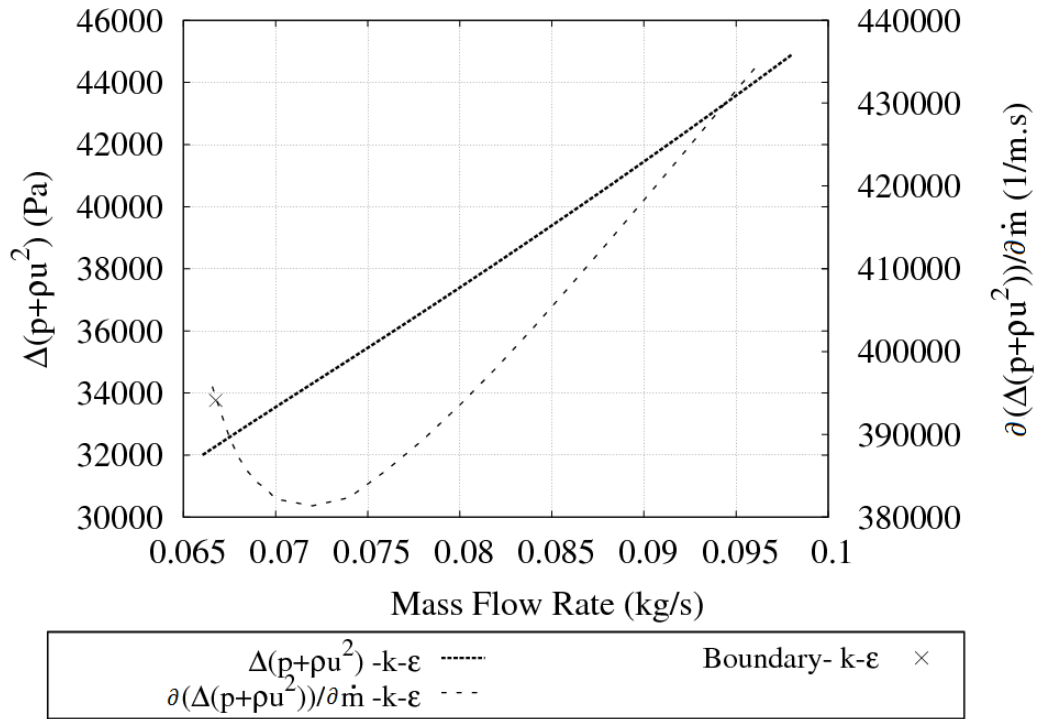


Figure 6.24: Instability boundary,  $\Delta(p + \rho u^2)$  of the channel, and  $\partial \Delta(p + \rho u^2) / \partial \dot{m}$ , using the  $k-\epsilon$  model for Case O3

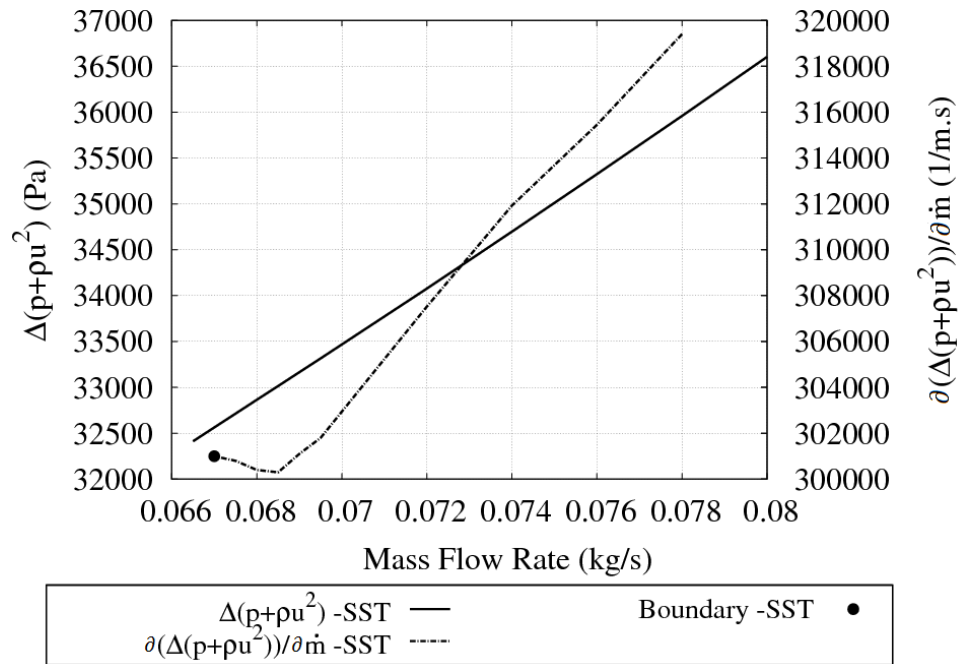


Figure 6.25: Instability boundary,  $\Delta(p + \rho u^2)$  of the channel, and  $\partial \Delta(p + \rho u^2) / \partial \dot{m}$ , using the SST model for Case O3

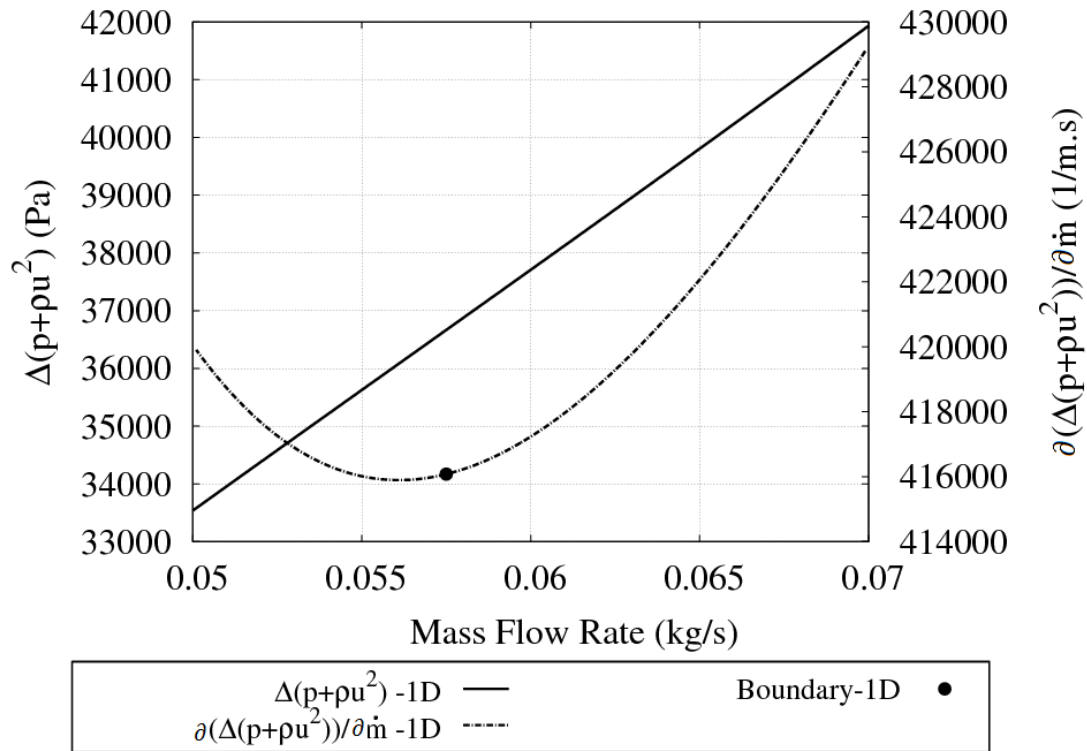


Figure 6.26: Instability boundary,  $\Delta(p + \rho u^2)$  of the channel, and  $\partial \Delta(p + \rho u^2)/\partial \dot{m}$ , using the 1-D code for Case O3

Table 6.10 summarizes the results of the CFD and 1-D codes corresponding to Chatoorgoon's criteria for oscillatory instability as well as the instability thresholds obtained using the  $k-\varepsilon$  and the SST models and the 1-D code. For the oscillatory instability cases, the 1-D non-linear code with the Blasius friction factor formula always predicts a higher static pressure drop and, therefore, predicts a lower mass flow rate at the oscillatory instability threshold compared to the CFD code.

Table 6.10: CFD and 1-D mass flow rates corresponding to Chatoorgoon's criteria for oscillatory instability and comparison with the instability threshold

Case	Instability Threshold Mass Flow Rate (kg/s)			Mass Flow Rate at $\partial^2\Delta(p + \rho u^2)/\partial\dot{m}^2 = 0$		
	1-D	$k-\varepsilon$	SST	1-D	$k-\varepsilon$	SST
<b>O1</b>	0.0415	0.052	0.053	0.046	0.059	0.053
<b>O2</b>	0.065	0.0705	0.0695	0.0685	0.071	0.07
<b>O3</b>	0.0575	0.067	0.067	0.0561	0.0715	0.0685
<b>O4</b>	0.081	0.086	0.09	0.0823	0.086	0.0865

Table 6.11 shows the percentage difference of the results corresponding to Chatoorgoon's criterion and the instability thresholds obtained using transient analyses for the  $k-\varepsilon$  and the SST models and 1-D code. The maximum difference between the mass flow rate at the instability threshold of CFD and the mass flow rate corresponding to  $\partial^2\Delta(p + \rho u^2)/\partial\dot{m}^2 = 0$  happens in Case O1 using the  $k-\varepsilon$  model and for other cases the difference is insignificant. Hence, approximating the flow instability threshold by the minimum of the  $\partial\Delta(p + \rho u^2)/\partial\dot{m}$  curve seems to hold true for CFD solutions. The maximum difference between the mass flow rate at the instability threshold and the mass flow rate corresponding to  $\partial^2\Delta(p + \rho u^2)/\partial\dot{m}^2 = 0$  using the 1-D code also happens in Case O1.

Table 6.11: Comparison of CFD and 1-D results corresponding to Chatoorgoon's criterion for oscillatory instability with the instability thresholds

Case	Difference of Instability Threshold Mass Flow Rate and Mass Flow Rate at $\partial^2\Delta(p + \rho u^2)/\partial \dot{m}^2 = 0$ (%)		
	1-D	$k-\varepsilon$	SST
<b>O1</b>	10.84	13.46	0
<b>O2</b>	5.38	0.71	0.71
<b>O3</b>	2.43	6.71	2.23
<b>O4</b>	1.6	0	3.9

#### 6.4 Summary of Static and Oscillatory Instabilities Results

Figures 6.27, 6.28, and 6.29 summarize the results of ratio of mass flow rate at the instability boundary to the mass flow rate at the conditions specified for static and oscillatory instabilities, for the CFD and 1-D codes. These figures show that these ratios are between 0.9 and 1.1 for most of the cases.

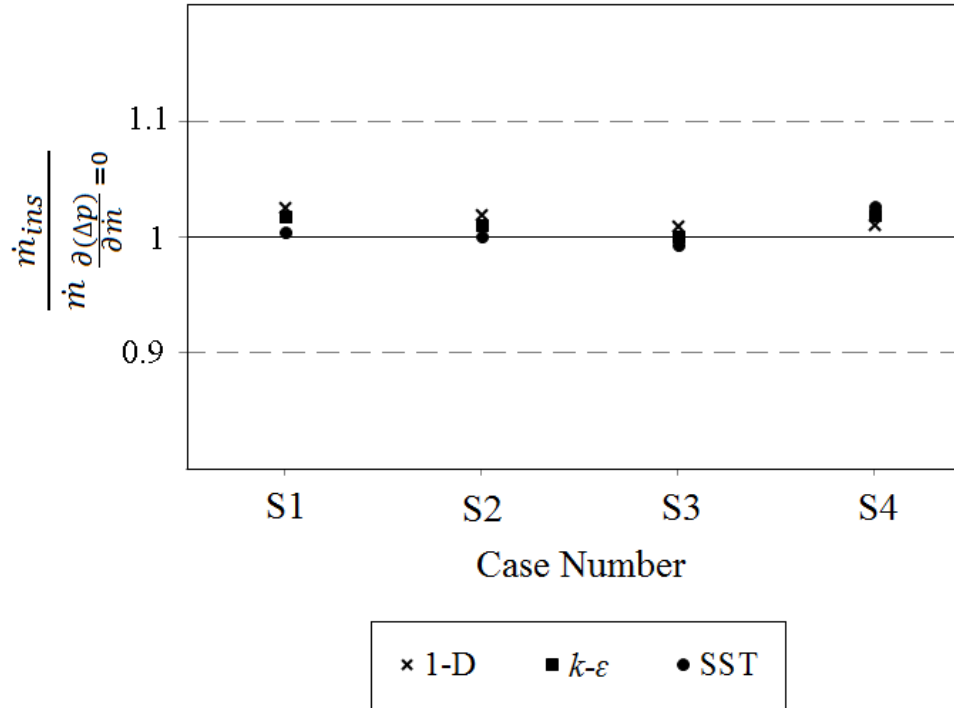


Figure 6.27: Ratio of mass flow rate at the instability boundary to the mass flow rate at  $\partial(\Delta p)/\partial\dot{m} = 0$  for static instability cases using CFD and 1-D codes

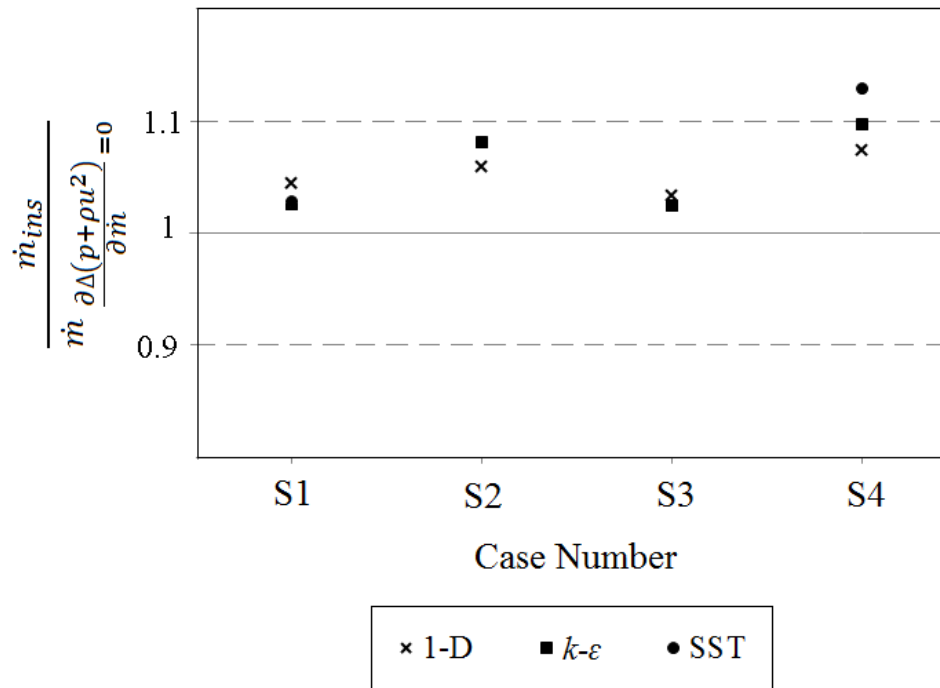


Figure 6.28: Ratio of mass flow rate at the instability boundary to the mass flow rate at  $\partial\Delta(p + \rho u^2)/\partial\dot{m} = 0$  for static instability cases using CFD and 1-D codes

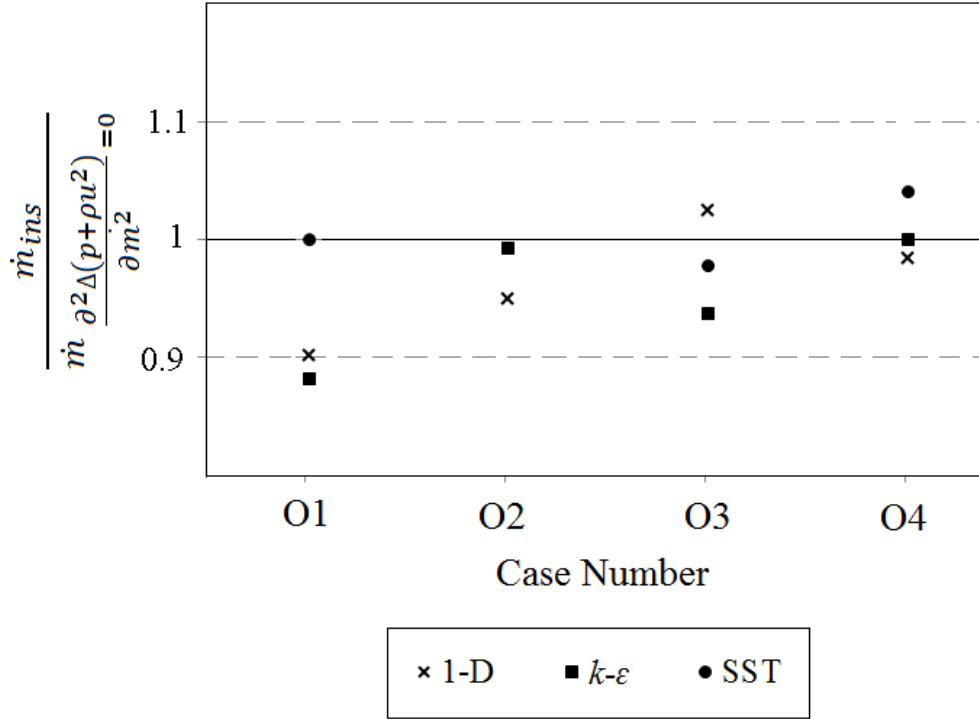


Figure 6.29: Ratio of mass flow rate at the instability boundary to the mass flow rate at  $\partial^2 \Delta(p + \rho u^2) / \partial m^2 = 0$  for oscillatory instability cases using CFD and 1-D codes

### 6.5 Effect of Turbulent Prandtl Number

In this section, the effect of  $Pr_t$  on the instability threshold is examined. Two oscillatory cases (Case O3 and Case O4) and one static instability case (Case S3) were selected to evaluate the effect of  $Pr_t$ . However, more cases and geometries should be studied to attain a final conclusion.

The variations of wall temperature and static pressure drop are shown in Figures 6.30 and 6.31, for Case S3. Figure 6.30 shows that reducing the  $Pr_t$ , reduces the wall temperature by about 50 K near the channel outlet. The reason for this reduction is that  $Pr_t$  is defined as the ratio between the momentum eddy diffusivity and the thermal eddy diffusivity and with the increase of  $Pr_t$ , the diffusion term of the energy equation reduces. Since there is no flow in the radial direction at the wall and only the diffusion transports the heat from

the wall to the fluid, with the decrease of diffusion effect the heat transfer in the radial direction lessens and the heat transfer coefficient reduces. Therefore, according to Equation (6.3), for a fixed amount of heat flux, the wall temperature is higher when  $Pr_t$  is larger.

$$Q = hA(T_w - T_b) \rightarrow q'' = h(T_w - T_b) \quad (6.3)$$

where  $q''$  is the heat flux at the wall,  $h$  is the convection heat transfer coefficient,  $T_w$  and  $T_b$  are the wall surface temperature and the average bulk temperature of the fluid, respectively. Although the change of wall temperature with  $Pr_t$  is considerable, it has a small effect on the static pressure drop as shown in Figure 6.31.

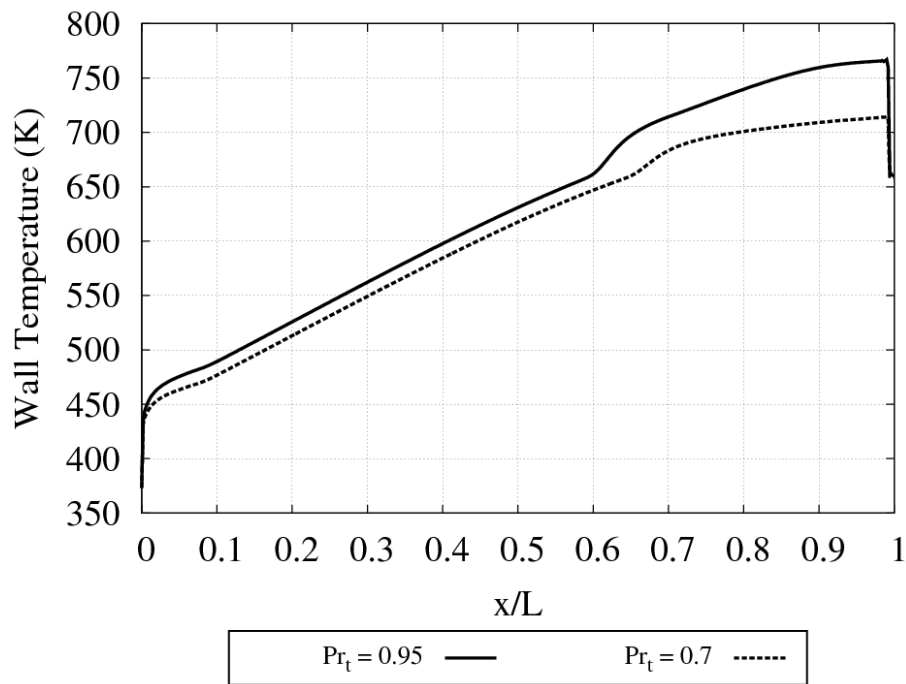


Figure 6.30: Comparison of wall temperature between two values of  $Pr_t$  for Case S3 ( $\dot{m} = 0.061$  kg/s)

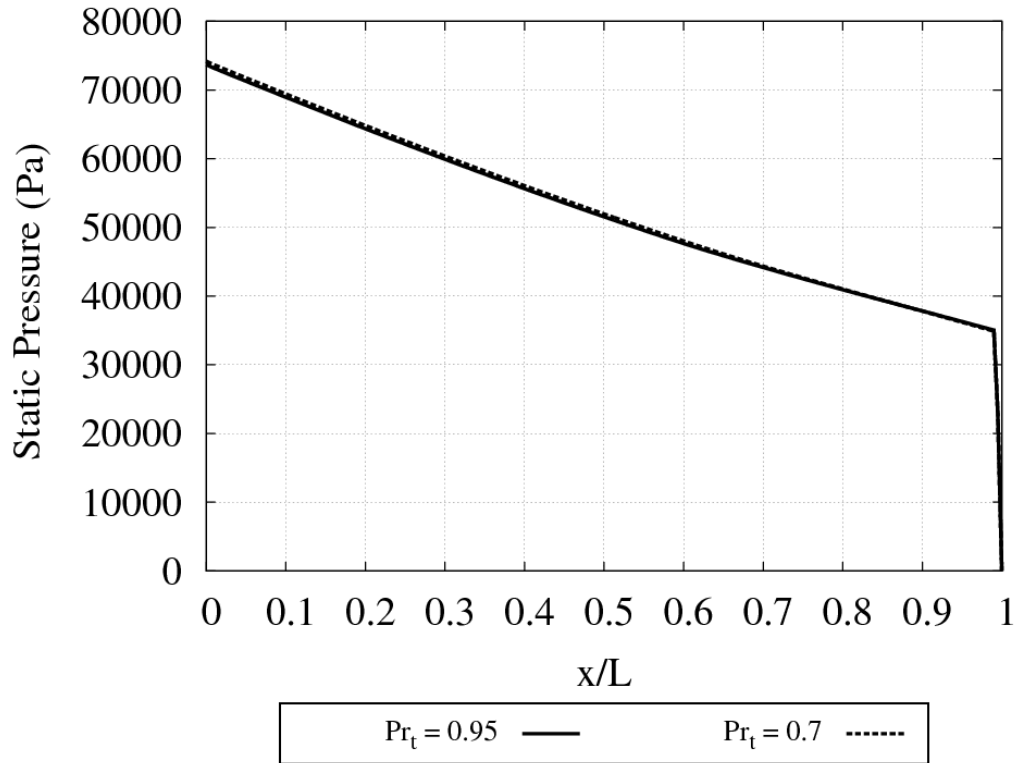


Figure 6.31: Comparison of static pressure between two values of  $Pr_t$  for Case S3 ( $\dot{m} = 0.061$  kg/s)

The variations of wall temperature and static pressure are shown in Figures 6.32 and 6.33 for Case O4. Figure 6.32 shows that reducing the  $Pr_t$ , reduces the wall temperature by about 20 K near the outlet. Like Case S3, here also the static pressure remained almost unaffected by the change of  $Pr_t$ , as shown in Figure 6.33.

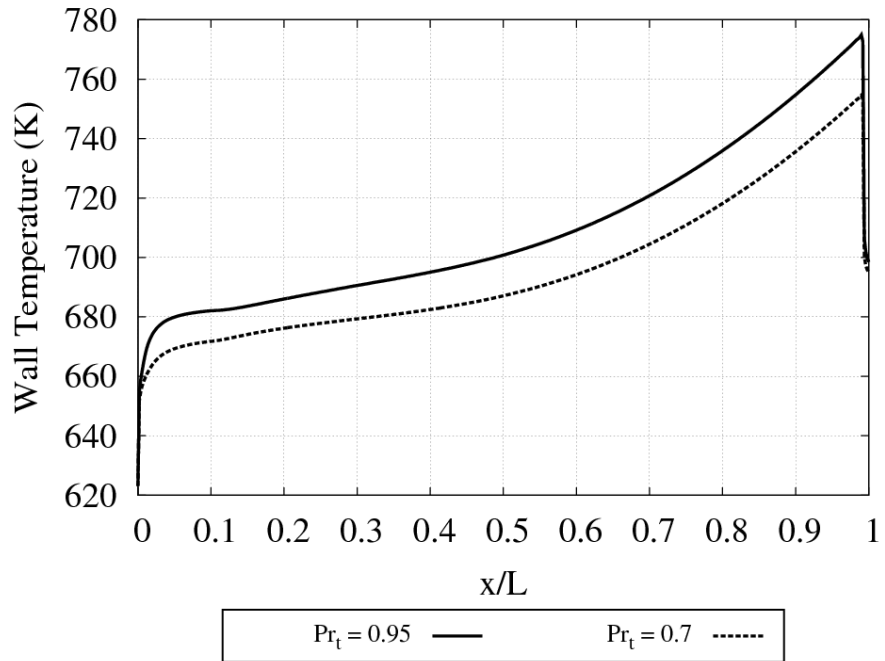


Figure 6.32: Comparison of wall temperature between two values of  $Pr_t$  for Case O4 ( $\dot{m} = 0.089$  kg/s)

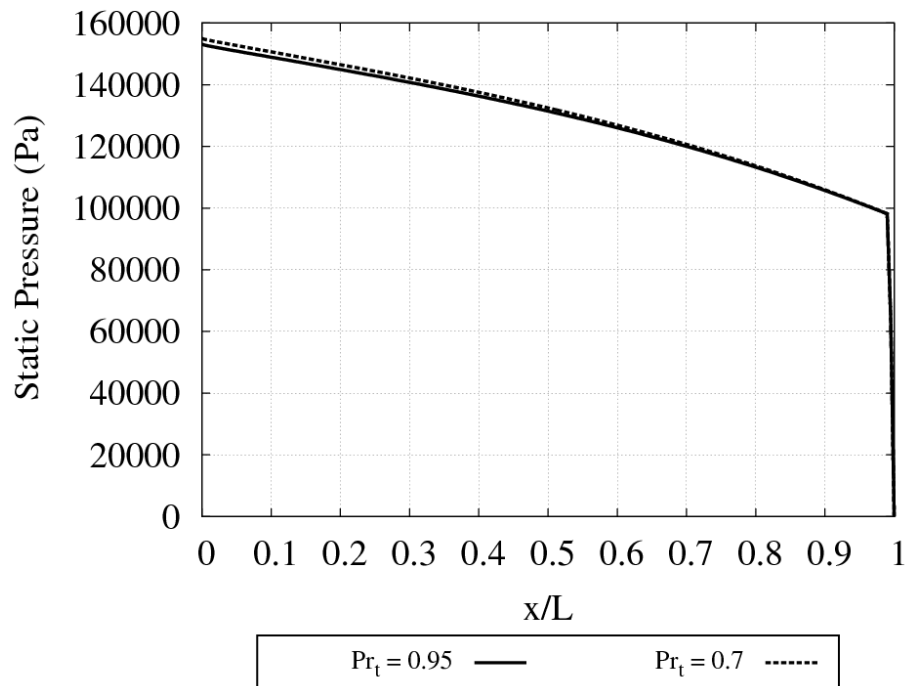


Figure 6.33: Comparison of static pressure between two values of  $Pr_t$  for Case O4 ( $\dot{m} = 0.089$  kg/s)

To see the effect of  $Pr_t$  on the flow behaviour in the absence of an outlet K factor, Case O3 was chosen and repeated with the  $Pr_t$  of 0.7. As shown in Figure 6.34, in this case also, there is a considerable difference between the two wall temperatures. As shown in Figure 6.35, here the difference of the static pressure between two values of  $Pr_t$  is more noticeable than in Case O4.

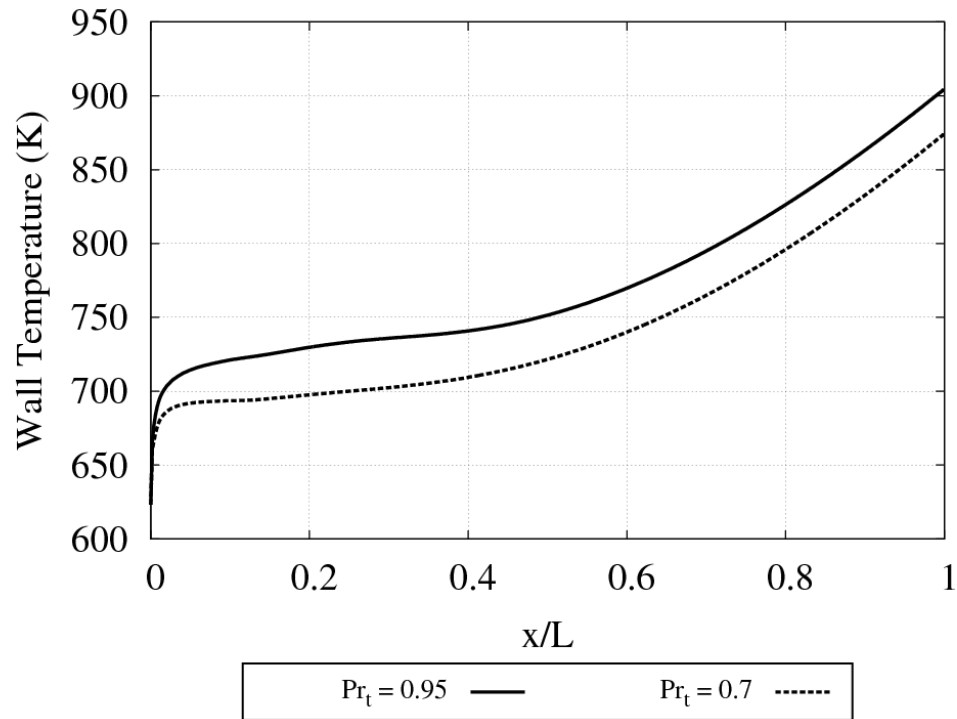


Figure 6.34: Comparison of wall temperature between two values of  $Pr_t$  for Case O3 ( $\dot{m} = 0.067$  kg/s)

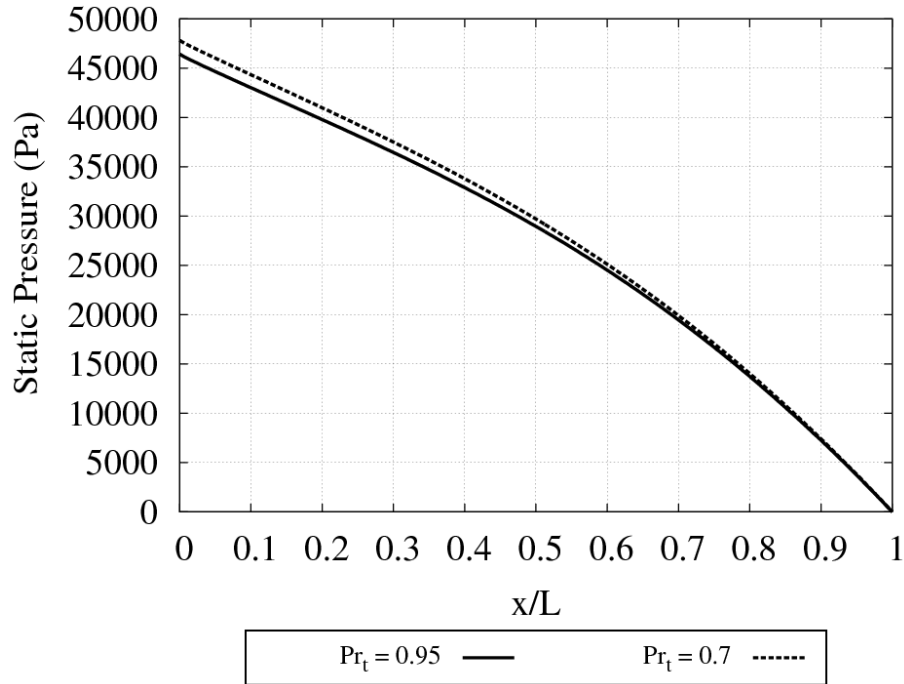


Figure 6.35: Comparison of static pressure between two values of  $Pr_t$  for Case O3 ( $\dot{m} = 0.067 \text{ kg/s}$ )

Figure 6.36 shows the variation of terms 1, 3 and 5 in Equation (6.1) with the non-dimensional length of the pipe for Case O3 using the two values of  $Pr_t$ . The hydrostatic term stays the same for both values of  $Pr_t$  and the RMS differences of gravitational and acceleration pressure drops between the two values of  $Pr_t$  are  $0.000417 \text{ N/m}$  (0.27% of the averaged magnitude along the pipe) and  $0.0013 \text{ N/m}$  (0.73% of the averaged magnitude along the pipe), respectively. This figure shows that the friction force gradient caused by frictional pressure drop is the main component that is different between the two cases and it causes the difference in the static pressure shown in Figure 6.35. Term 4 is also slightly different between the two cases, especially near the inlet of the flow.

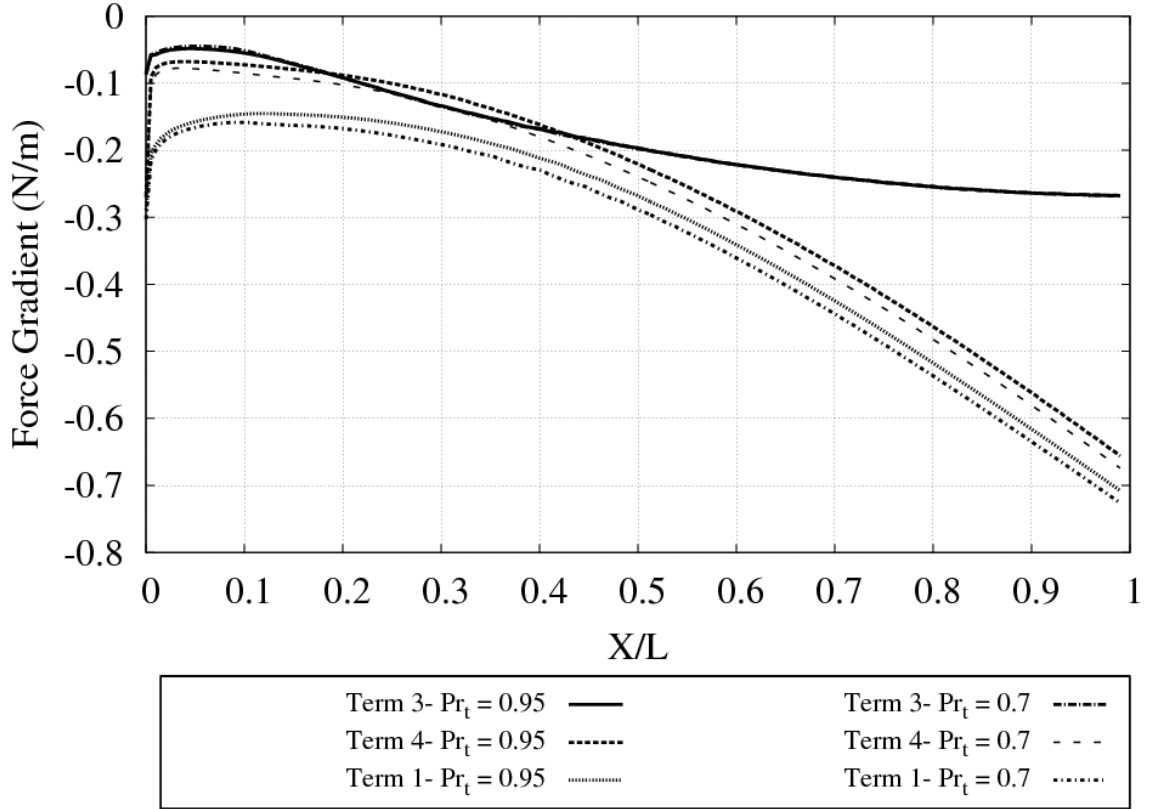


Figure 6.36: Axial variation of different terms in Equation (6.1) using  $Pr_t = 0.7$  and  $0.95$  for Case O3 ( $\dot{m} = 0.067$  kg/s)

$Pr_t$  has a considerable effect on the heat transfer characteristics of the flow. However, whether it affects the instability boundary or not has not been discussed before. Table 6.12 shows the effect of  $Pr_t$  on the static instability thresholds and CFD flow rates corresponding to  $\partial \Delta(p + \rho u^2)/\partial \dot{m} = 0$  and  $\partial \Delta(p)/\partial \dot{m} = 0$  for Case S3, using the SST model. These results also show that  $Pr_t$  does not have a noticeable effect on the instability threshold and the mass flow rates corresponding to  $\partial \Delta(p + \rho u^2)/\partial \dot{m} = 0$  and  $\partial \Delta(p)/\partial \dot{m} = 0$ .

Table 6.12: Comparison of static instability threshold mass flow rates between two values of  $Pr_t$  using the SST model

Case	$Pr_t$ Number	CFD Instability Threshold Mass Flow Rate (kg/s)	CFD Mass Flow Rate corresponding to $\partial \Delta(p + \rho u^2)/\partial \dot{m} = 0$ (kg/s)	CFD Mass Flow Rate corresponding to $\partial (\Delta p)/\partial \dot{m} = 0$ (kg/s)
<b>S3</b>	0.7	0.062	0.06	0.062
	0.95	0.0615	0.06	0.062

Table 6.13 shows the comparison of CFD mass flow rate predictions for the instability thresholds and corresponding to  $\partial^2 \Delta(p + \rho u^2)/\partial \dot{m}^2 = 0$  between  $Pr_t$  of 0.95 and 0.7 for oscillatory instability cases of O3 and O4, using the SST model. Results show that, especially in case of having a K factor where the pressure drop is dominated by the K factor,  $Pr_t$  does not have a noticeable effect on the instability threshold. Still in Case O3, the difference of 2 kPa was not large enough to make much difference in the instability threshold. Therefore, the difference of instability threshold between two  $Pr_t$  numbers is small enough to consider the results of this study independent of  $Pr_t$  number.

Table 6.13: Comparison of oscillatory instability threshold mass flow rates between two values of  $Pr_t$  using the SST model

Case	$Pr_t$ Number	CFD Instability Threshold Mass Flow Rate (kg/s)	CFD Mass Flow Rate corresponding to $\partial^2 \Delta(p + \rho u^2)/\partial \dot{m}^2 = 0$ (kg/s)	Difference of Instability Threshold between $Pr_t=0.7$ and $Pr_t=0.95$ (%)
O3	0.7	0.064	0.0635	4.47
	0.95	0.067	0.0685	
O4	0.7	0.09	0.086	0
	0.95	0.09	0.0865	

## **6.6 Effect of Outlet K Factor**

It is well known that introducing an outlet K factor destabilizes the system and causes the instability onset to happen at a higher mass flow rate, for a constant power. The reason is the increase in the pressure drop on the vapor side of the channel when having an outlet K factor. The present CFD work also confirms the increase in the instability threshold mass flow rate by increasing the outlet K factor, both for static and oscillatory instabilities, when the flow is upward (Tables 6.3 and 6.8).

## **6.7 Effect of Inlet Temperature**

It has been verified that the inlet temperature has a non-monotonic effect on the instability threshold and increasing the inlet temperature can either destabilize or stabilize the system (Jain and Rizwan-uddin, 2007, Xiong et al., 2012, Chatoorgoon, 2013). In the current study, only two different inlet temperatures were examined while the other parameters were remained unchanged. Therefore, the current CFD results are not enough to draw a conclusion on the effect of inlet temperature on the instability threshold. However, for all the cases tests, increasing the inlet temperature destabilized the system and caused the instability to happen at a higher mass flow rate.

## **6.8 Variation of Properties in the Heat Transfer Deteriorated Region**

As discussed in Chapter 5, the heat transfer deterioration (HTD) is characterized by lower values of heat transfer coefficient and, therefore, higher values of temperature near the wall, compared to the normal heat transfer mode. HTD may happen in some parts of the heated channel or within the entire channel at either low or high mass flow rates. Figure 6.37 shows the variation of wall temperature along the pipe for three different mass flow rates obtained using the SST turbulence model for Case S2, leading to deteriorated mode

of heat transfer. As mass flow increases, the peak value of wall temperature reduces and shifts towards the outlet of the flow.

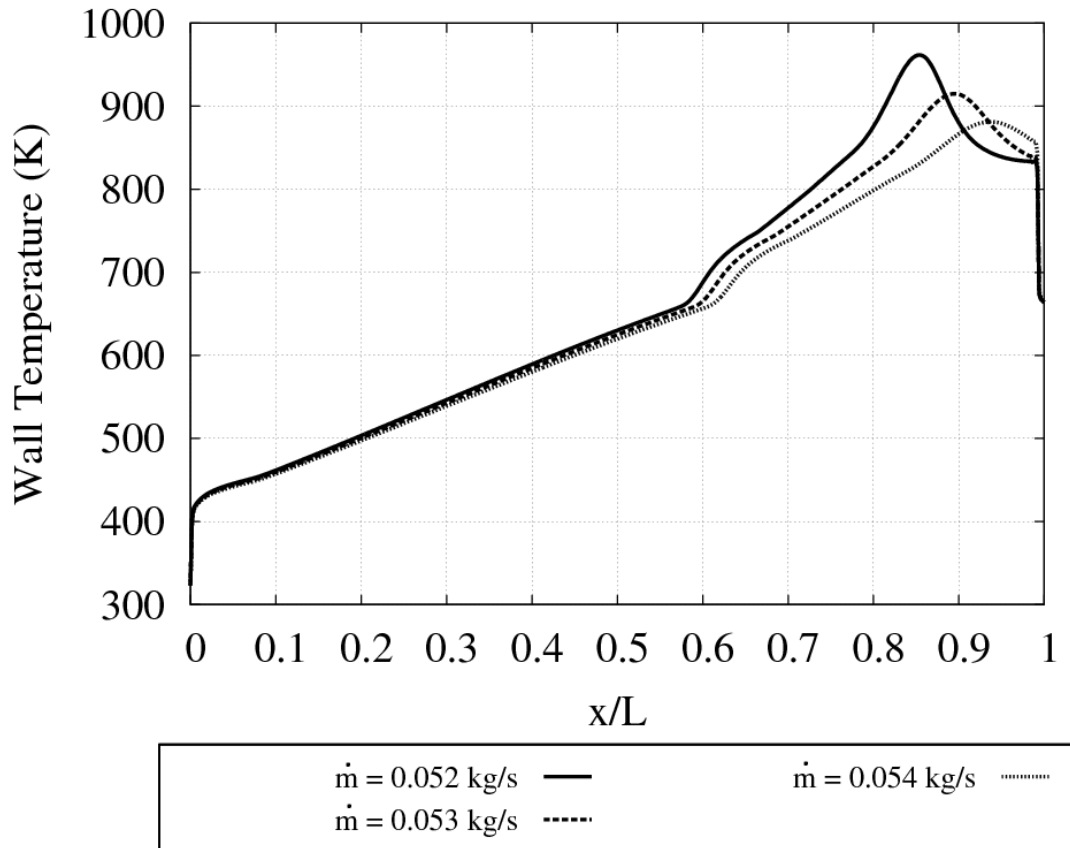


Figure 6.37: Axial variation of wall temperature for different mass flow rates leading to HTD using the SST model for Case S2

To find out the reason for this behavior of wall temperature, Case S2 with a mass flow rate equal to 0.052 kg/s was chosen. The temperature peak in this case occurred at the axial location of  $x/L = 0.85$ , as seen in Figure 6.37.

For this case, the axial variation of near-wall thermal conductivity is shown in Figure 6.38, before the K factor region. Before the wall temperature reaches the pseudo-critical temperature (656 K), the thermal conductivity is large and, therefore, the near-wall fluid experiences a normal heat transfer rate. After the wall temperature reaches the pseudo-critical temperature, the thermal conductivity decreases sharply and acts to reduce the

heat transfer from the wall to the fluid and, therefore, the wall temperature starts to increase sharper and the heat transfer deterioration region begins. As the wall temperature increases, the value of near-wall density reduces and leads to an acceleration of flow near the wall. As shown in Figure 6.39, the M-shaped velocity profile occurs slightly before the peak of temperature. Figure 6.40 shows the variations of velocity gradient and turbulence kinetic energy near the wall. The velocity gradient after the pseudo-critical point starts to decrease. Since the production term in the turbulence kinetic energy equation is a function of velocity gradient, the decrease in the velocity gradient reduces the production term and, therefore, reduces the turbulence kinetic energy. This process continues until the near-wall higher momentum is transported to the bulk fluid and the velocity of the fluid in the whole section starts to increase and leads to heat transfer recovery after  $x/L = 0.85$ . After this point, the acceleration of near-wall flow leads to an increase in the turbulence kinetic energy and wall temperature starts to decrease.

All the cases of this study leading to a static instability had some regions of deteriorated heat transfer.

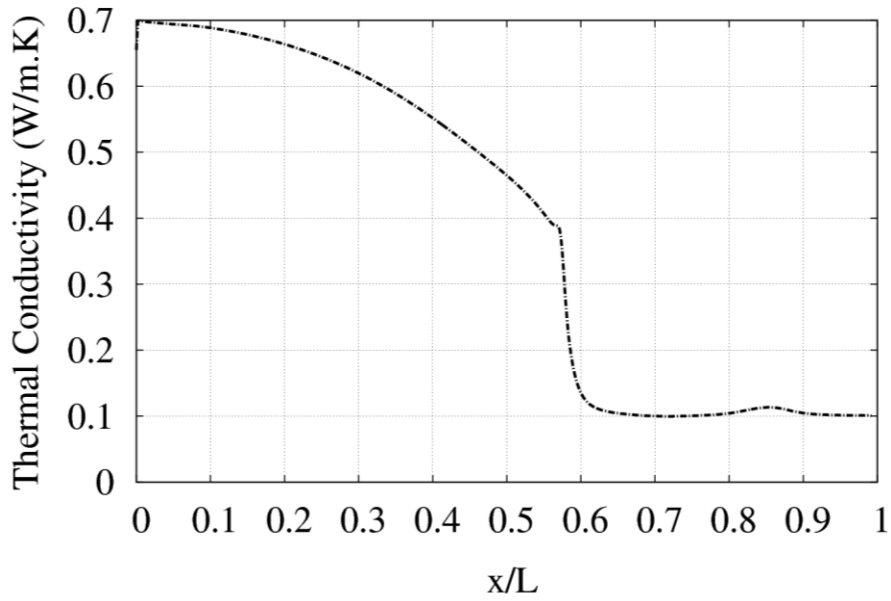


Figure 6.38: Axial near-wall variation of thermal conductivity for the region before the K factor, using the SST model for Case S2 ( $\dot{m} = 0.052$ )

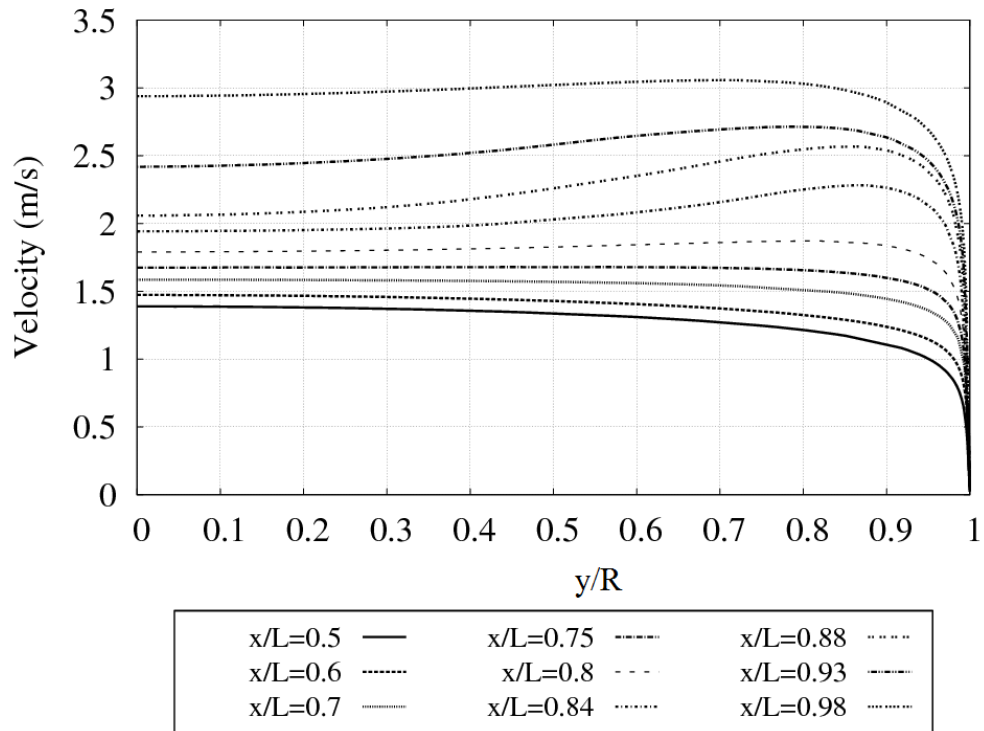


Figure 6.39: Radial variation of velocity at different axial locations using the SST model for Case S2 ( $\dot{m} = 0.052$  kg/s)

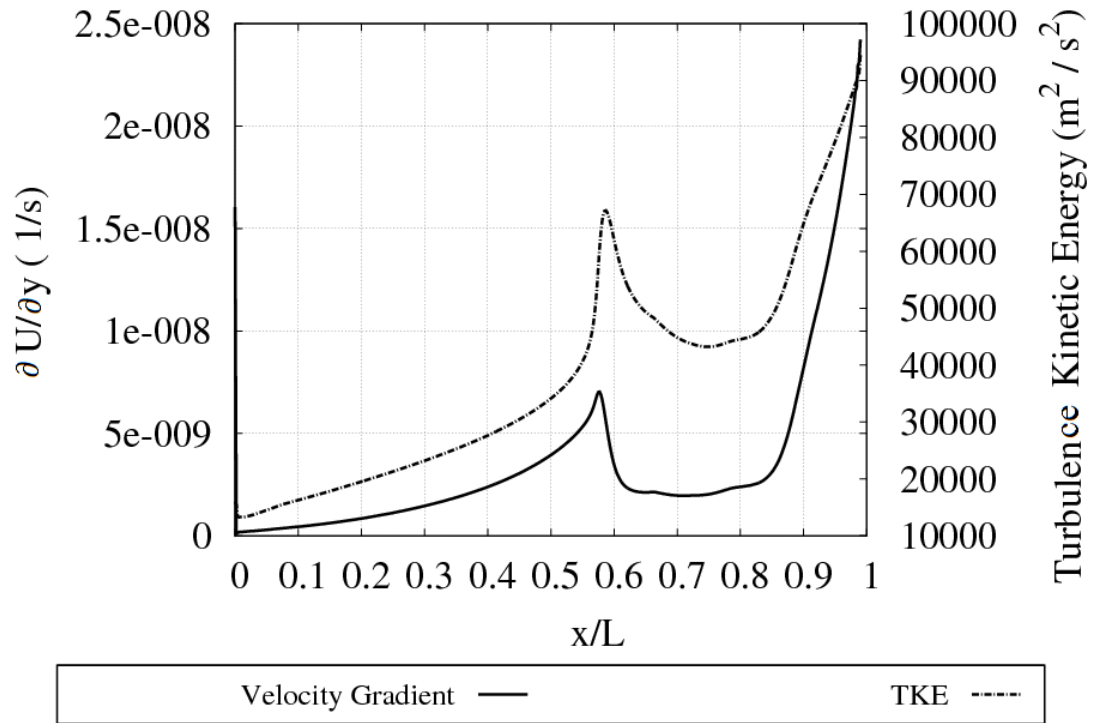


Figure 6.40: Axial near-wall variation of velocity gradient and turbulence kinetic energy for the region before the K factor, using the SST model for Case S2 ( $\dot{m} = 0.052 \text{ kg/s}$ )

## CHAPTER 7

### SUMMARY, CONCLUSIONS, AND RECOMMENDATIONS

#### 7.1 Summary

A numerical study was conducted to model 2-D axisymmetric pipes with upward flow of supercritical water, using RANS models in ANSYS CFX v14.5 code. First, three computational domains were simulated and results were compared with the experimental data of wall temperature and frictional pressure drop and reasonably good agreements were found. Based on the results of validations with experimental data, a constant value for  $Pr_t$  was selected in studying the remaining cases. Secondly, analysis of the static and oscillatory instabilities was performed in a vertical pipe with up-flow at 25MPa with 100 kW power input using a constant wall heat flux. Eight cases with different inlet temperatures and outlet K factors were studied and reported. Specifying a K factor allows introducing the desired pressure drop in the form of the momentum source term. To find the mass flow rate at the instability threshold, for each flow rate, a separate steady-state analysis was performed to obtain the pressure drop of the system. That pressure drop was then used as an inlet boundary condition to perform the transient simulation. Two turbulence models were used to find the instability threshold: the standard  $k-\epsilon$  model with a scalable wall-function and the  $k-\omega$  based SST model. The instability thresholds predicted by these two models were compared. The results of the CFD code were also compared with 1-D non-linear code solutions. Also, conditions for approximating the thresholds of static and oscillatory instabilities based on steady-state results were assessed and discussed. In addition, two different constant values of  $Pr_t$  were used to

study the effect of  $Pr_t$  on the instability threshold. Finally, the effects of inlet temperature and outlet K factor on the instability threshold were discussed briefly.

## 7.2 Conclusions

The following conclusions were drawn from the results of the simulations:

- Using Ambrosini's geometry, the results of instability thresholds between the  $k-\varepsilon$  and the SST models were close and the largest difference, which appeared in Case S4, was equal to 7.38%.
- The maximum difference of CFD and 1-D instability thresholds for static instability was for Case S4 using the  $k-\varepsilon$  model. There is a relatively large difference between the oscillatory instability thresholds of 1-D and CFD codes. The maximum difference of CFD and 1-D instability thresholds for oscillatory instability was for Case O1, using the SST model and was equal to 21.7%.
- When analyzing the static instability, the maximum difference between mass flow rate instability threshold of CFD and mass flow rate corresponding to Chatoorgoon's condition ( $\partial \Delta(p + \rho u^2)/\partial \dot{m} = 0$ ) happened in Case S4 using the SST model and was equal to 11.5%. When the power was doubled, the 11.5% difference was reduced to 3%, indicating the seemingly large differences may be due to the very low mass flow rates. However, the maximum difference between the mass flow rate at the instability threshold of CFD and the mass flow rate corresponding to Ledinegg's condition ( $\partial \Delta(p)/\partial \dot{m} = 0$ ) happened in Case S4 using the SST model and was equal to 2.46 %. For other cases the difference was insignificant. Hence, approximating the flow instability threshold by the minimum of  $\Delta(p + \rho u^2)$  versus mass flow rate

curve and the minimum of  $\Delta p$  versus mass flow rate curve held true for a CFD solution for the cases studied in the present work. Ledinegg's criteria, however, agreed better with the CFD results (when there are no inlet and outlet plena). Therefore, Ledinegg's criterion is clearly more suitable for channels without plena.

- When analyzing the oscillatory instability, the maximum difference between the mass flow rate at the instability threshold of CFD and the mass flow rate corresponding to Chatoorgoon's condition ( $\partial^2\Delta(p + \rho u^2)/\partial\dot{m}^2 = 0$ ) happened in Case O1 using the  $k-\varepsilon$  model. For other cases the difference was insignificant. Hence, approximating the flow instability threshold by the minimum of the  $\partial\Delta(p + \rho u^2)/\partial\dot{m}$  curve seemed to hold true for CFD solutions for the cases studied in the present work, although, work has to continue for channels with plena.
- Through examining Cases O3, O4, and S3, results showed that  $Pr_t$  did not have a noticeable effect on the instability threshold, especially in cases with an outlet K factor where the pressure drops were dominated by the K factor. However, more investigations have to be done to obtain a final conclusion on the effect of  $Pr_t$  on the instability threshold.
- The present CFD work confirmed the increase in the instability threshold mass flow rate by increasing the outlet K factor, both for static and oscillatory instabilities.
- It had been proven previously that increasing the inlet temperature can either destabilize or stabilize the system. In the current study, only two different inlet temperatures were examined while the other parameters remained unchanged. Therefore, the current CFD results were not enough to draw a conclusion on the

effect of inlet temperature on the instability threshold. However, for all the cases examined, increasing the inlet temperature destabilized the system and caused the instability to happen at a higher mass flow rate.

- In the case of Shitsman's experiment, all values of  $Pr_t$  were able to predict the trend of axial temperature. However, for some  $Pr_t$  numbers, the magnitude of temperature at the second peak was not predicted accurately, and for others the location of the second peak was not predicted correctly. Also, the magnitudes of the temperature at the first peak and after the peak were over-predicted for all of the values of  $Pr_t$  used. CFX also failed to predict the reduction in the wall temperature near the channel outlet. However,  $Pr_t$  equal to 1 gave a better overall agreement of wall temperature along the pipe.
- In the case of Ornatsky's experiment, all values of  $Pr_t$  were able to predict the trend of axial temperature. The onset of the heat transfer deterioration was predicted well using all values of  $Pr_t$ . However, in the region of heat transfer deterioration, the results obtained using different values of  $Pr_t$  deviated from experimental data and as  $Pr_t$  increased, the wall temperature in the region of deteriorated heat transfer increased. For any given  $Pr_t$  value, CFX failed to predict the decrease in the wall temperature at the pipe outlet. However,  $Pr_t$  equal to 0.9 gave a better overall agreement of wall temperature with the experiment data.
- In the case of Ishigai's experiment, both the SST and the  $k-\varepsilon$  turbulence model show good agreement with the experimental data of frictional pressure drop. However, the  $k-\varepsilon$  turbulence model under-predicted the frictional pressure drop slightly.

### 7.3 Recommendations

The following recommendations are made for future studies:

- The study should be repeated for channels with plena to be more realistic.
- Extend the study to down-flow and horizontal flow orientations.
- Use large eddy simulation (LES) or develop more robust turbulence models. RANS models sometimes fail to predict the critical conditions of the flow such as cases of strong HTD and buoyancy. Since performing DNS studies, especially for complex geometries, is expensive and time-consuming, the use of LES or other turbulence models that are capable of determining anisotropy in the flow would be worth pursuing.
- Investigate further the effect of inlet temperature on the static and oscillatory instability thresholds. The non-monotonic effect of inlet temperature requires a wide range of inlet temperatures to be examined.
- Explore the effect of spatially variable  $Pr_t$  numbers on the instability threshold. Different correlations have been defined for  $Pr_t$  as function of  $Pr$ ,  $y^+$ ,  $Pe_t$ , etc. Some of these correlations were reviewed in Chapter 5. Although, the effect of variable values of  $Pr_t$  on the heat transfer characteristics of supercritical flow has been studied to some extent, the effect of that on the instability threshold has not been investigated yet.
- Analyze static and oscillatory instabilities in different geometries with different lengths and diameters. In the current study, only one geometry was used to analyze

the instability in the flow. Whether the conclusions drawn in this study are applicable to other geometries is an important matter that should be explored.

- Study the instability in another fluid rather than water. Although water is the main fluid used in SCWRs, other fluids like CO<sub>2</sub> and Helium, and Methane are also possible to be used at supercritical pressures and are worth examining.

## REFERENCES

Ambrosini, W., Di Marco, P., Susaneck, A., 1999, Prediction of boiling channel stability by a finite-difference numerical method, 2nd International Symposium on Two-Phase Flow Modeling and Experimentation, Pisa, Italy.

Ampomah-Amoako, E. and Ambrosini, W., 2013, Developing a CFD methodology for the analysis of flow stability in heated channels with fluids at supercritical pressures, *Annals of Nuclear Energy* 54, pp.251-262.

Bae, J.H., Yoo, J.Y., Choi, H., 2005, Direct numerical simulation of turbulent supercritical flows with heat transfer, *Phys. Fluids* 17, pp.1–24.

Barth, T.J. and Jespersen, D.C., 1989, The design and application of upwind schemes on unstructured meshes, *AIAA Paper* 89-0366,

Bazargan, M. and Mohseni, M., 2009, Effect of turbulent Prandtl number on the convective heat transfer to turbulent upflow of supercritical carbon dioxide, *Proceeding of the ASME, Heat Transfer Summer Conference HT2009-88461*, San Francisco, California USA.

Blasius, H., 1913, *Mitt.Forsch.Geb.Ing.-Wesen* 131, pp.1-41.

ANSYS, Inc., 2014, *ANSYS CFX-Solver Theory Guide*.

Boure, J.A., Bergles A.E. and Tong, L. S., 1973, Review of Two-Phase Flow Instability, Nuclear Engineering and Design 25, pp.165-192.

Bourke, P., Pulling, D., 1971, Experimental explanation of deterioration in heat transfer to supercritical carbon dioxide, Transaction of ASME, N 71-HT-24.

Brady, D., Duffey, R., Khartabil, H., Sadhankar, R and Suppiah, S., 2007, Generation IV reactor development in Canada, 3<sup>rd</sup> Int. Symposium on SCWR, Shanghai, China.

Chatoorgoon, V., 1986, SPORTS - A simple non-linear thermalhydraulic stability code, Nuclear Engineering and Design, Volume 93, Issue 1, pp. 51–67.

Chatoorgoon, V., 2001, Stability of Supercritical Fluid Flow in a Single-Channel Natural-Convection Loop, International Journal of Heat and Mass Transfer 44, pp.1963-1972.

Chatoorgoon, V., 2006, Supercritical Flow Stability in Two Parallel Channels, Proceedings of Int. Conf. of Nuclear Engineering, ICONE 14-89692.

Chatoorgoon, V., 2013, Non-dimensional parameters for static instability in supercritical heated channels, Int. J. of Heat and Mass Transfer 64, pp.145-154.

Chen, Y., Zhao, M., Yang, C., Bi, K., Du, K., 2013, Experiment of heat transfer of supercritical water in natural circulation with different diameters of heated tubes, ISSCWR6-13097, ISSCWER-6, Shenzhen, Guangdong, China.

Daney, D.E., Ludtke, P.R. and Jone, M.C., 1979, An experimental study of thermally-induced flow oscillations in supercritical Helium, J. of Heat Transfer 101, pp.9-14.

Duffey, R.B., Pioro, I.L., 2005, Experimental heat transfer of supercritical carbon dioxide flowing inside channels (survey), Nucl. Eng. Design 235, pp. 913–924.

Duffey, R.B. and Pioro, I.L., 2005, Supercritical Water-cooled Nuclear Reactors: Review and Status, In Nuclear Materials and Reactors from Encyclopedia of Life Support Systems (EOLSS).

Fukuda, K., Hasegawa, S., Kondoh, T., Nozaki, F. and Nagayoshi, T., 1991, Instability of supercritical Helium flow, Transaction of the Japan Society of Mechanical Engineers Series B., pp.621-625.

Gomez, T. O., Class, A., Lahey, R. T. and Schulenberg, T., 2006, Stability Analysis of a Uniformly Heated Channel with Supercritical Water, Proceedings of ICONE14, International Conference on Nuclear Engineering, Miami, Florida.

Grotjans, H. and Menter, F.R., 1998, Wall functions for general application CFD codes, ECCOMAS 98 Proceeding of the Fourth European Computational Fluid Dynamics Conference, pp.1112-1117.

He, S., Kim, W.S. and. Bae, J.H., 2008, Assessment of performance of turbulence models in predicting supercritical pressure heat transfer in a vertical tube, *Int. J. Heat Mass Transfer* 51, pp.4659–4675.

Hendricks, R.C., Simoneau, R.J. and Smith, R.V., 1970, Survey of heat transfer to near-critical fluids, Report No. NASA TN-D-5886, Lewis Research Center, NASA, USA, 116 pages.

Hollingsworth, D.K., Kays, W.M. and Moffat, R.J., 1989, Measurement and prediction of the turbulent thermal boundary layer in water on flat and concave surface, Report No. HMT-41, Thermosciences division, Dept. of Mech Eng., Stanford University.

Howell, J.R. and Lee, S.H., 1999, convective heat transfer in the entrance region of a vertical tube for water near the thermodynamic critical point, *International Journal of Heat and Mass Transfer*, pp.1177-1187.

Ishigai, S., Kadji, M., Nakamoto, M., 1981, Heat transfer and pressure drop under water flow at supercritical pressure, *JSME J. Ser. B* 47 (424), pp. 2333–2349.

Jain, R., Litch, J., Anderson, M., Corradini, M., Lomperski S. and Chao, D. H., 2003, Studies of Natural Circulation Heat Transfer and Flow Stability of a Supercritical Fluid, The 10<sup>th</sup> International Topical Meeting on Nuclear Reactor Thermal Hydraulics (NURETH-10), Seoul, Korea, October 5-9.

Jain, P.K., Rizwan-uddin, 2008, Numerical analysis of supercritical flow instabilities in a natural circulation loop, Nuclear Engineering and Design 238, pp.1947–1957.

Jaromin, M. and Anglart, H., 2013, A numerical study of heat transfer to supercritical water flowing upward in vertical tubes under normal and deteriorated conditions, Nuclear Engineering and Design, v. 264, pp.61-70.

Kakac, S., Bon, B., 2008, Review of two-phase flow dynamic instabilities in tube boiling systems, International Journal of Heat and Mass Transfer 51, pp. 399-433.

Kao, M.T., Lee, M., F, Y.M., Chieng, C.C., 2010, Heat transfer deterioration in a supercritical water channel, Nuclear Engineering and Design 240, pp.3321-3328.

Kays, W.M., 1994, Turbulent Prandtl number-where are we?, Journal of Heat Transfer 116, pp.284-295.

Kays, W.M., Crawford, M.E., 2005, Convective heat and mass transfer, 4th ed., McGraw-Hill.

Kurganov, V.A., Ankundinov, V.B., Kaptil'nyi, 1986, A.G. Experimental study of velocity and temperature fields in an ascending flow of carbon dioxide at supercritical pressure in a heated vertical tube. *High Temp.* 24 (6), pp.811–818.

Lauder, B.E. and Spalding, D.B., 1974, The numerical computation of turbulent flows, *Computational Methods and Applied Mechanics Engineering*, vol. 3, pp.269-289.

Ledinegg, M., 1938, Instability of flow during natural and forced convection, *Die Wärme*, 61 (8), pp.891-898.

Lemmon, E.W., Huber, M.L., McLinden, M.O., 2013, NIST Standard Reference Database 23: Reference Fluid Thermodynamic and Transport Properties-REFPROP, Version 7, National Institute of Standards and Technology, Standard Reference Data Program.

Lorentzen, G., 1994, Revival of carbon dioxide as a refrigerant, *International Journal of Refrigeration* 17 (5), pp. 292-301.

LV, F., Huang, Y.P., Wang, Y.L., Yan, X., 2013, Experimental Observation of Supercritical Water Natural Circulation Instabilities, The 15th International Topical Meeting on Nuclear Reactor Thermalhydraulics, NURETH-15 NURETH15-193, Pisa, Italy.

Launder, B. E., and Sharma, B. I., 1974, Application of the energy dissipation model of turbulence to the calculation of flow near a spinning disc, Letters in Heat and Mass Transfer, vol. 1, no. 2, pp. 131-138.

Menter, F. R., 1993, Zonal two equation  $k-\omega$  turbulence models for aerodynamic flows, AIAA Paper 93-2906.

Menter, F. R., 1994, Two-Equation Eddy-Viscosity Turbulence Models for Engineering Applications, AIAA Journal, vol. 32, no 8. pp. 1598-1605.

Mohseni, M. and Bazargan, M., 2011, The effect of the low Reynolds number  $k-\epsilon$  turbulence models on simulation of the enhanced and deteriorated convective heat transfer to the supercritical fluid flows, J. of Heat and Mass Transfer 47, pp.609-619.

Myoung, H.K., Kasagi, N., Hirata, M., 1989, Numerical prediction of turbulent pipe flow heat transfer for various Prandtl number fluids with the improved  $k-\epsilon$  turbulence model, JSME, Ser II, 32(4), pp.613-22

Ornatsky, A.P., Gluhchenko, L.F., Kalachev, S.I., 1971, Heat transfer with rising and falling flows of water in tubes of small diameter at supercritical pressures, Thermal Eng. 18 (5), pp.137.141.

Palko, P. and Anglart, H., 2008, Theoretical and numerical study of heat transfer deterioration in high performance light water reactor, Science and Technology of Nuclear Installation, 405072.

Pioro, I., Duffey, R. B., Dumouchel, T. J., 2004, Hydraulic resistance of fluids flowing in channels at supercritical pressures (survey), Nuclear Engineering and Design 231, pp. 187–197.

Pioro, I. and Mokry, S., 2011, Heat transfer to supercritical fluids, heat transfer-theoretical analysis, experimental investigations and industrial systems, InTech.

Rhie, C.M. and Chow, W.L., 1983, Numerical study of the turbulent flow past an air foil with trailing edge separation, AIAA Journal 21, 1525-1532.

Rodney, D., Wood, J. Smith, M., 1964, Heat transfer in the critical region—temperature and velocity profiles in turbulent flow, AIChE Journal Volume 10, Issue 2, pp180–186.

Sciencetech Inc., 1999, RELAP5/Mod3 Code Manual, vol. I: Code Structure, System Models and Solution Methods, The Thermal Hydraulics Group, Idaho.

Sharabi, M., Ambrosini, W. and He, S., 2008, Prediction of unstable behaviour in a heated channel with water at supercritical pressure by CFD models, Annals of Nuclear Energy 35, pp. 767–782.

Sharabi, M., Ambrosini, W., He, S., Jiang, P.X. and Zhao, C.R., 2009, Transient Three-Dimensional Stability Analysis of Supercritical Water Reactor Rod Bundle Subchannels by a Computational Fluid Dynamics Code, *J. Eng. Gas Turbines Power* 131, Issue 2, 022903.

Shitsman, M.E., 1963, Impairment of the heat transition at supercritical pressures, *High Temp.* 1 (2), pp.237-244.

Song, J.H., Kim, H.Y., Kim, H. and Bae, Y.Y., 2008, Heat transfer characteristics of a supercritical fluid flow in a vertical pipe, *J. of Supercritical Fluids*.

U.S. DOE Nuclear Energy Research Advisory Committee and the Generation IV International Forum, 2002, A Technology Roadmap for Generation IV Nuclear Energy Systems, GIF.

Wagner, W., Cooper, J. R., Dittmann, A., Kijima, J., Kretzschmar, H.J., Kruse, A., Mares, R., Oguchi, K., Sato, H., Stocker, I., Sifner, O., Takaishi, Y., Tanishita, I., Trubenbach, J. and Willkommen, Th., 2000, The IAPWS industrial formulation 1997 for the thermodynamic properties of water and steam, *Journal of Engineering for Gas Turbines and Power*, Transactions of the ASME, Vol. 122.

Weigand, B., Ferguson, J.R. and Crawford, M.E., 1997, An extended Kays and Crawford turbulent Prandtl number model, *Int. J. Heat Mass Transfer* 17, pp.4191-4196.

Wilcox, D.C., 1988, Re-assessment of the scale-determining equation for advanced turbulence models, *AIAA Journal*, vol. 26, no. 11, pp.1299-1310.

Xi, X., Xiao, Z., Yan, X., Xiong, T. and Huang, Y., 2014, Numerical simulation of the flow instability between two heated parallel channels with supercritical water, *Annals of Nuclear Energy* 64, pp.57-66.

Xiong, T., Yan, X., Huang, Sh., Yu, J. and Huang, Y., 2013, Modeling and analysis of supercritical flow instability in parallel channels, *Int. J. Heat and Mass Transfer* 57, pp.549–557.

Xiong, T., Yan, X., Xiao, Z.J., Li, Y.L., Huang, Y.P., Yu, J.C., 2012, Experimental study on flow instability in parallel channels with supercritical water, *Annals of Nuclear Energy* 48, pp.60-67.

Yamagata, K., Nishikawa, K., Haswgawa, S., Fuji, T. and Yoshida, S., 1972, Forced convective heat transfer to supercritical Water flowing in tubes, *Int. J. Heat Mass Transfer*, pp.2575-2593.

Yi, T.T., Koshizuka, S. and Oka, Y., 2004, A Linear Stability Analysis of Supercritical Water Reactors (I), Thermal-Hydraulic Stability, *Journal of Nuclear Science and Technology* 41, No.12, pp.1166-1175.

Yoo, J.Y., 2013, The turbulent flows of supercritical fluids with heat transfer, *Annu. Rev. Fluid Mech* 45, pp.495-525.

Zuber, N., 1966, An analysis of thermally induced flow oscillations in the near-critical and super-critical thermodynamic region, Rept. NASA-CR-80609, Research and Development Center, General Electric Company, Schenectady, New York, USA.

## APPENDIX A

### GEOMETRY AND GRID

To clearly demonstrate the details of the geometry and the grid generated, the steps which were taken to create the geometry and the mesh in ICEM CFD v.145 are shown for a 15 degree wedge. It should be noted again that the final geometry is a wedge with an angle of 1 degree. The overall steps used to create the geometry and the mesh are:

1. Points were created at the domain boundaries for the inlet and the outlet of the pipe by defining x, y, and z components of each point.
2. Curves were created from the points to define the edges of the geometry.
3. Surfaces were created using 3 or 4 curves.
4. Surfaces were defined as parts with names corresponding to the location of boundary conditions.
5. A body was created using the centroid of two points of the geometry.
6. Blocking was performed using 3-D bounding box (Figure A.1).
7. Two perpendicular splits were applied to the original single block on  $x$ - $y$  and  $x$ - $z$  planes (Figure A.2).
8. The lower left block (shown in Figure A.3) was deleted, which led to the geometry in Figure A.4.
9. To create a quarter O-Grid, six vertices were selected in the order shown in Figure A.4. A quarter O-Grid was created to fit the hexa blocks into a wedge (Figure A.5).
10. From the four blocks, three of them were deleted as shown in Figure A.6, which led to the geometry shown in Figure A.7.

11. Vertices of the blocking and points of the geometry were associated accordingly and the other vertices of blocking were moved to the desired locations (Figure A.8).

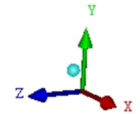
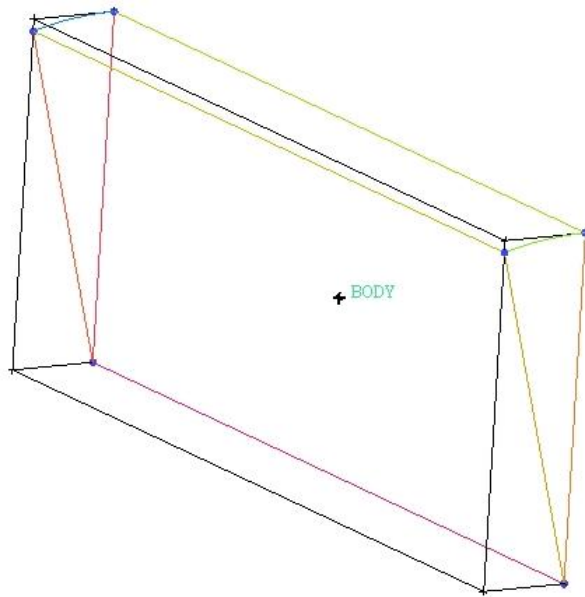


Figure A.1: 3-D bounding box

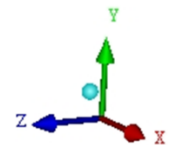
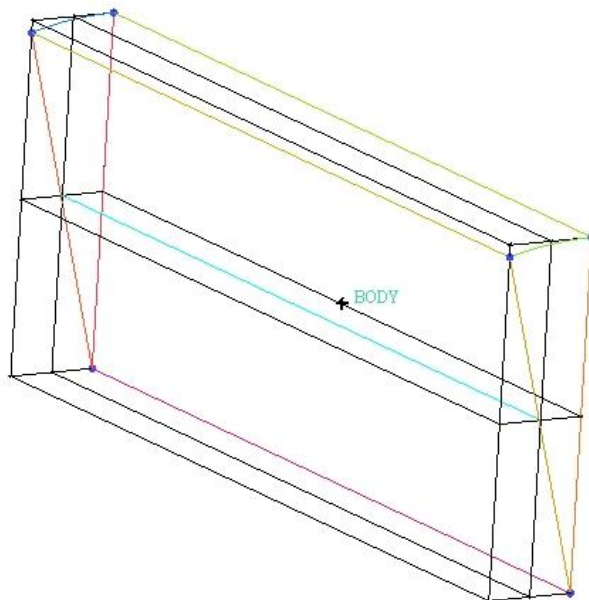


Figure A.2: Perpendicular splits on  $x$ - $y$  and  $x$ - $z$  planes

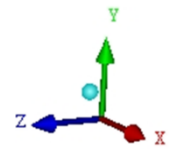
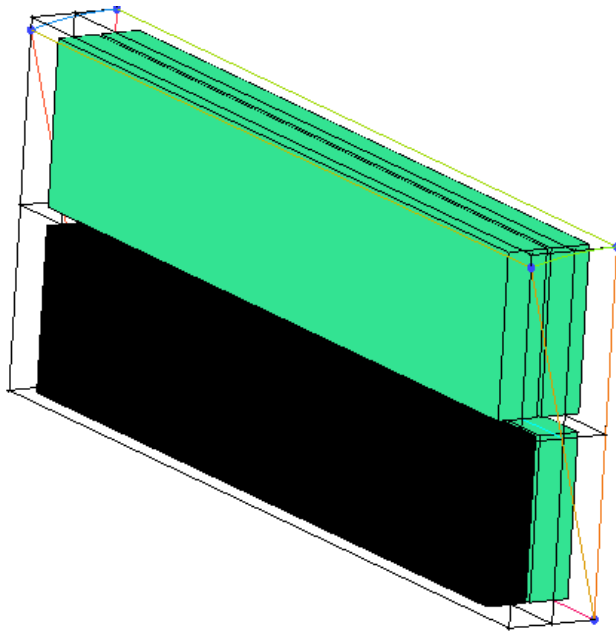


Figure A.3: The block which was deleted

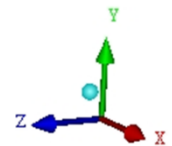
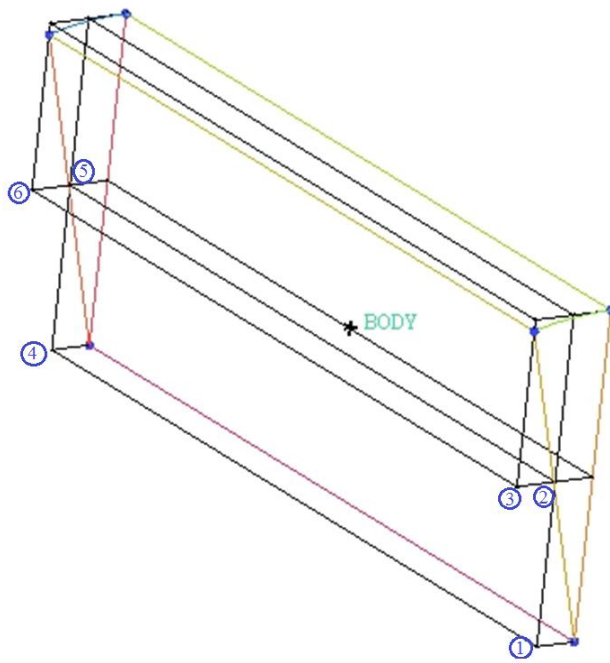


Figure A.4: Geometry and blocking after the lower left block was deleted

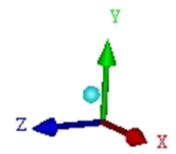
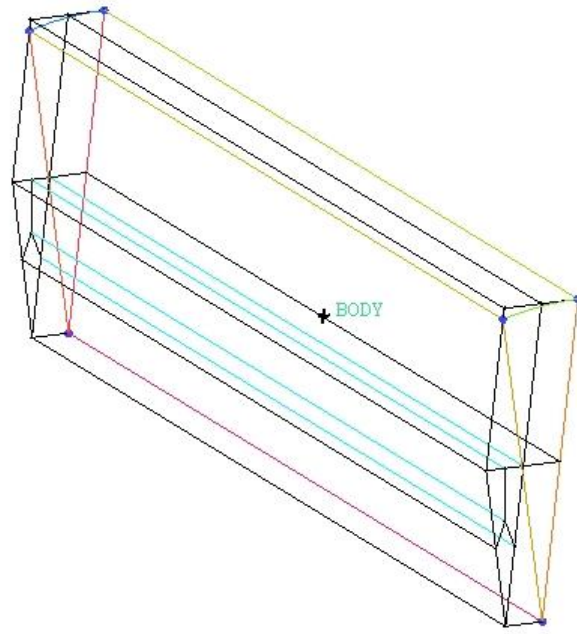


Figure A.5: Quarter O-Grid block

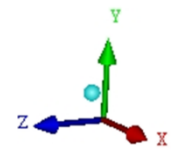
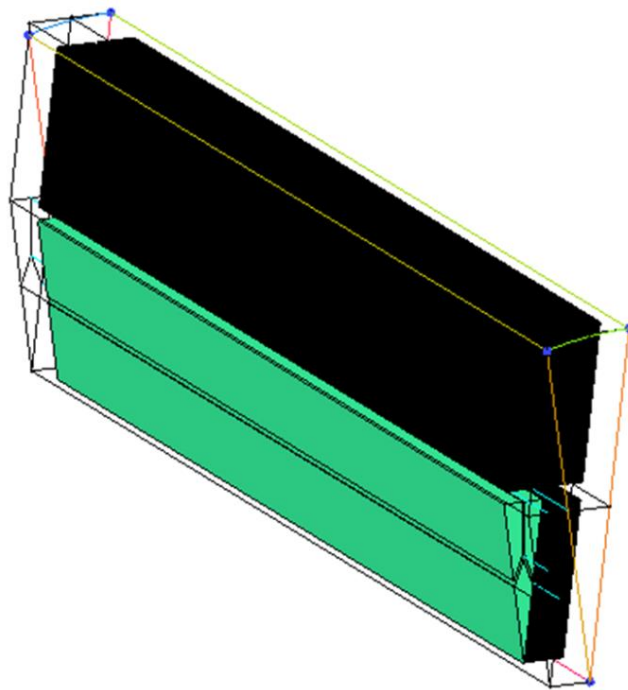


Figure A.6: Blocks that were deleted

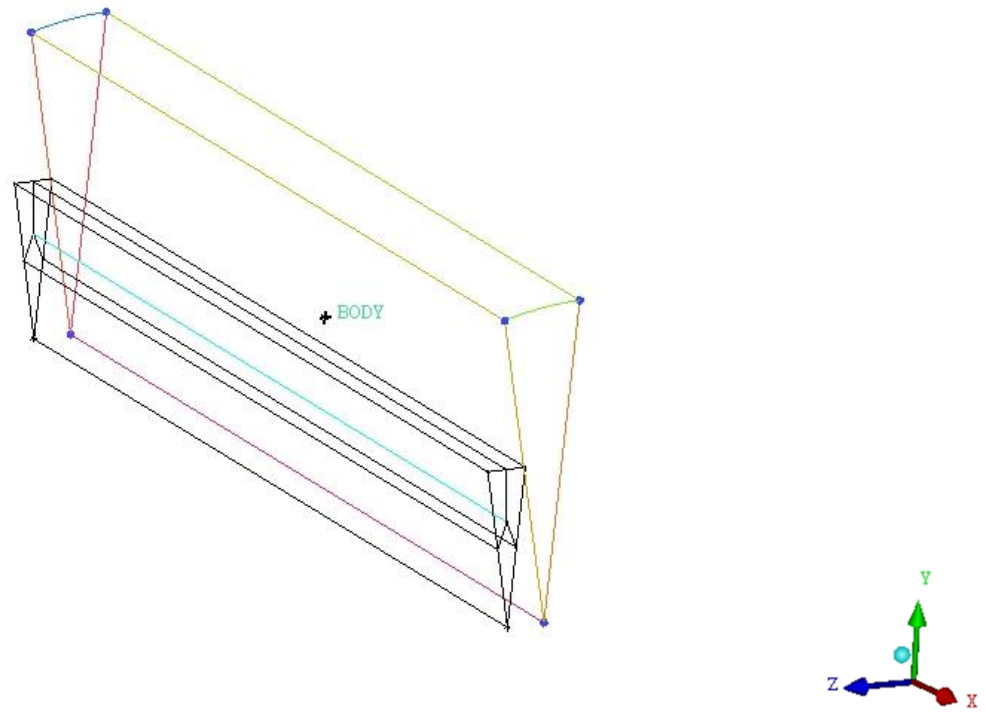


Figure A.7: Geometry and blocking after the blocks were deleted

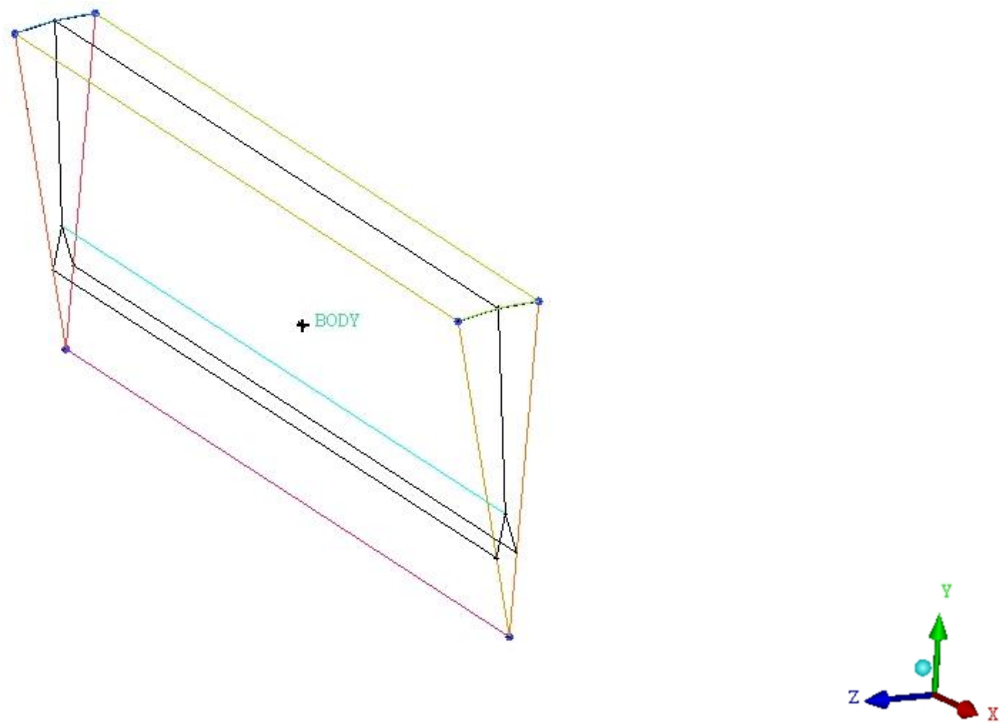


Figure A.8: Associated vertices of the blocking and points of the geometry

In the main geometry, the diamond-shaped region at the bottom of the wedge should be small enough to have curved-shape grids and big enough to stay within the tolerance range of the grid (0.01mm). Therefore, the height of this region was chosen to be 0.12 mm.

12. Once the geometry was created and the blocking and association were done, a mesh was created on the geometry as shown in Figure A.9. Because of the Cartesian nature of the geometry, the hexagonal meshing module (HEXA) was used which is capable of creating O-grids. The number of nodes, value of the spacing from the wall and the stretching ratio of the nodes were specified for each edge. Uniform distribution of nodes for all axial edges (edges in  $x$  direction) was chosen. For radial edges (in  $y$  and  $z$  direction), bi-geometric spacing option was used. Ratio and spacing of nodes were altered in a way to acquire enough nodes near the wall to solve the boundary layer properly. The value of the first spacing near the wall was adjusted to obtain the desired  $y^+$  value range.

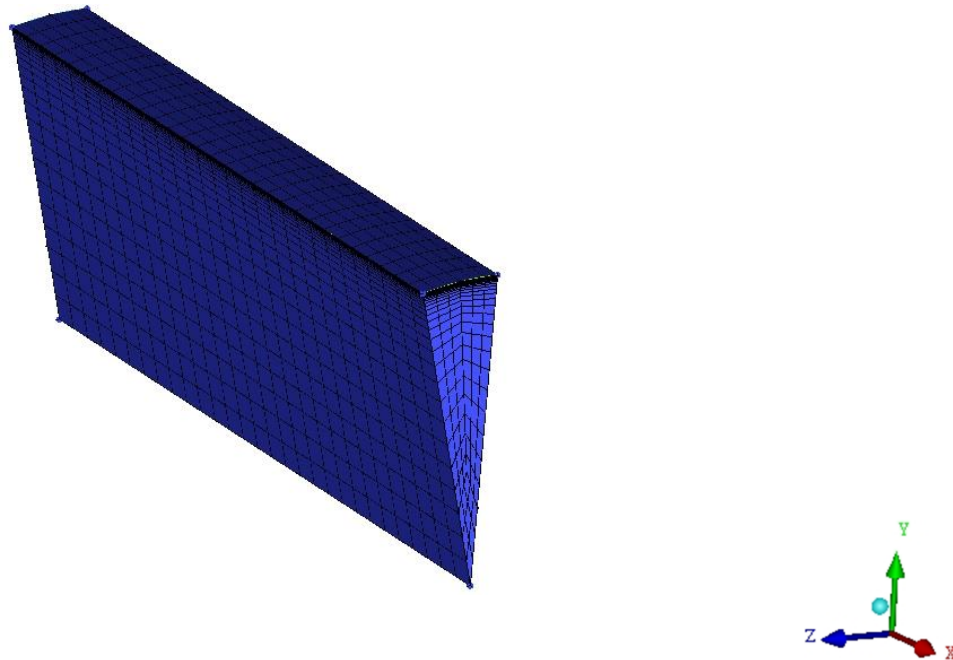


Figure A.9: The mesh applied on the geometry

## APPENDIX B

### MOMENTUM SOURCE TERM

#### Momentum Source terms

Momentum sources can be applied in CFX using two methods: Loss model and General Momentum Sources.

➤ Loss Model

An additional source term is added to the momentum equation, which is responsible for the isotropic or directional losses. In this study the isotropic losses in  $y$  and  $z$  direction are neglected and the loss in the  $x$  direction is modeled as follows:

$$S_{M,x} = -\frac{\mu}{K_{perm}}U_1 - K_{loss}\frac{\rho}{2}|U|U_1 \quad (\text{B.1})$$

Where  $K_{perm}$  is the permeability,  $K_{loss}$  is the loss coefficient,  $|U|$  is the magnitude of the local velocity,  $U_1$  is the local  $x$ -direction velocity, and  $\rho$  is the local density.

As discussed in Chapter 4,  $K_{perm}$  was set to infinity ( $10^{30}$ ) to eliminate the role of the viscous loss in the momentum equation source term.

$$\frac{\mu}{K_{perm}}U_1 = 0 \quad (\text{B.2})$$

Therefore,

$$S_{M,x} = -K_{loss}\frac{\rho}{2}|U|U_1 \quad (\text{B.3})$$

To specify a value for isotropic loss, a fluid subdomain with an adiabatic wall was added to the main domain. By neglecting the effect of velocity variation, shear stress and gravity in the subdomain, the momentum equation for steady-state condition becomes:

$$-\frac{\partial P}{\partial x_i} + S_{M,x} = 0 \quad (\text{B.4})$$

Therefore,

$$\frac{\partial P}{\partial x_1} = -K_{loss} \frac{\rho}{2} |U|U_1 \quad (\text{B.5})$$

Equation (B.5) allows introducing the desired pressure drop into the momentum equation by specifying the  $K_{loss}$ .

➤ General Momentum Source

General momentum source is another option in CFX which enables the specification of momentum sources in a specific direction, directly in terms of a momentum value per unit volume. Therefore, the momentum source in  $x$  location becomes:

$$S_{M,x} = S_{spec,x}i \quad (\text{B.6})$$

where  $S_{spec,x}i$  quantifies the specified momentum component in  $x$  direction.

To obtain good convergence when the source term is a function of velocity, Momentum Source Coefficient is used to linearize the source term, such that:

$$-\frac{\partial P}{\partial x_1} = KU_1 \quad (\text{B.7})$$

where  $K$  is the momentum source coefficient.

When setting a General Momentum Source, there are two optional parameters which should be enabled when the momentum source is meant to induce a pressure drop. These options are: **Redistribute in Rhie Chow** and **Include Coefficient in Rhie Chow**.

Enabling these two options avoids the possible pressure wiggles near the subdomain boundary.

In the General Momentum Source option, the value of source term can be inserted as constant or as a function. Since in this study, the momentum source is used to induce a pressure gradient, the source term is specified as follows:

$$S_{M,x} = -\frac{K}{\Delta x} \times G \times U \quad (\text{B.8})$$

where  $K$  is the local pressure drop coefficient, and is the same  $K$  factor which is used in 1-D codes,  $\Delta x$  is the length of the subdomain part and  $G$  is a constant value and is equal to:

$$G = \frac{\dot{m}}{A} \quad (\text{B.9})$$

where  $\dot{m}$  is the mass flow rate and  $A$  is the cross section area. In Equation (B.8) either the local or the area-averaged value of velocity could be used.

When using the Loss Model, the value of pressure gradient is calculated based on local values of velocity. Therefore, as the flow approaches the wall and the velocity goes to zero, the pressure gradient which is the momentum source also approaches zero (Equation (B.5)). The radial variation of momentum source in the subdomain for Loss Model is shown in Figure B.1.

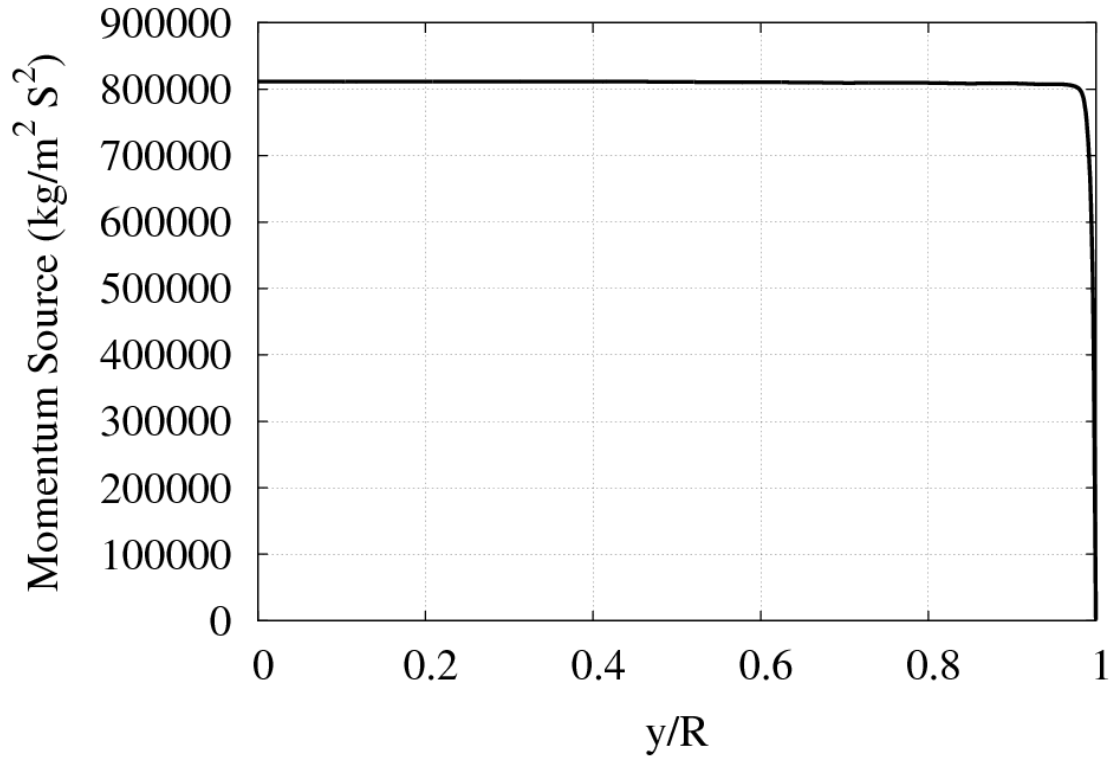


Figure B.1: Radial variation of momentum source in the subdomain using the Loss Model for Case S4 ( $\dot{m} = 0.06 \text{ kg/s}$ )

This variation of momentum source causes the velocity of the fluid to accelerate near the wall, as the drag term goes to zero. The velocity profile just before the subdomain and along the subdomain is shown in Figure B.2.

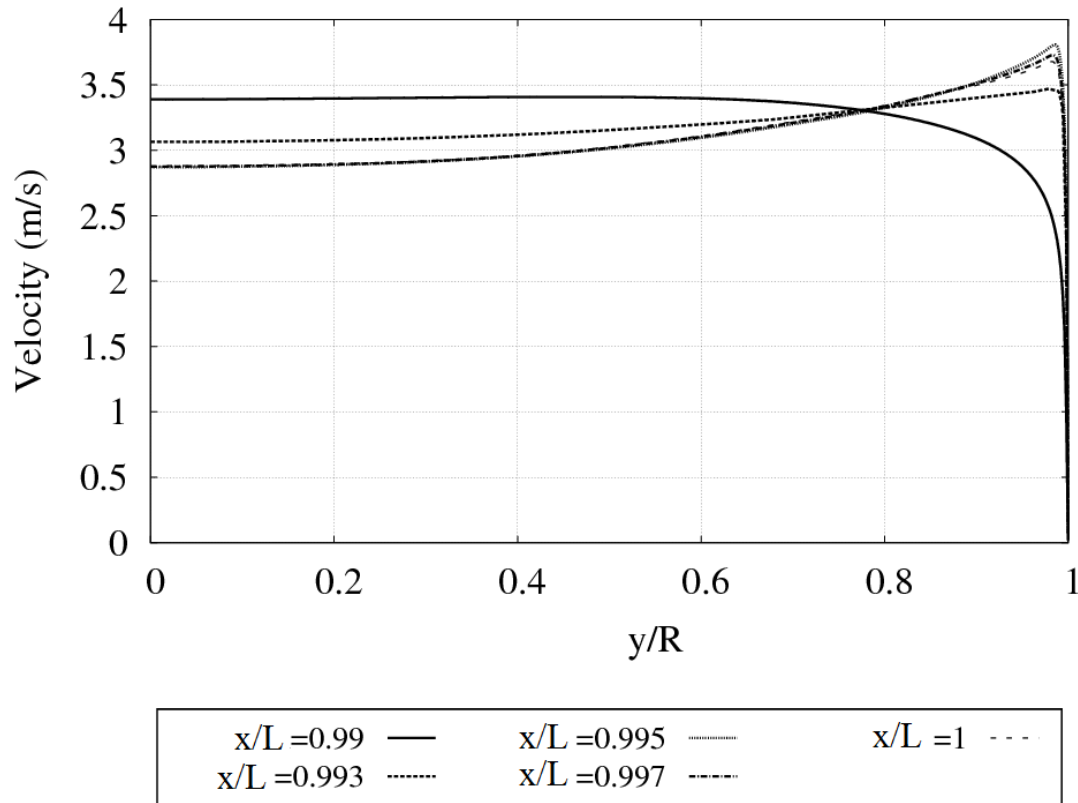


Figure B.2: Radial variation of velocity at different axial locations, slightly before and along the subdomain using the Loss Model for Case S4 ( $\dot{m} = 0.06 \text{ kg/s}$ )

However, in 1-D codes, the pressure gradient is calculated based on a bulk value of the velocity and, therefore, there is no radial change in the value of momentum source (since there is no radial coordinate) and, consequently, there is no acceleration in the flow. Therefore, to obtain simulation which agrees better with the 1-D code, the General Momentum Source option in CFX can be used while the source term is defined as Equation (B.8) and is based on an area-averaged value of velocity. This way, the momentum source stays the same in radial location. Figure B.3 shows the radial variation of momentum source term when using the General Momentum Source model with the source term as a function of the area-averaged velocity.

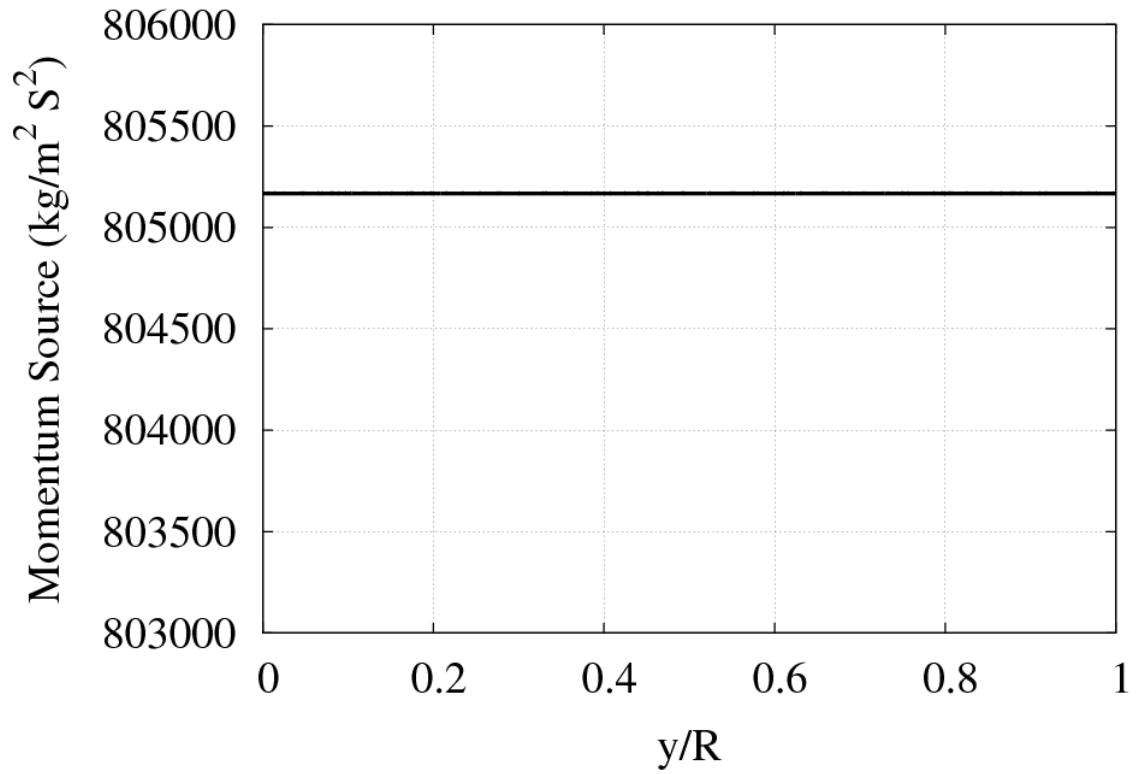


Figure B.3: Radial variation of momentum source in the subdomain using the Momentum Source Model for Case S4 ( $\dot{m} = 0.06$  kg/s)

This way, the profile of velocity before and after the subdomain has no acceleration as shown in Figure B.4.

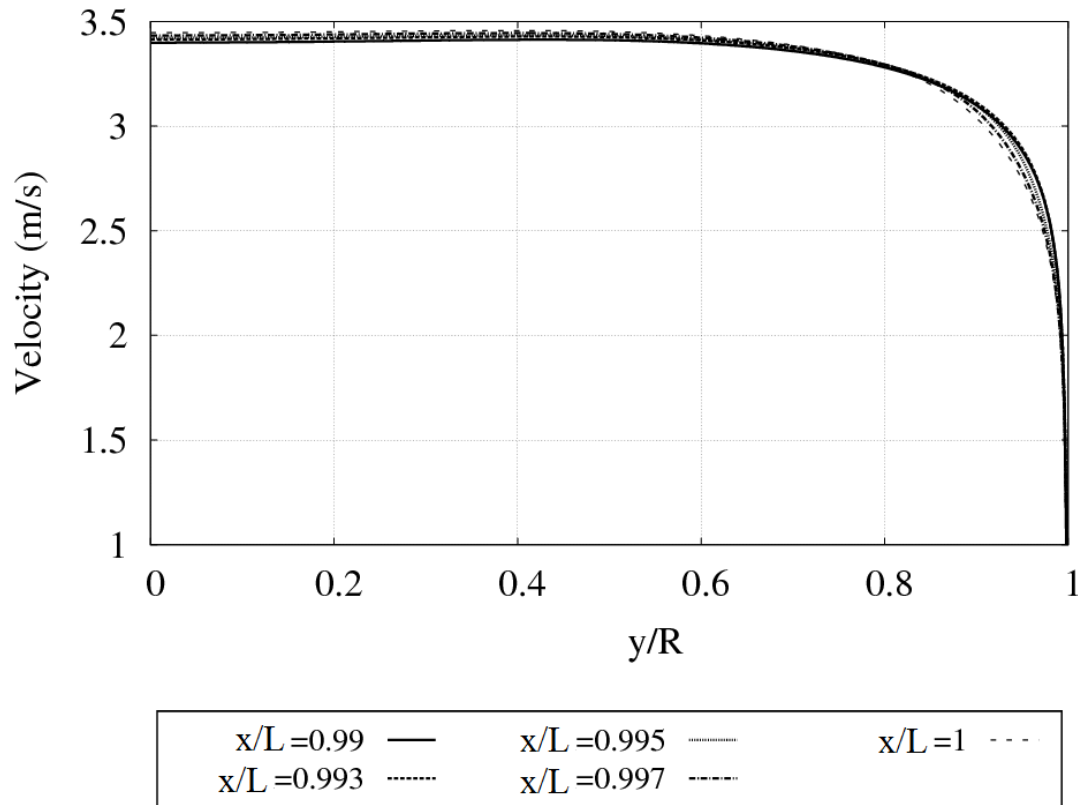


Figure B.4: Radial variation of velocity at different axial locations, slightly before and along the subdomain using the Momentum Source Model for Case S4 ( $\dot{m} = 0.06 \text{ kg/s}$ )

The use of Loss Model or the Momentum Source Model does not change the instability boundary results, considerably. Simulating Case S4 using both methods showed that using the Momentum Source Model changes the instability results by about 0.8 %. Therefore, the results of this study obtained using the Loss Model are reliable. However, in future studies, to have a closer simulation to 1-D codes, the second option for the momentum source term is recommended.